School of Physics and Astronomy
Raymond and Beverly Sackler Faculty of Exact Sciences
Tel-Aviv University

Properties of the reaction $pp \to ZZ$ at 14 TeV using the ATLAS detector

Thesis submitted to the Senate of the Tel-Aviv University as part of the requirements for the degree "Doctor of Philosophy"
by

Erez Reinherz-Aronis

The research work for this thesis was carried out within the Experimental High Energy Group under the supervision of

Prof. Gideon Alexander
Prof. Erez Etzion

November 2010

Abstract

This thesis describes the investigation of the main physics properties of the ZZ production in pp collision of the Large Hadron Collider (LHC) at 14 TeV using the ATLAS detector via an extensive Monte Carlo samples. These include the measurements of the differential and total cross sections, determination of the longitudinal Z polarization, the angular correlation between the two $Z \rightarrow l^+l^-$ decay planes and the feasibility to study the Bose-Einstein Correlation (BEC) of the ZZ pairs. In addition the transformation from pp collisions to their basic $q\bar{q}$ reactions and vice versa have here been worked out to yield the so called Energy Density Functions.

In the differential and total cross section analyses the sensitivity to the Standard Model (SM) properties was studied by setting the Z mass to be a free fit parameter. In the differential cross section analysis the M_Z value of 98.45±13.62 and 92.91±6.13 GeV were obtained for the luminosities of 100 and 300 fb^{-1}. These results are improved in the total cross section analyses to M_Z = 90.88±0.89 and 91.03±0.19 GeV for the luminosities of 100 and 300 fb^{-1}.

In the study of the ρ_0 longitudinal Z polarization we applied two Spin Density Matrix analysis methods which yielded for the 300 fb^{-1} sample the values ρ_0 = 16.5±4.8 % and 15.1±0.4 % for a loose invariant mass cut and ρ_0 = 16.1±6.6 % and 15.5±0.4 % for a tight mass cut. These results are in a very good agreement between themselves and with the expected SM value of 15.6 %

The fit to the ZZ decay planes correlation strength $A(zz)$ lead to the results 0.031±0.068 and 0.023±0.037 for the luminosities of 100 and 300 fb^{-1}. These $A(zz)$ values are consistent within errors with the expected one of ∼0.02.

Finally the feasibility of a BEC study of ZZ pairs has been explored and was found that it can be realized only in the planned future Super LHC with a typical luminosity of the order of 1000 fb^{-1} per year.

Acknowledgements

I would like to start and thank both of my supervisors, Prof. Gideon Alexander and Prof. Erez Eztion for their continuous support and guidance along the way. My thanks are to Prof. Gideon Alexander for sharing his enormous experience with me and for his endless and timeless assistance as well as for all his suggestions, comments and talks we had about my work, which always constituted an enlightening experience and to Prof. Erez Eztion in particulate for his continues guidance in the matters concerning Monte Carlo and detector aspects of my work.

My thanks are also to Prof. Avner Soffer and Drs. Gideon Bella, Yan Ben-Hammou and Arik Kreisel for their assistes and constructive discucssions along the way. Finally I would like to thank my colleagues in the Tel-Aviv ATLAS group for all their help, encouragement and many useful discussions throughout this work.

Contents

Chapter 1

Introduction

The current theory which deals with all the known physics properties of the elementary particles and their interactions, except gravity, is the well known Standard Model (SM) [1–3]. This theory has been extensively tested and found so far to describe very accurately the experimental results. In the SM theory the electroweak interactions are mediated via the photon and the massive gauge bosons $W^{\pm}$ and Z^0. However, a central part of the SM is still not experimentally discovered namely, the Higgs sector which is responsible for the particles' masses. Moreover, it is generally accepted that the SM is not the complete theory of particles and fields.

To this end the Large Hadron Collider (LHC) [4] was constructed at the European Organization for Nuclear Research (CERN) laboratory near Geneva, Switzerland that has been commissioned in 2009. This collider is planned to investigate new and exciting physics beyond the SM in proton-proton (pp) collisions at the center-of-mass (CM) energy of $\sqrt{s_{pp}} = 14\ TeV$, higher by almost an order of magnitude than the existing $2\ TeV$ collider, the Tevatron at Fermilab. Among the outstanding tasks of the LHC are the search for the missing Higgs boson, testing with a high precision the validity of the SM at higher energies and exploring "new physics" like the search for SUper SYmmetry (SUSY) particles. In addition this new collider may well supply information on symmetry violation between matter and antimatter.

The research work reported here is based on the ATLAS detector at the LHC and concentrates on the investigation of the ZZ gauge bosons pair produced in pp collisions at 14 TeV via their charged leptonic decay channels. One of the goals of this study was to examine the validity of the SM in its description to the ZZ pair production and to explore methods to search for new physics. Deviation from the SM predictions may, for example, occur either from the presence of anomalous couplings, or from the production of non-SM particles and their decays into vector boson pairs.

The production of the ZZ gauge boson pairs was previously studied at the LEP2 and at the Tevatron colliders. At the electron positron collider LEP2 the reaction $e^+e^- \rightarrow ZZ$ was measured [5] and found to be in good agreement with the SM predictions. At the Tevatron only a handful of events were collected [6–9] in its RunII.

In this thesis we report on the simulation studies of the following topics

- Measurement of the total and differential $q\bar{q} \rightarrow ZZ$ cross sections as a function of the CM energy of the ZZ system, $\sqrt{s_{ZZ}}$, and their comparison to theoretical expectations, whenever possible.
- Study of the angular correlations between the two $Z \rightarrow l^+l^-$ decay planes.
- Determination of the Z polarization via its decay into two charged leptons. This was studied in terms of the Spin Density Matrix analysis method. In particular the possibility to measure the longitudinal Z polarization is emphasized.
- The possible use of the Bose-Einstein correlation in ZZ pairs is shown.

The research work presentation is organized as follows: An overview of the LHC accelerator and the ATLAS detector is described in chapter 2. An introduction to the main physics aspects of this research work is given in chapter 3. The Monte Carlo events selection procedure is outlined in chapter 4. This is

followed in chapter 5 by the physics analysis results. In chapter 6 an attempt to measure the Bose-Einstein correlation of ZZ pairs is discussed. Finally a summary and an outlook are presented in chapter 7.

Chapter 2

The LHC accelerator and the ATLAS detector

2.1 The pp Large Hadron Collider

The current existing highest energy particle accelerator is the CERN Large Hadron Collider (LHC), which is aimed to collide proton-proton beams up to an energy of 14 TeV in their Center of Mass (CM) system. This collider, which utilizes the tunnel excavated for the e^+e^- Large Electron Positron (LEP) collider, is situated around 100 m below the ground level and includes several large halls to accommodate the approved LHC experiments (see Fig. 2.1).

Two of the experiments, ATLAS [10–12] and CMS [13,14], are constructed for a general study of pp collisions properties and in particular aimed to search for new physics. Two other experiments are the LHCb [15] which is dedicated to study B-physics and CP-violation and ALICE [16] which is designed for the research of heavy ion collision. The LHC has started its operation in 2009 with a pp $\sqrt{s_{pp}}$ of 900 GeV which was later upgraded to 7 TeV and is expected to reach in a couple of years to its planned value of 14 TeV.

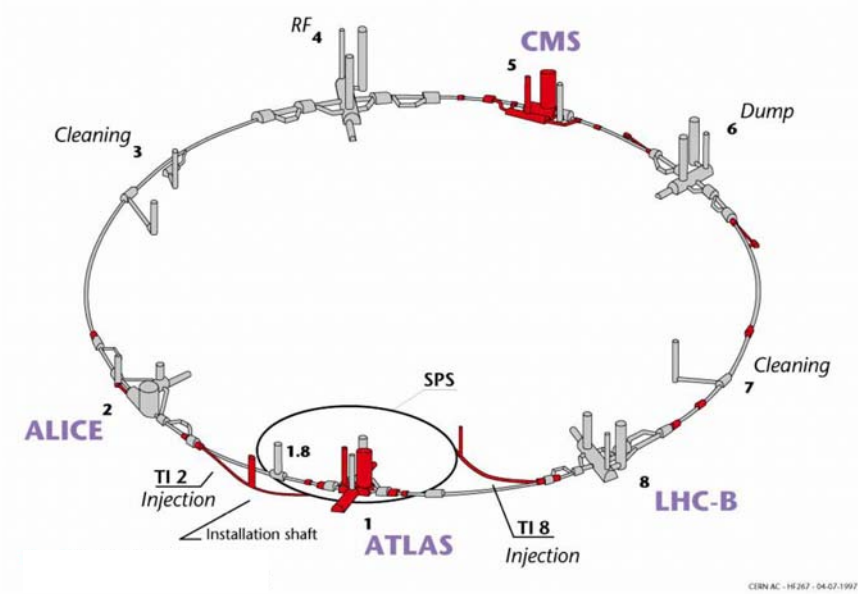

Figure 2.1: Layout of the LHC tunnel, taken from Ref. [17], which includes the location of the experiments and accelerator facilities.

2.1.1 The physics motivation

The new LHC collisions energy regime should extend our current knowledge of matter and its substructure. It is anticipated that the LHC will have the capability to discover or exclude new physics theories and expectations over a large range of predicted high mass particles and coupling strengths. Among them is the understanding of the electroweak symmetry breaking which involves the search for the predicted Standard Model (SM) Higgs boson, where its lower mass limit of 114 GeV [18] was given by LEP and excluded by the Tevatron in the region of 163-168 GeV [19]. Further goals are the improvement of the measurements precision of properties of the SM particles like the $W^{\pm}$ and Z^0 gauge bosons and heavy quarks and to search for "Beyond the SM" physics like supersymmetric particles or new heavy gauge boson.

2.1.2 The main LHC configuration

The LHC is placed in a 26.7 km underground ring tunnel which was excavated for its predecessor, the LEP collider. The LHC accelerator consists of two colliding synchrotron proton rings capable of accelerating protons from their injection energy of 450 GeV up to its highest designed energy of 7 TeV, which corresponds to a maximum CM energy of $\sqrt{s} = 14\ TeV$. The magnetic field needed to keep these beams circulating in the machine is provided by 1232 superconducting dipoles with a field of 8.4 $tesla$.

At the LHC each beam bunch consists of $\sim 10^{11}$ protons and has a size of a few centimeters in its motion direction and a diameter of about one millimeter. In order to increase the luminosity the bunches are squeezed to a diameter of about 16 μm as they approach the collision points. The two proton beams are planned to collide at the different interaction points every 25 *nano seconds* so that in the final collision stage they will reach a rate of about $\simeq 10^9$ $events/second$. This will result in around 20 events per bunch crossing which corresponds to about 1000 charged particles hitting each of the LHC detectors. For this reason the radiation tolerance of the detectors material was a crucial aspect in their design.

2.1.3 The acceleration scheme

The proton acceleration scheme is achieved in several stages. Prior to being injected into the main ring, protons are extracted from a hydrogen target and linearly accelerated in bunches up to the energy of 50 MeV in the LINAC (see Fig. 2.2). These 10^{11} protons bunches are then injected via the Proton Synchrotron Booster (PSB) into the Proton Synchrotron (PS) ring, which is the oldest accelerator on the CERN site, with a circumference of 630 m. The PS boosts the protons up to an energy of 26 GeV after which they are injected into the Super Proton Synchrotron (SPS) accelerator where they are brought to an energy of 450 GeV. In the past the 6.9 km circumference SPS was used as a $p\bar{p}$ collider where the UA1 and UA2 experiments provided the first evidence of the weak force carriers, the $W^{\pm}$ and the Z^0 [20–23]. Finally

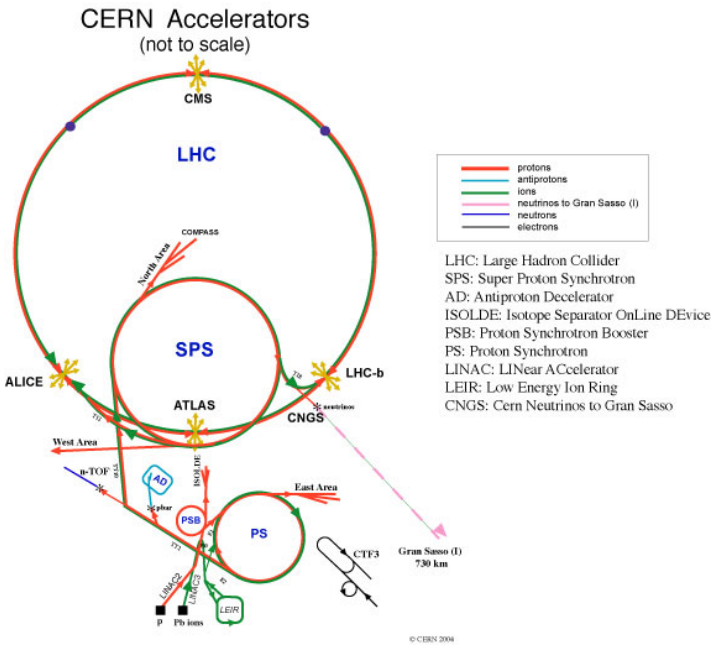

Figure 2.2: The LHC acceleration setup at the CERN site.

the proton beams are injected into the two separated beamlines of the LHC, the cross section of which are shown in Fig. 2.3, where they are accelerated to their final planned energy.

2.1.4 Time schedule of the energy and luminosity setups

Currently the operation of the LHC is planned to have two running periods. The first one started in 2010 and is due to end by the end of 2012. In this period the machine CM energy was set to $\sqrt{S} = 7\ TeV$ where the integrated luminosity is expected to reach the value of about 15 fb^{-1}. This period will allow the LHC staff to prepare for the next running period while the various experiments and physics groups will be able to test, align and calibrate their equipment and carry out the first 7 TeV pp collision analyses.

The second running period will follow a 12-16 months shutdown to support the necessary machine upgrade to allow the CM energy to reach the planned one of $\sqrt{s} = 14\ TeV$ with its envisaged integrated luminosity of $\sim$100 fb^{-1} per year.

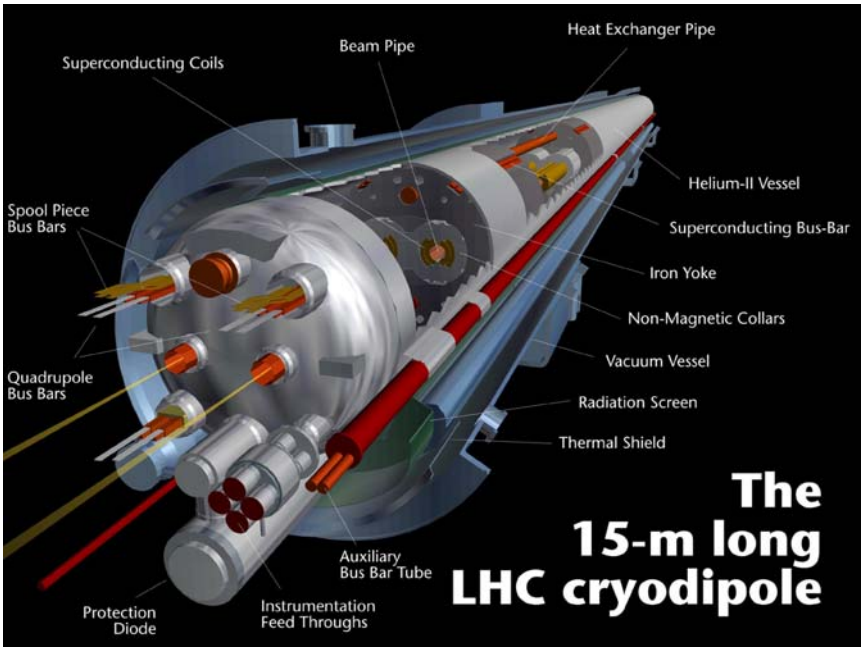

Figure 2.3: A profile cut of one of the LHC cryodipoles details of which are given in Refs. [24–27]

A precise measurement and control of the luminosity is a major experimental challenge at the LHC as it is needed for determination of the cross section of the various physics processes and to guarantee an optimal operation of the accelerator. The luminosity supplied by the accelerator can be determined by its beam parameters. The luminosity relevant for the physics analyses is the one accumulated by the detector [28] which can be measured by the use of physics processes like the $pp \to ppe^+e^-$ reaction. In the beginning it is anticipated that a luminosity precision of 5-10% can be reached from the LHC machine parameters.

2.2 The ATLAS detector

The "A Toroidal LHC ApparatuS" (ATLAS) detector is a multi-purpose detector which was constructed to exploit the full discovery potential of the LHC by studying in details a broad spectrum of physics processes. The ATLAS is designed to detect charged particles and most of the neutral ones, the still missing Higgs boson and proposed new physics particles.

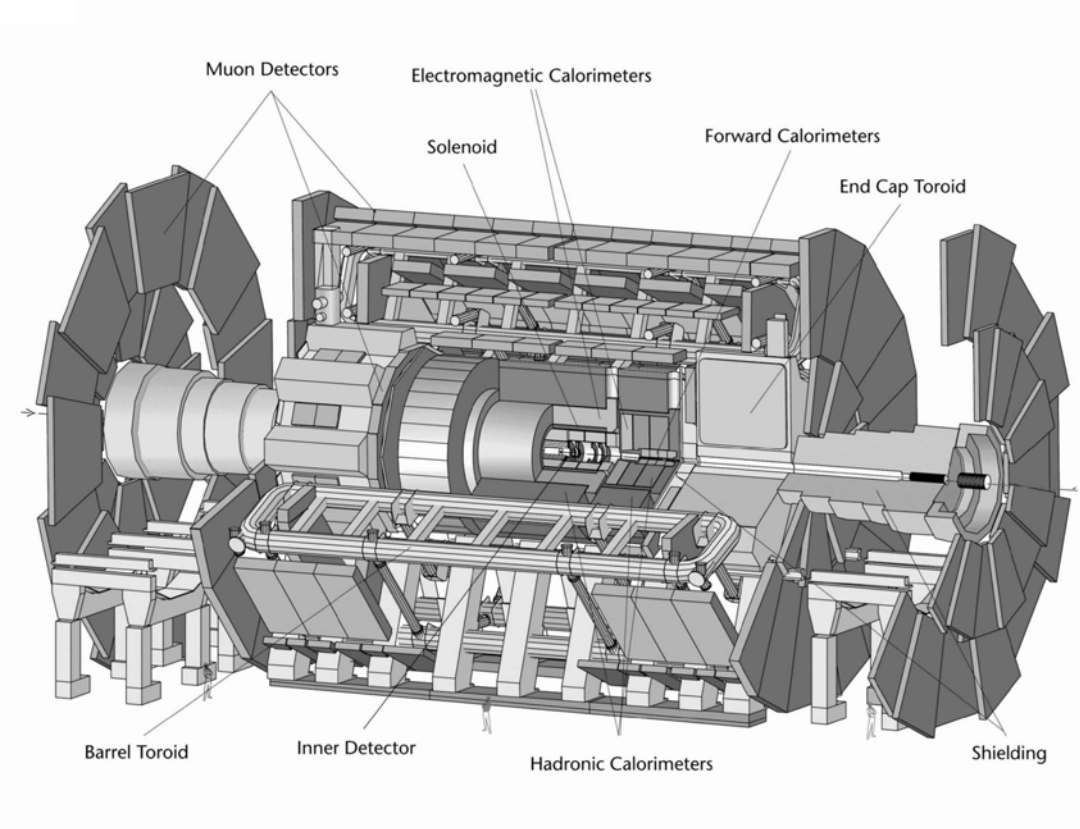

Figure 2.4: General view of the ATLAS detector.

The overall ATLAS detector layout, shown in Figure 2.4, is described in details in the Technical Design Reports (TDR) [10]. The shape of the ∼7000 *tons* detector has a cylindrical form of about 44 m long and 22 m in diameter. Like most former collider detectors, ATLAS is build in an onion-like structure which is divided into three major sub-systems: the inner detector, the calorimeters and the muon spectrometers. An important feature of the design

of the detector is its almost 4π radian coverage which allows measurements of missing momentum of the not detected neutral particles.

2.2.1 The ATLAS coordinate system

The origin of the ATLAS global xyz coordinate system lies in the center of the detector which coincides with the beam interaction point (IP). The z-axis lies parallel to the beam line in an anti-clockwise direction while the x-axis points to the center of the LHC ring and the y-axis points upwards and is perpendicular to both the x- and the z-axes. Due to the cylindrical shape of ATLAS it can also be described by a cylindrical coordinate system where the polar angle θ is defined with respect to the positive z-direction and the azimuthal angle ϕ is defined in the xy plane measured from the x-axis.

In addition to the particles geometrical direction one can also link them to the commonly used rapidity variable which is define as

$$y = \frac{1}{2} ln \left(\frac{E + p_L}{E - p_L} \right) \tag{2.1}$$

where E is the energy of the particle and p_L is its longitudinal component (in the z direction) of the particle momentum. The advantage in using the rapidity variable in hadron collisions is due to the fact that a difference between two rapidity values is invariant under the longitudinal Lorentz boost. In the reletivistic case, a good approximation for the rapidity is

$$\eta = \frac{1}{2} ln \left(\frac{|\vec{p}| + p_L}{|\vec{p}| - p_L} \right) = -ln \left(tan \frac{\theta}{2} \right) \tag{2.2}$$

where η is referred to as the pseudorapidity.

2.2.2 The ATLAS luminosity measurement

At the ATLAS detector a dedicated luminosity monitor has been installed, known under the name "LUminosity measurement with a Cherenkov Integrating Detector" (LUCID), which was active from the start of the first running period. The current luminosity precision measured by LUCID is about 10% [11]

and it is expected to be improved with time. The LUCID Cherenkov counter consists of two arrays of aluminum tubes filled with gas. The arrays are placed around the beam pipe at $\sim$17 m on both sides of the ATLAS interaction point and cover the very forward range of $5.6 < \eta < 5.9$. The tubes are 1.5 m long and have a 15 mm diameter with a 1 mm wall thickness. The aluminum tubes directed towards the IP in order to reject particles that are not created by the pp collisions. This counter monitors the number of interactions occurring in each bunch crossing by counting the mean number of charged particles within its acceptance. The Cerenkov photons created by the passage of charged particles in the gas are reflected on the tube walls until they reach the photomultipliers placed at the back of the tubes.

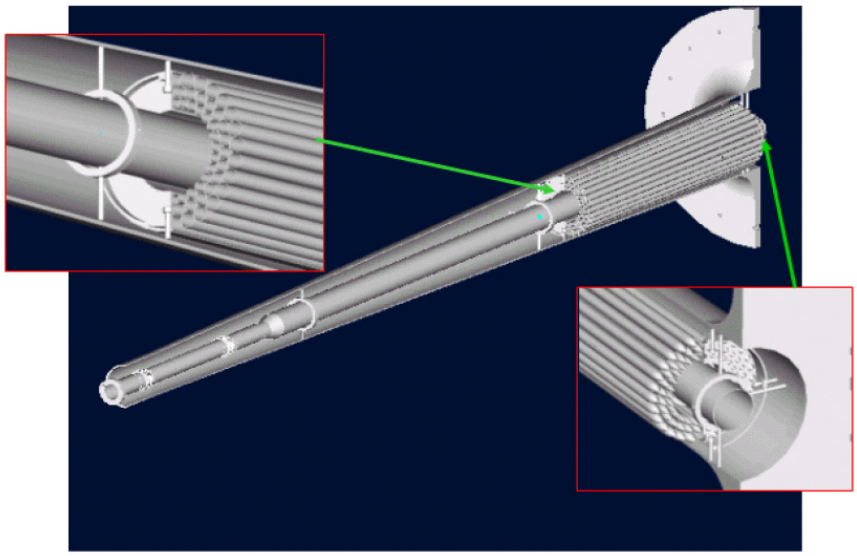

Figure 2.5: The LUCID detector placed between the beampipe and the conical support tube of the beampipe (taken from Ref. [29]).

2.2.3 The inner detector

The ATLAS Inner Detector (ID) [30, 31] is designed to measure the direction, momentum, and the sign of the particles electric charged produced in a high multiplicity environment of the LHC collisions. In particular it is aimed to reconstruct the primary vertex and if present also the secondary ones.

The shape of the ID is a cylinder with an outer radius of 115 cm and a total length of 7 m. The complete ID structure is contained within a magnetic field of 2 *tesla* that allows the determination of particles' momenta by measuring the tracks curvature. The inner detector is divided into three sub-detector, as shown in Fig. 2.6 [32]. These three sub-systems, although technically independent, act complementary to fulfill the basic experimental tasks of the ID. The most inner layer, closest to the interaction point, is the silicon pixel detector. This sub-detector is surrounded by the SemiConducting Tracking (SCT) sub-detector and the most outer layer of the ID, the Transition Radiation Tracking (TRT) system. The acceptance of the inner detector is designed to cover a large close spherical volume to prevent as much as possible the escape from detection of outgoing particles. This acceptance can be also expressed in terms of the pseudorapidity η namely it is confined to $|\eta| < 2.5$. To note is that in order to minimize the radiation damage both the pixel and SCT sensors are cooled down to an operation temperature range of -5° C to -10° C.

The pixel detector

The pixel sub-detector is the closest component of the detector to the IP. Its main task is to provide measurements of charged tracks at high multiplicity and extreme radiation background.

As can be seen from Fig. 2.6 [32] the pixel sub-detector system consists of three cylindrical layers around the beam axis in the barrel region with the radii of 5, 9 and 12 cm followed by three disks perpendicular to the beam axis at distances of 50, 58 and 65 cm in the z direction on both sides of the IP. The pixel sub-detector is assembled out of 1,744 pixel sensors of dimension $19{\times}63$ mm^2 where each of them is constructed out of $\sim$47,000 silicon pixels. With about 80.4 million readout channels, the pixel detector provides, via the bending solenoidal magnetic field, a precise determination of the momentum, the impact parameter and the primary vertex of charged tracks. Its spatial resolution is of 10 μm in the ϕ-plane and 115 μm in the z-direction [32]. The high granularity of the first pixel detector layer is essential for a good vertex resolution of the secondary vertices which are crucial for the identification of

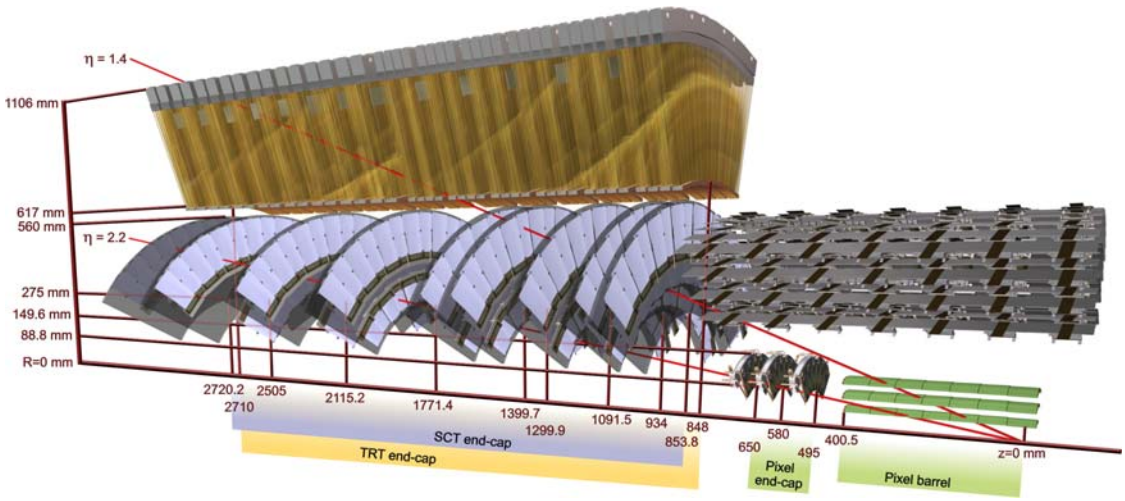

Figure 2.6: A 1/8 cylindrical profile cut of the Inner Detector system showing the three sub-detectors, taken from [32]. The silicon pixel detector is the cylindrical layer on the bottom right and the followed three perpendicular disks. The SemiConducting Tracking system is the middle layer of cylinders and disks. The Transition Radiation Rracking system is presented only in the endcap region by the upper left component. In addition the figure includes two charged tracks emerging at $\eta = 1.4$ and 2.2.

short-lived particles such as the B hadrons and the b quark. To note is that the pixel sub-detector will suffer from the highest radiation damage rate and its performance will most probably deteriorate after a few years.

The semiconductor tracker

The SemiConductor Tracker (SCT) which surrounds the pixel sub-detector is the middle component of the ID. It was designed, as the pixel sub detector, to determine for each track its momentum, impact parameter and vertex position.

The SCT which is shown in Fig. 2.6 uses silicon microstrip technology for tracking charged particles [33, 34] and is constructed from silicon sensors (like the pixel detector) which are segmented in strips thus giving a position measurement. The SCT at the barrel region consists of four cylindrical shaped layers with radii of 30, 37, 44 and 51 cm of silicon strips which are arranged

so that each layer has one set of silicon strips parallel to the beam axis and another set tilted by angle of 40 $mrad$ in order to measure the radial and longitudinal position of the hit. The same layer arrangement was also used at the endcap region where nine axial wheels equipped with double layers of silicon strip detectors were installed on each side of the IP. The SCT with its ∼6.2 million readout channels has the spatial resolution of 17 μm in the ϕ-plane and 580 μm in the z-direction [32]. It was design to resolve ambiguities of two tracks separated down to 200 μm in the dense tracking environment of the LHC.

The transition radiation tracker

The Transition Radiation Tracker (TRT) is the outermost part of the ID. Its main tasks are to serve as an electron identifier and to improve track momentum resolution by providing a long lever arm of measured hits.

The TRT is made out of polypropylene sheets sandwiched between drift tubes, called straws, which have a diameter of 4 mm and a length varying between 37 cm in the endcap region to 144 cm in the barrel region. These straws are filled with a xenon gas mixture. As can be seen from Fig. 2.6, it covers the pseudorapidity region of $|\eta| < 2.0$ and has the intrinsic resolution of 130 μm [35]. In the barrel region there are 52,544 straws arranged along the beam pipe. At the endcap region these straws are arranged radially in 18 wheels with a total of 319,488 straws.

Charged particles crossing the the polypropylene sheets emits photons that are registered in Xe gas of the straws, while all the charged particles producee ionization in the straws. These photons which are referred to as transition radiation have energies in the X-ray range [36]. The number of photons emitted is proportional to the Lorentz factor, $\gamma = E/m$ where E and m are the energy and mass of the charged particle. Thus the electron which has a small mass does emit a larger amount of radiation that allows the separation between it and heavier particles with the same energy.

2.2.4 Calorimetry

The ATLAS calorimeter detection system shown in Fig. 2.7 [37] is responsible for the energy measurement of particles and jets (both charged and neutral). In addition, an important role of this sub-detector is to determine the missing transverse energy by summing up all the measured energy deposits.

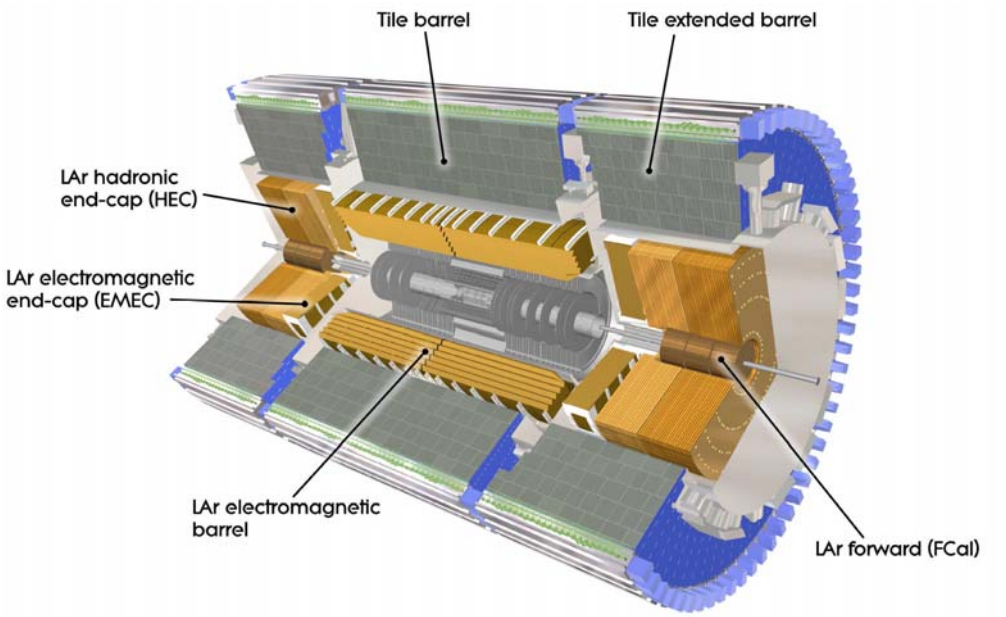

Figure 2.7: The calorimetry system. The different sub-detectors in both the barrel and the endcap regions are indicated, taken from [37].

The calorimeters are divided into an inner part, the electromagnetic calorimeter which is optimized to measure photons and electrons and an outer part referred to as the hadronic calorimeter which is optimized to detect hadrons. The electromagnetic calorimeter covers the range $|\eta| < 3.2$ and the hadronic one, including the forward calorimeter, extends up to $|\eta| < 4.9$. The calorimeters use high atomic number material which causes the incoming particle to interact with their media producing Electro-Magnetic showers of particles. The showers are initiated in the absorber material and extend into the active material where the ionization of the produced shower is measured.

Electromagnetic calorimeter

The electromagnetic calorimeter is a highly granular lead-liquid argon sampling calorimeter that is placed around the ID and is designed to identify and measure the energy of electrons and photons.

The calorimeter consists of passive absorbers that are made out of lead (Pb) and stainless steel while the active parts consist of Liquid Argon (LAr). The choice of LAr was made because of its very good radiation tolerance whereas the choice of Pb is due to its high atomic number which ensures that the electrons and photons showers are well developed to be detected in the active medium. The lead plate modules are organized geometrically in an accordion-shape which provides a uniform azimuthal coverage by minimizing the gaps between the detector modules. The barrel electromagnetic LAr calorimeter covers the range of $|\eta| < 1.5$ whereas the endcap region extends this rage to $1.4 < |\eta| < 3.2$. The material at $|\eta| < 2.5$ in front of the calorimeters introduces an uncertainty in the energy measurement of particles due to energy loss in that material. A correction for this loss is achieved by the the coli material placed in front of the electromagnetic calorimeters. The electromagnetic LAr energy measurement resolution σ is consistent with its designed value [38–40] of

$$\frac{\sigma}{E} = \frac{10\%}{\sqrt{E}} \oplus 0.7\% \tag{2.3}$$

where the energy E is expressed in GeV.

Hadronic calorimeter

The ATLAS hadronic calorimeters which cover the pseudorapidity range of $|\eta| < 4.9$, use three different detection techniques to meet their physics goals and to tolerate the background radiation.

In the barrel region of $|\eta| < 1.7$, the so called Tile Hadronic Calorimeter (TileCal), is made out of steel which acts as an absorber and tiles of plastic scintillators that serves as the active material. The TileCal cells do points towards the IP. In the endcap region, where radiation tolerance is crucial, the

LAr is used as the active material while the steel is replaced by copper to be the absorber medium. The endcap region is divided into the Hadronic Endcap Calorimeter (HEC) which covers 1.5< $|\eta|$ <3.2 and to the Forward Calorimeter (FCal) which extends the HEC coverage to 3.2< $|\eta|$ <4.9. The TileCal, HEC and FCal energy resolution are consistent with [41]

$$\frac{\sigma}{E} = \frac{50\%}{\sqrt{E}} \oplus 3\% \tag{2.4}$$

where as before E is expressed in GeV.

2.2.5 Muon spectrometers

The muon spectrometers form the outermost part of the ATLAS detector and cover the largest portion of its volume (see Fig. 2.9). They were designed and constructed to detect charged tracks emerging from the barrel and endcap calorimeters in the range of $|\eta| < 2.7$ and to serve as a trigger system for high energy muons in the pseudorapidity of $|\eta| < 2.4$ [42]. The spectrometers can measure muon tracks from momenta of a few GeV up to the TeV region with a resolution of 3% to 10% [32].

A layout of a quarter profile cut of the full muon spectrometer system is shown in Fig. 2.8. As seen from this figure the muon spectrometers is arranged in three cylindrical layers with radii of about 5, 7.5, and 9.5 m in the barrel region ($|\eta| < 1$). In the endcap region ($1 < |\eta| < 2.7$) four vertical disks perpendicular to the beam axis are placed at distances of 7, 11, 13.5 and 22 m from the IP. In the center of the detector ($|\eta| = 0$) a gap in the coverage has been left open for the service cables for the solenoid magnet, the calorimeters and the ID.

Muon measurement chambers

The muon measurement chambers were the main ATLAS component used in the present work. The momentum measurement precision of a muon track is achieved mainly by the Monitored Drift Tubes (MDT) setup associated with a dedicated magnetic system that is installed between the first and the

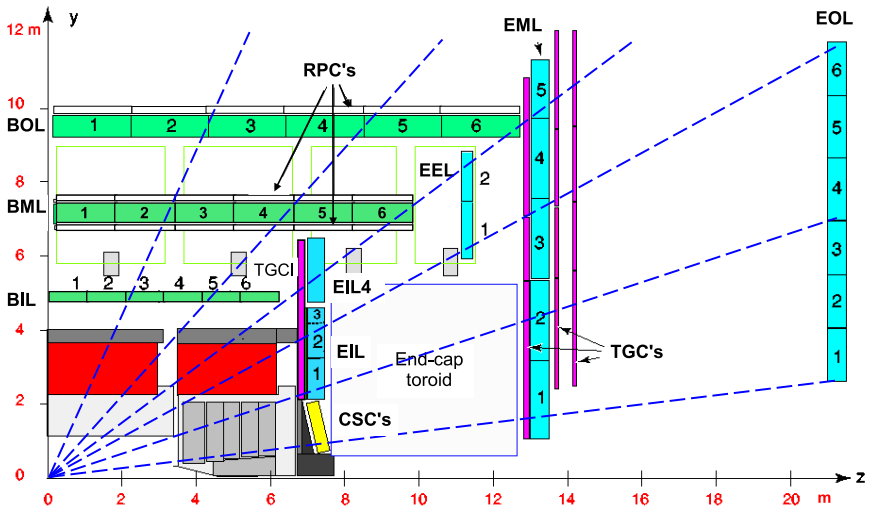

Figure 2.8: A quarter profile cut of the muon spectrometer system in a plane containing the beam axis (bending plane). Infinite momentum muon tracks are drawn by the dashed straight lines.

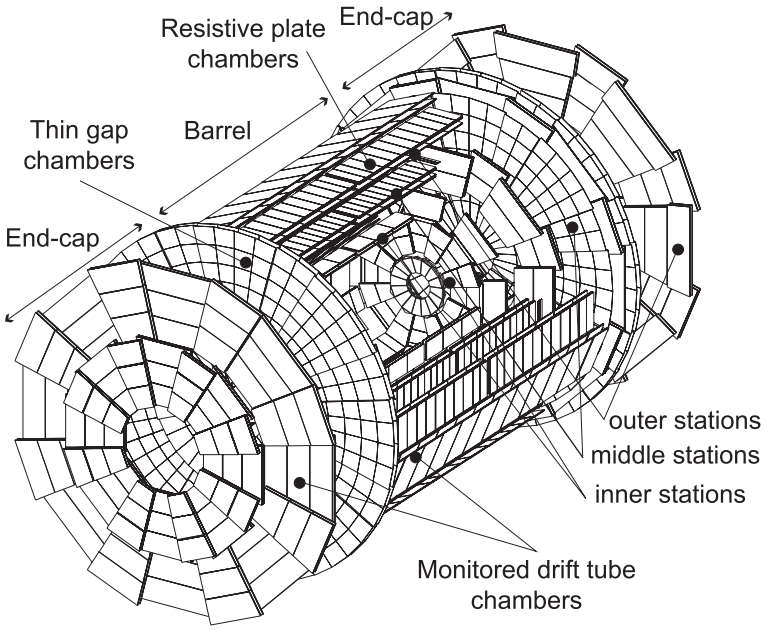

Figure 2.9: The ATLAS muon spectrometer setup, taken from [42]. The different muon chamber types are presented.

third MDT layers. This magnetic field setup consists out of large air-core superconducting magnets which include three toroids, two at the endcaps and one in the barrel, all installed symmetrically around the beam axis. Due to the toroid geometry the produced magnetic field is almost perpendicular to the muons trajectories.

The monitored drift tubes

The Monitored Drift Tubes (MDT) chambers, which cover the pesudorapidity range of $|\eta| < 2.7$, are made out of several aluminum drift tubes arranged in rows called layers. Each chamber consists of six or eight layers of tubes depending on the distance from the interaction point. Each drift tube is 29.97 mm in diameter, filled with a gas mixture of Ar/CO_2 (in the ratio 93:7) at a pressure of 3 bar [42]. In the center of the tube and along its length, a tungsten wire acts as the anode. When a charged particle traverses a tube it ionizes the gas and electrons are release. Under the influence of the radial electric field, electrons start to drift towards the wire forming an avalanche near its center. A measurement of the drift-time can be transformed into a distance between the wire and the particle passing track in the tube. In this way one can gather the measured points from all the layers of the chamber and fit a continues line through them. This line is referred to as a track segment which is a basic input to the muon track reconstruction algorithms. The resolution of the MDT chambers is about 80 mm per tube and is about 35 mm for the entire chamber [32, 43].

The cathode strip chambers

In the forward region ($2.0 < |\eta| < 2.7$), where a high background rate is expected, the MDT chambers are substituted in the first layer by the Cathode Strip Chambers (CSC) which are installed at a distance of $\sim$7 m from the IP. The CSC are multi-wire chambers which are designed to provide a spatial high resolution and time measurement. Their fine granularity is an important property for the separation of the signal from the background. They are constructed to measure simultaneously the η and the ϕ coordinates [32, 44]. The spatial resolution of an individual CSC is about 60 μm [32] in the bending

plane and 5 mm in the transverse coordinate. Their ability to operate in a high-rate data collection is mainly due to the small electron drift time which results in a time resolution of 7 ns.

Muon trigger chambers

An essential feature of the muon spectrometer system is its capability to trigger on muon tracks [42]. As a result the muon precision tracking chambers have been complemented by a system of fast trigger chambers which are a part of the ATLAS first level trigger. Their tasks are to determine the global reference time (bunch crossing identification) and to measure the muon track coordinates. The muon trigger system is constructed out of resistive plate chambers and thin gap chambers.

The resistive plate chambers

The Resistive Plate Chambers (RPC), which are located in the barrel region, are made out of two parallel resistive electrode-plates of phenolic-melaminic plastic laminate separated by a gap of 2 mm filled with $C_2H_2F_4$ gas [42]. The electric field maintained between the plates is $\sim$4.9 kV/mm. This field allows the production of an electron avalanche along the ionizing tracks towards the anode. The time resolution of the RPC is 2 ns [45] and its spatial resolution is about 1 cm.

The Thin Gap Chamber

The Thin Gap Chamber (TGC), which are installed in the end-cap region, are multi-wire proportional chambers constructed out of two cathode plates separated with a gap of a 2.8 mm. This gap is filled with a gas mixture of n-C_5H_{12} (n-pentane) and CO_2 [42]. The anode wires are at a distance of 1.8 mm from one another and are placed in the middle of the two cathodes plates. The about 2.9 kV [10] high electric field of the wires and the small wire-to-wire distance results in a very small time resolution of 4.5 ns [46, 47].

The TGC, which were developed and produced mainly in Israel, are installed with an accuracy of 5 mm and 2 $mrad$ between them. However the required stand-alone muon momentum resolution should be 30 μm [48].

Chapter 3

Physics background

3.1 The Standard Model in a nutshell

The 'Standard Model' (SM) of particle physics is a quantum field theory which describes the matter and its interactions in terms of fundamental point-like particles. This SM which has extensively been tested and found to be a successful description of our current knowledge in particles physics. It provides the theoretical framework to calculate measurable quantities, describes phenomena, and provides predictions that can be checked experimentally. The SM covers three of the four known forces namely, the electromagnetic, the strong and the weak, and is described by the local symmetries, $SU(3)_C \times SU(2)_L \times U(1)_Y$, where C is the color charge of the strong interaction, L indicates the left-handed weak interaction and Y is the weak hypercharge.

All known fundamental particles are divided into two categories according to their spin. The spin half particles, the $fermions$, consist of strong interacting *quarks* and weak interacting *leptons*. The interactions between the fermions are mediated by force carriers, the *gauge bosons*, which are spin 1 particles. These bosons are the W^+, W^- and Z^0 which carry the weak interactions, the *gluon* which is responsible for the strong interaction and the *photon* which carry the electromagnetic interaction. The currently known quarks and leptons belong to three generations, as shown in Table 3.1, where they are

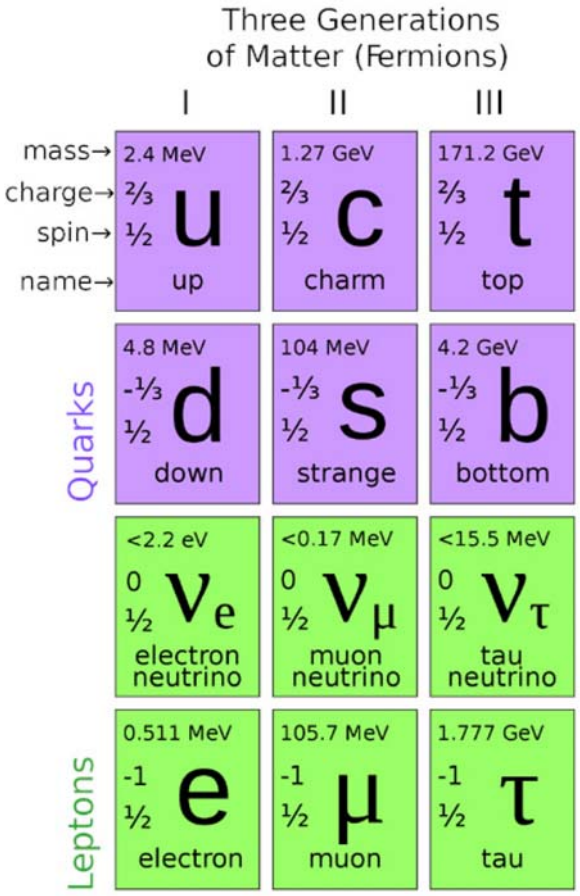

Table 3.1: *Quarks* and *Leptons* summary table. The fermions are grouped in doublets and ordered in three generations. Various properties of these fermions are also given.

grouped in doublets (pairs). As can be seen from the table, the upper quark of the doublet has an electric charge of $Q/|e| = 2/3$ and the lower one has a charge of $Q/|e| = -1/3$. In the leptonic sector we have in addition to the *electron* two heavier particles, the *muon* (μ) and the *tau* (τ), that have identical properties as the *electron* apart for their mass values. Each of these three leptons has a corresponding neutral partner namely, the *electron neutrino* (ν_e), the *muon neutrino* (ν_μ) and the *tau neutrino* (ν_τ).

So far quarks are found only in bound states, the *hadrons*. In general it is envisage that at high energy density one forms a *quark-gluon plasma* state where the quarks are not confined. The existence of this state still needs a ver-

ification. Hadrons exists in two forms: *Mesons*, which are a bound states of a quark and anti-quark, and *Baryons*, which are a bound states of three quarks. The hadron strong interaction is mediated by eight massless spin 1 gauge boson fields, the gluons, described within the Quantum-Chromo-Dynamics (QCD).

The electromagnetic and weak interactions were unified into the electro-weak theory by Glashow [1], Weinberg [2] and Salam [3] (GWS). This theory is described by three gauge fields, W_i, that are invariant under $SU(2)_L$ and an additional gauge field, B, which is invariant under $U(1)_Y$. It was further suggested by GWS, and confirmed experimentally, that one observes a combination of two of these fields

$$W^{\pm} = W_1 \mp iW_2 \tag{3.1}$$

and a mixture of the two other gauge fields, namely

$$\begin{pmatrix} A \\ Z^0 \end{pmatrix} = \begin{pmatrix} cos\theta_W & sin\theta_W \\ -sin\theta_W & cos\theta_W \end{pmatrix} \begin{pmatrix} B \\ W_3 \end{pmatrix} \tag{3.2}$$

where A is the electromagnetic vector potential and θ_W is the weak mixing angle known as the *Weinberg angle* which links the masses of the weak gauge bosons to be

$$sin^2\theta_W = 1 - \frac{M_W^2}{M_Z^2} \ . \tag{3.3}$$

The *Weinberg angle* is a free parameter of the SM and was determined experimentally to be $sin^2\theta_W$=0.231 [49] at the Z^0 mass. The weak mixing angle is also connected to the couplings of the gauge bosons to the fermions, namely

$$g_W = \frac{g_e}{sin\theta_W} \ , \quad g_Z = \frac{g_e}{sin\theta_W cos\theta_W} \ , \tag{3.4}$$

where g_e is one unit of the electric charge and g_Z (g_W) is the Z (W) boson couplings to the fermions as given in Table 3.2, where they are divided into sets of $Left$ and *Right couplings*.

The Z couplings to the different fermions can be also written in terms of the Vector (g_V) and the Axial-Vector (g_A) couplings which are related to the Left-Right couplings by

$$g_V = \frac{1}{2}(g_L + g_R) \ \text{ and } \ g_A = \frac{1}{2}(g_L - g_R) \ . \tag{3.5}$$

	g_L	g_R	g_V	g_A
$\nu_e,\ \nu_\mu,\ \nu_\tau$	$\frac{1}{2}$	0	$\frac{1}{4}$	$-\frac{1}{4}$
$e,\ \mu,\ \tau$	$-\frac{1}{2}sin^2\theta_W$	$sin^2\theta_W$	$-\frac{1}{4}+sin^2\theta_W$	$\frac{1}{4}$
$u,\ c,\ t$	$\frac{1}{2}-\frac{2}{3}sin^2\theta_W$	$-\frac{2}{3}sin^2\theta_W$	$\frac{1}{4}-\frac{2}{3}sin^2\theta_W$	$-\frac{1}{4}$
$d,\ s,\ b$	$-\frac{1}{2}+\frac{1}{3}sin^2\theta_W$	$\frac{1}{3}sin^2\theta_W$	$-\frac{1}{4}+\frac{1}{3}sin^2\theta_W$	$\frac{1}{4}$

Table 3.2: The Z boson couplings to fermions given in terms of the Left-Right couplings and the Vector and the Axial-vector couplings.

3.2 pp interactions at high energies

In QCD theory the proton is composed of three light valence uud quarks. In high energies the interactions between two colliding protons are dominated by gluon-gluon fusion. In addition there are the quark anti-quark interactions both of which leads to the production of hadronic jet(s). Further contributions to pp reaction comes from the Drell-Yan process [50, 51].

3.2.1 The reaction $pp \to Z + X$

The total expected $p\bar{p} \to Z + X$ and $pp \to Z + X$ cross sections are shown in Fig.3.1, taken from Ref. [52], where they are compared to the UA1 and UA2 measurements. To note is that since the $p\bar{p}$ annihilation process decreases with energy the $p\bar{p}$ and the pp cross sections approach each other at the higher energy end (see Figs. 3.1 and 3.5).

The inclusive production of a single $W^{\pm}$ and Z^0 have been measured and studied in $p\bar{p}$ colliders at 630 GeV by the Super Proton Synchrotron (SPS) at CERN and in the vicinity of 2 TeV by the $p\bar{p}$ Tevatron collider at Fermilab. The results of these cross sections multiplied by their charged leptonic decay ratios are shown in Figs. 3.2 and 3.3 with their expected behavior as a function of energy [54]. From this figure one observes that the cross sections increase with energy where the W one is higher than that of the Z by one order of magnitude.

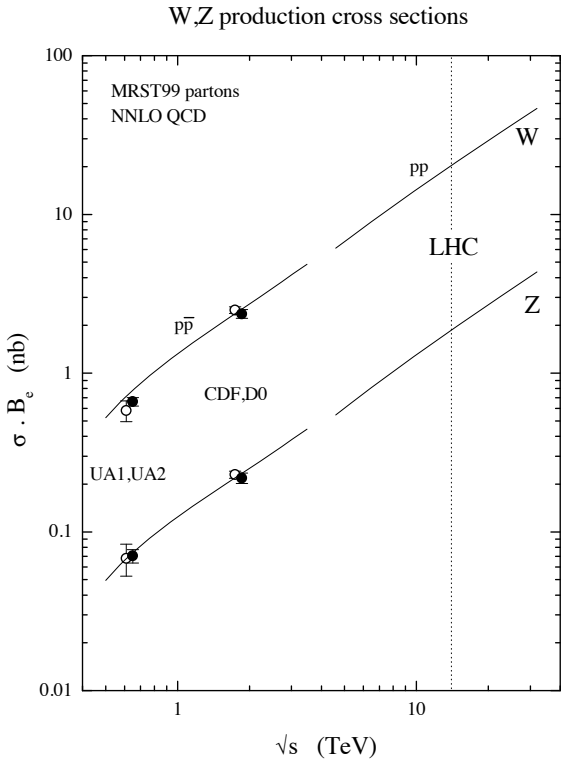

Figure 3.1: The expected production of the $Z + X$ in pp and $p\bar{p}$ collisions, taken from Ref. [53], as a function of $\sqrt{s_{pp}}$ compared to the experimental measurements of UA1, UA2, CDF and DØ.

An overview of several pp cross sections as a function of $\sqrt{s_{pp}}$ in the range 1 to 40 TeV, which also cover the LHC energy of 14 TeV, are presented in Fig. 3.4.

3.2.2 The reaction $pp \rightarrow ZZ + X$

While single production of gauge bosons were studied and investigated in some details by several hadronic collision experiments, the production of gauge boson pairs was barely experimentally accessible until now due to insufficient energy. In fact, in only two accelerators, the LEP2 and the Tevatron, these studies could be attempted.

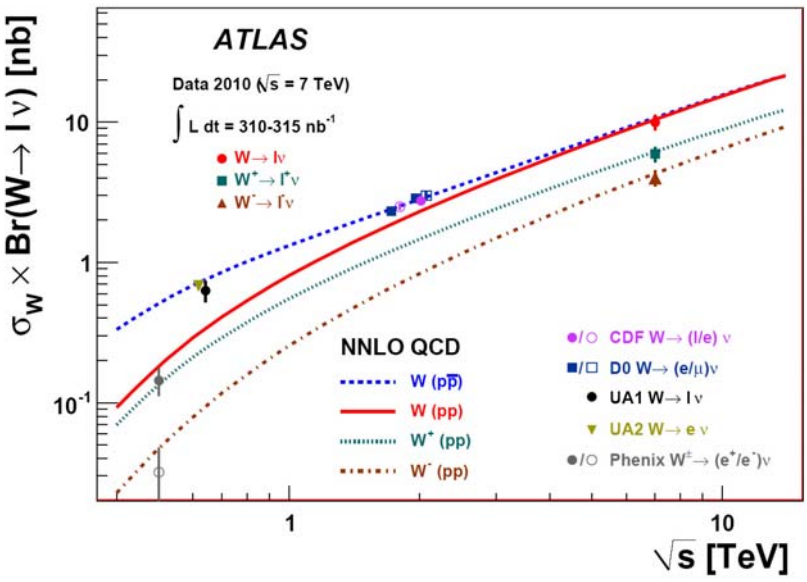

Figure 3.2: The inclusive cross sections of $p\bar{p} \to W + X \to l\nu + X$ as measured by UA1 and UA2 at the SPS collider and by CDF and DØ at the Tevatron and the inclusive cross sections of $pp \to W + X \to l\nu + X$ as measured by the ATLAS detector, taken from Ref. [54] The solid lines represent the expected cross sections multiplied by the bosons decay branching ratios to leptons.

The theoretical estimates of the production of ZZ and WW are shown in Fig. 3.5 as a function of the collision energy. As can be seen, at 14 TeV the pp and $p\bar{p}$ cross sections are approaching each other. Furthermore one can observe by comparing Figs. 3.2, 3.3 and 3.5 that the cross sections to produce a pair of gauge bosons is typically lower by three orders of magnitude than the production of a single one.

In the electron positron collider LEP2[1] at CERN the reactions $e^+e^- \to ZZ$ and $e^+e^- \to W^+W^-$ were measured. Their cross sections, which are shown in Fig. 3.6, are found to be in good agreement with the SM predictions (continuous lines). At the Tevatron in its RunII, only a handful of events were collected [6–9]. The LHC affords the opportunity to extend these studies to higher energies and larger statistics. The theoretical expected pp total cross

[1]LEP2 was an upgraded version of the LEP accelerator which operated up to ∼200 GeV

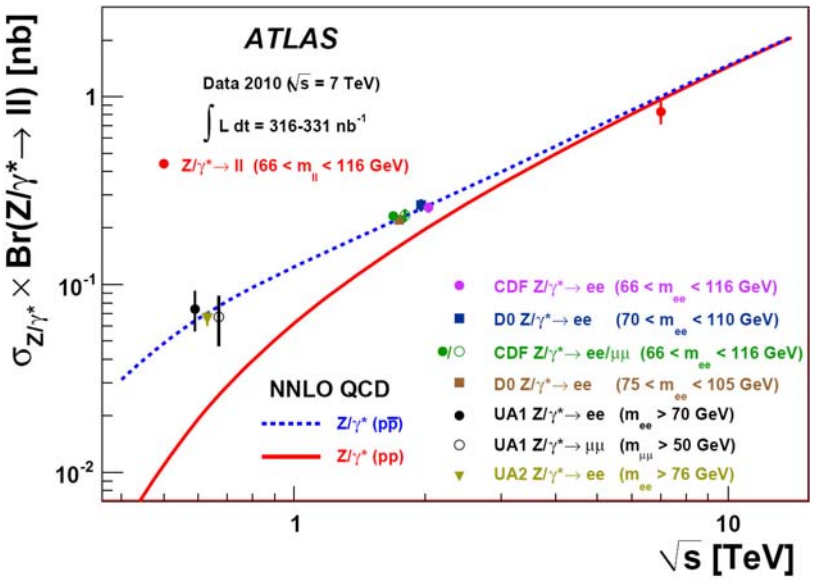

Figure 3.3: The inclusive cross sections of $p\bar{p} \rightarrow Z + X \rightarrow l^+l^- + X$ as measured by UA1 and UA2 at the SPS collider and by CDF and DØ at the Tevatron and the inclusive cross sections of $pp \rightarrow Z + X \rightarrow l^+l^- + X$ as measured by the ATLAS detector, taken from Ref. [54] The solid lines represent the expected cross sections multiplied by the bosons decay branching ratios to leptons.

sections at 14 TeV leading to WW, WZ and ZZ in the final state are listed in Table 3.3 where LO and NLO are respectively the leading and next to leading order calculations. As can be deduced from the table, a non-negligible uncertainty still exists in the theoretical estimats of these cross sections.

One should stress that the transformation from the pp cross sections to their fundamental $q\bar{q}$ cross sections requires the use of the Parton Distribution Functions, PDF. These functions describe the relative parton energy with respect to that of the proton laboratory energy that is $x = E_{parton}/E_{proton}$. Typical PDF distributions are shown in Fig. 3.7, taken from Ref. [62]. The effect of the PDF as used in the present work will be described in details in Sec. 5.1.

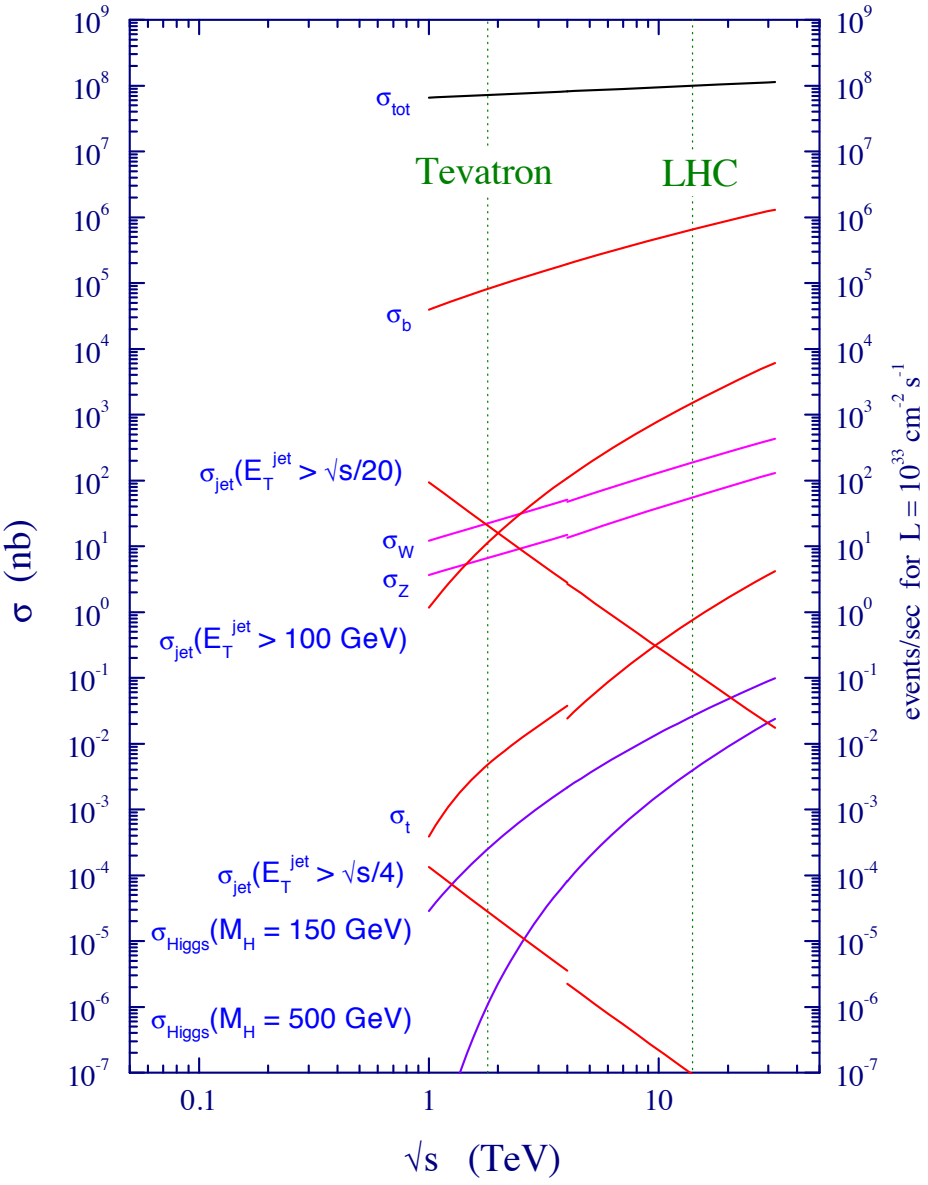

Figure 3.4: Overview of several pp cross sections as a function of $\sqrt{s_{pp}}$, taken from Ref. [55]. The right vertical dotted line corresponds to the LHC energy.

3.3 The $q\bar{q} \to ZZ$ reaction

The cross section of the process $q\bar{q} \to ZZ$, is one of the physics results that is expected to emerge from the operation of the new high energy LHC accelerator. The dominant SM lower order diagrams for this process are shown in

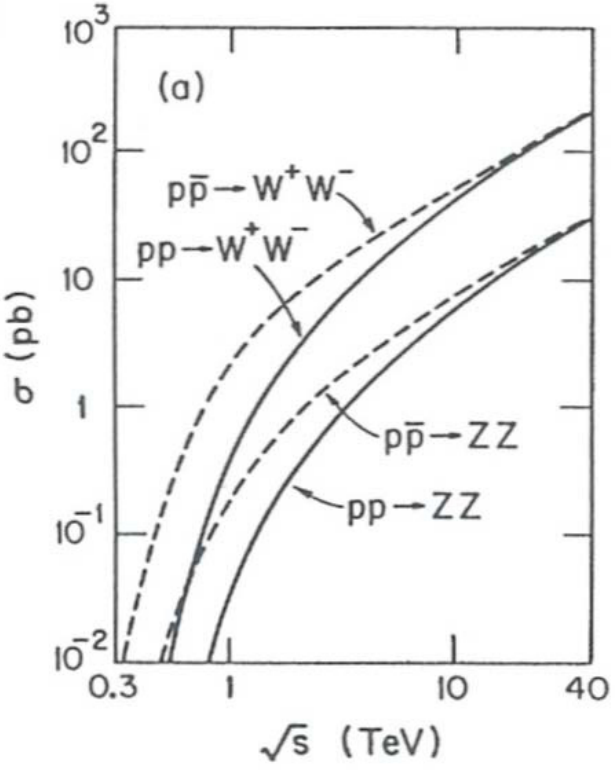

Figure 3.5: The theoretical calculated production cross sections of $ZZ + X$ and $WW + X$ in pp and $p\bar{p}$ collisions as a function of $\sqrt{s_{pp}}$, taken from Ref. [52].

Fig. 3.8 in terms of the Mandelstam variables [63].

A geometrical sketch of the process $q\bar{q} \to ZZ \to f\bar{f}f'\bar{f}'$ is shown in Fig. 3.9 where the Z boson production polar angle, θ_Z, is defined with respect to the $q\bar{q}$ collision line in the CM system of the ZZ pair. Note that due to the fact that the processes involves two identical particles θ_Z can only be defined between 0 and $\pi/2$ radians.

3.3.1 The Helicity Amplitude calculations

For the calculations of the gauge boson pair production via the quark anti−quark reactions we have utilized the helicity amplitudes method. To this end we have followed the notation and the helicity amplitude terms given in Table 3.4, which was taken from Ref. [64], to calculate the expected SM properties of the ZZ

Reference	[12]	[56]		[57]		[58, 59]
	LO	LO	NLO	LO	NLO	NLO
$\sigma(pp \to WW)$ $[pb]$	71	**84**	124	80	118	114.7
$\sigma(pp \to WZ)$ $[pb]$	26	**31**	54	29.5	50.7	50
$\sigma(pp \to ZZ)$ $[pb]$	–	**12.7**	17	11.7	15.6	15.3

Table 3.3: The total pp cross sections for the inclusive production of WW, WZ and ZZ at $\sqrt{s_{pp}} = 14\ TeV$ obtained from several theoretical estimates of Lower Order (LO) and Next to Leading Order (NLO) calculations. The values in bold are those used by us in Section 4.

final state. To this state both the t-channel and the u-channel configurations contribute. Each of them has two quark initial helicity states, $\lambda = \pm 1/2$, and three Z final helicity states, τ=−1, 0 and +1. Here again the angle θ_W is the known electro-weak mixing angle. In this scheme the vector (a_Z) and the axial vector (b_Z) couplings of the SM fermions ($f\bar{f}$) to the Z gauge boson are given by

$$a_Z \;=\; \frac{1}{4sin\theta_W cos\theta_W}(r_3 - 4Q_f sin^2\theta_W) \quad \text{and} \quad b_Z \;=\; \frac{1}{4sin\theta_W cos\theta_W} r_3 \;, \tag{3.6}$$

where Q_f is the electric charge of the fermions given in terms of the positron charge namely, $Q_f \;=\; 2/3, -1/3$ and -1 respectively for u, d and e. The weak isospin projection r_3 of the fermions is equal to +1 for the up quark and −1 for the down quark and the electron.

3.3.2 Differential cross sections

After integrating over the production azimuthal angle, the differential cross section of the process $q\bar{q} \to ZZ$ is given in terms of the helicity amplitudes $F_{\lambda\lambda'\tau\tau'}$ by

$$\frac{d\sigma}{dcos\theta_Z} \;=\; \frac{C|\vec{p}|}{16\pi\hat{s}\sqrt{\hat{s}}} \sum_{\lambda\lambda'\tau\tau'} |F_{\lambda\lambda'\tau\tau'}(cos\theta_Z)|^2 \;, \tag{3.7}$$

where θ_Z stands for the production scattering angle defined in the ZZ pair rest frame between the incident fermion and the final Z boson momentum (see Fig 3.9). The average color factor C is equal to 1/3 for $q\bar{q}$ initial state and is

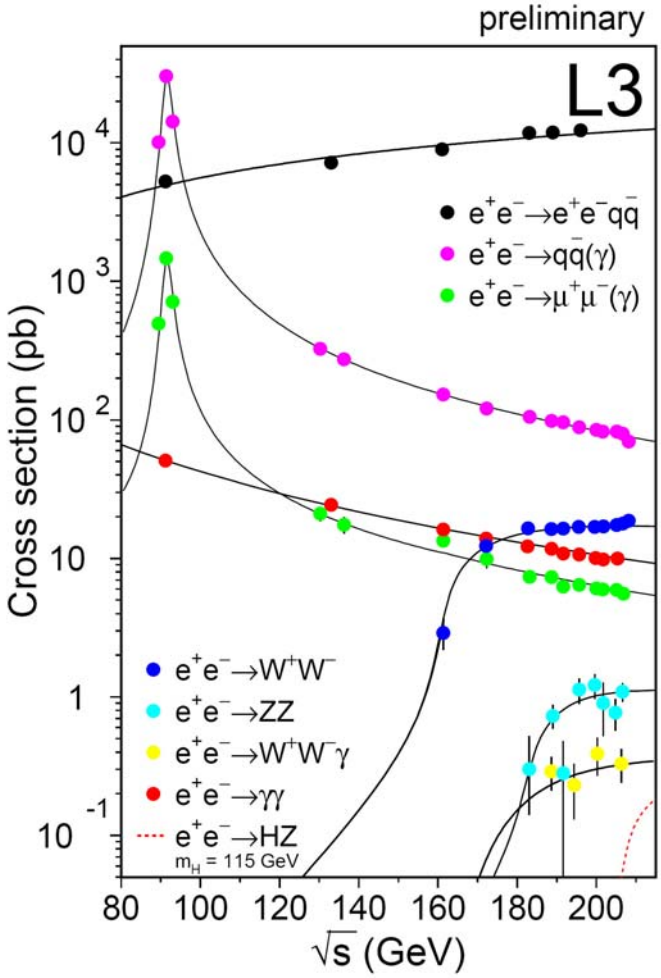

Figure 3.6: Several e^+e^- cross sections as a function of $\sqrt{s_{e^+e^-}}$ measured at LEP and LEP2. The figure is given by the L3 collaboration [60] and is based on Refs. [5, 61]. The continuous lines represent the SM expectations.

set to 1 for e^+e^- case. The momentum is given by $|\vec{p}| = \beta\sqrt{\hat{s}}/2$, were $\hat{s}$ is the $q\bar{q}$ center of mass energy squared ($=Ecm^2$) and β is equal to

$$\beta = \sqrt{\frac{(\hat{s} + m^2 - m'^2)^2}{\hat{s}^2} - \frac{4m^2}{\hat{s}}} \ . \tag{3.8}$$

In the case of a ZZ final state β is reduced to

$$\beta_{ZZ} = \sqrt{1 - \frac{4m_Z^2}{\hat{s}}} \ . \tag{3.9}$$

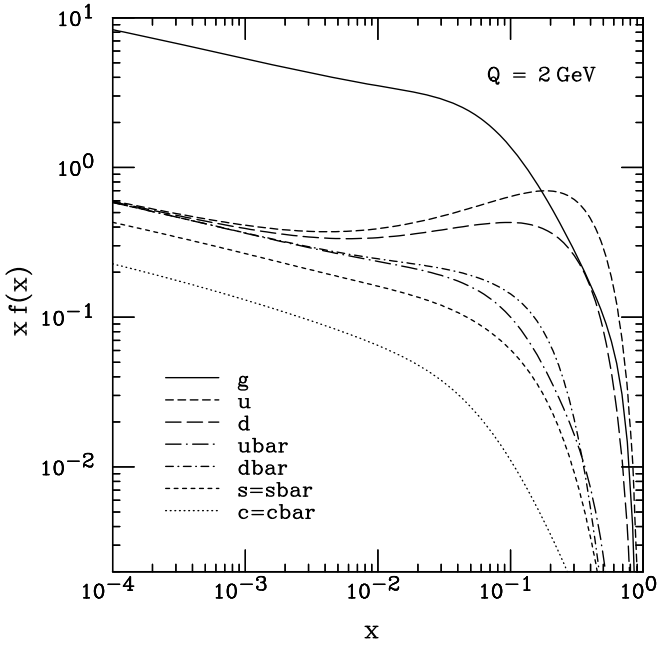

Figure 3.7: Typical Parton Distribution Functions for several partons as a function of $x = E_{parton}/E_{proton}$, taken from Ref. [62].

One of the advantages of the helicity amplitudes method is that one has the possibility to extract from them a cross section for a given polarization state. This is explored by us further on in Sec. 3.3.4 for the longitudinal Z polarization study. If one sums over all the polarization final states the $f\bar{f} \to ZZ$ differential cross section in the ZZ center-of-mass system can be given [52] in terms of the Mandelstam variables [63] by

$$\frac{d\sigma(ZZ)}{dcos\theta_Z} = \frac{\pi\alpha^2 C}{\hat{s}^2}(\hbar c)^2 \frac{g_L^4 + g_R^4}{sin_W^2 cos_W^2} \times \left[\frac{t}{u} + \frac{u}{t} + 4M_Z^2\frac{\hat{s}}{tu} - M_Z^4\left(\frac{1}{t^2} + \frac{1}{u^2}\right)\right]\frac{dt}{dcos\theta_Z} \tag{3.10}$$

where g_L and g_R are the Left and Right couplings of the fermions to the Z boson as given in Sec. 3.1.

As an example for the differential cross section we present in Fig. 3.10 the $d\sigma(u\bar{u} \to ZZ)/dcos\theta_Z$ as calculated from Eqs. (3.7) and (3.9) using Table 3.4. This cross section is shown for three different $\sqrt{\hat{s}_{ZZ}}$ values. To note is that the forward angular distribution enhancement increases with energy.

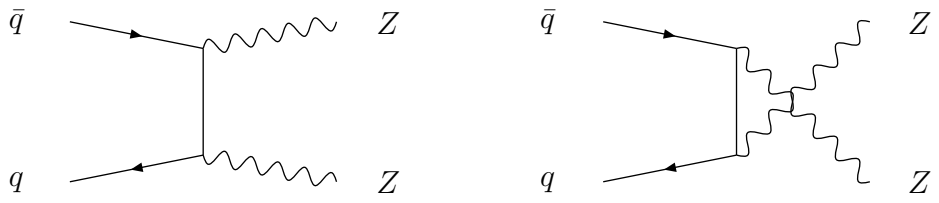

Figure 3.8: The SM lower order t- and u-channel diagrams for ZZ pair production in $q\bar{q}$ collisions.

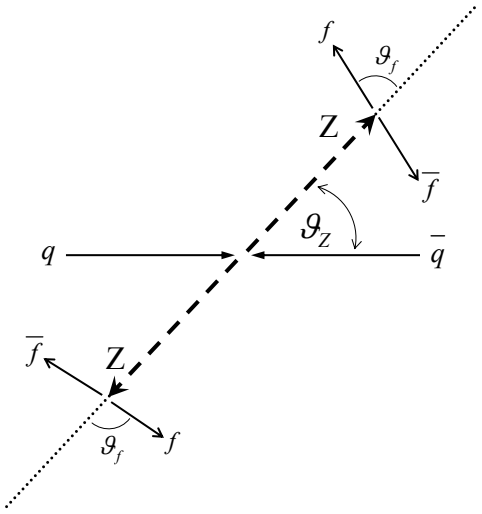

Figure 3.9: Schematic view of the process $q\bar{q} \rightarrow ZZ \rightarrow f\bar{f}$ production in a polar angle θ_Z. In addition the $Z \rightarrow f\bar{f}f'\bar{f}'$ polar decay angle θ_f is defined in the CM of its Z boson parent.

3.3.3 Total cross sections

The total cross section of $\sigma(q\bar{q} \rightarrow ZZ)$ can be derived from Eq. (3.7) by integrating over $cos\theta_Z$. The expected total cross section, in the range of $\sqrt{\hat{s}_{ZZ}}$ from threshold to 750 GeV is shown in Fig. 3.11. In order to avoid the pole at $\theta_Z = 0$ and to account for the loss of events were particles enter the beam pipe we have introduced a cut of $|cos\theta_Z| < 0.98$ in our helicity

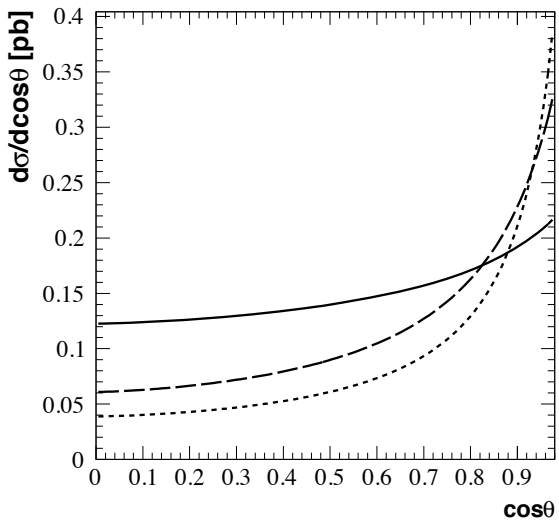

Figure 3.10: The $u\bar{u} \to ZZ$ differential cross section in the CM system. The solid, dashed and dotted lines represent the distributions at the $\sqrt{\hat{s}_{ZZ}}$ energies of 200, 250 and 300 GeV respectively.

amplitude calculations. The high energy of a pp collider like the LHC provides the possibility to study the ZZ system beyond the LEP2 upper limit of about 200 GeV.

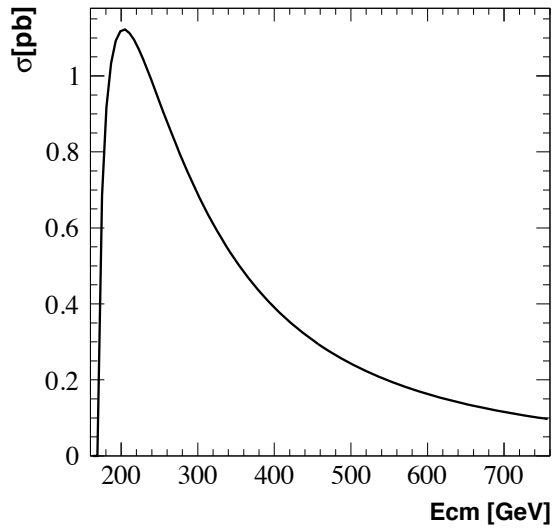

Figure 3.11: The helicity amplitude calculated $\sigma(q\bar{q} \to ZZ)$ shown as a function of the ZZ center of mass system ($Ecm = \sqrt{\hat{s}_{ZZ}}$).

3.3.4 The Z longitudinal polarization

In the absence of polarization each helicity state have the same probability to occur. When one of the helicity states is dominating, one refers to it as the polarization direction of the particle. The expected Z longitudinal polarization can be calculated via the helicity amplitude method. For a given polar angle $cos\theta_Z$ the single Z and joint ZZ longitudinal polarizations $\rho_{00}(cos\theta_Z)$ and $\rho_{0000}(cos\theta_Z)$ are given by

$$\rho_{00}(cos\theta) = \frac{\sum_{\lambda\lambda'\tau'} |F_{\lambda\lambda' 0\tau'}(cos\theta_Z)|^2}{\sum_{\lambda\lambda'\tau\tau'} |F_{\lambda\lambda'\tau\tau'}(cos\theta_Z)|^2} \quad \text{and} \quad \rho_{0000}(cos\theta) = \frac{\sum_{\lambda\lambda'} |F_{\lambda\lambda' 00}(cos\theta_Z)|^2}{\sum_{\lambda\lambda'\tau\tau'} |F_{\lambda\lambda'\tau\tau'}(cos\theta_Z)|^2} \,. \tag{3.11}$$

In Fig. 3.12 the expected ρ_{00} and ρ_{0000} polarizations averaged over $cos\theta_Z$ are given as a function of $\sqrt{\hat{s}_{ZZ}}$.

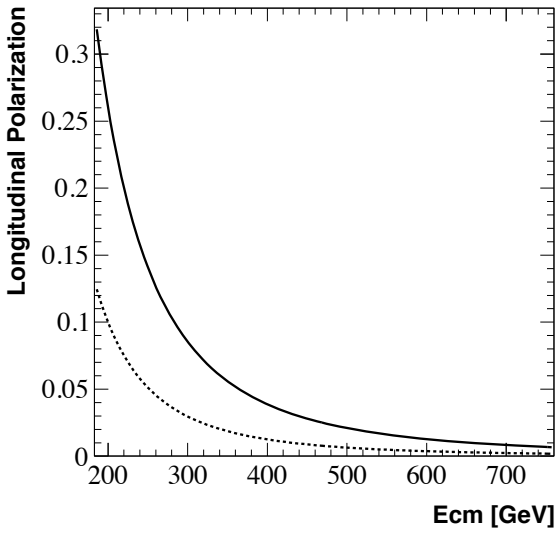

Figure 3.12: The expected Z longitudinal polarizations at 14 TeV averaged over $cos\theta_Z$ estimated via the helicity amplitude method. The continues and dashed lines represent respectively the single, ρ_{00}, and the joint, ρ_{0000}, polarizations.

		$\tau=\tau'=\pm1$	$\tau=-\tau'=\pm1$	$\tau=\tau'=0$	$\tau=0,\ \tau'=\pm1$	$\tau=\pm1,\ \tau'=0$
	1	$\dfrac{-e^2\hat{s}\lambda}{2}sin\theta$	$\dfrac{-e^2\hat{s}\lambda}{2}sin\theta$	$\dfrac{-e^2\hat{s}\lambda}{2}sin\theta$	$\dfrac{-e^2\hat{s}\lambda}{2}\dfrac{(\tau' cos\theta-2\lambda)}{\sqrt{2}}$	$\dfrac{-e^2\hat{s}\lambda}{2}\dfrac{(\tau cos\theta+2\lambda)}{\sqrt{2}}$
T	$\dfrac{4\lambda a_{Zi}b_{Zi}-a_{Zi}^2-b_{Zi}^2}{t}$	$cos\theta-\beta$	$-cos\theta-2\lambda\tau$	$\dfrac{\hat{s}}{2m_Z^2}\left[cos\theta-\beta\left(1+\dfrac{2m_Z^2}{\hat{s}}\right)\right]$	$\dfrac{\sqrt{\hat{s}}}{2m_Z}\left[cos\theta(1+\beta^2)-2\beta\right]$ $\dfrac{2m_Z\tau' sin^2\theta}{\sqrt{\hat{s}}(\tau' cos\theta-2\lambda)}$	$\dfrac{-\sqrt{\hat{s}}}{2m_Z}\left[cos\theta(1+\beta^2)-2\beta\right]$ $+\dfrac{2m_Z\tau sin^2\theta}{\sqrt{\hat{s}}(\tau cos\theta+2\lambda)}$
U	$\dfrac{4\lambda a_{Zi}b_{Zi}-a_{Zi}^2-b_{Zi}^2}{u}$	$cos\theta+\beta$	$-cos\theta-2\lambda\tau$	$\dfrac{\hat{s}}{2m_Z^2}\left[cos\theta+\beta\left(1+\dfrac{2m_Z^2}{\hat{s}}\right)\right]$	$\dfrac{\sqrt{\hat{s}}}{2m_Z}\left[cos\theta(1+\beta^2)+2\beta\right]$ $\dfrac{2m_Z\tau' sin^2\theta}{\sqrt{\hat{s}}(\tau' cos\theta-2\lambda)}$	$\dfrac{-\sqrt{\hat{s}}}{2m_Z}\left[cos\theta(1+\beta^2)+2\beta\right]$ $+\dfrac{2m_Z\tau sin^2\theta}{\sqrt{\hat{s}}(\tau cos\theta+2\lambda)}$

Table 3.4: The helicity amplitude table for the $q\bar{q}\rightarrow ZZ$ production taken from Ref. [64].

Chapter 4

The simulated data sample

In this work we utilize the so called "gold plated events" where the Z boson pairs are observed through their decay into two pairs of muons. These muons are among the best identified particles in the ATLAS detector since they are required to traverse through all the detector elements and leave a track in the outer muon spectrometers (see Fig. 4.1).

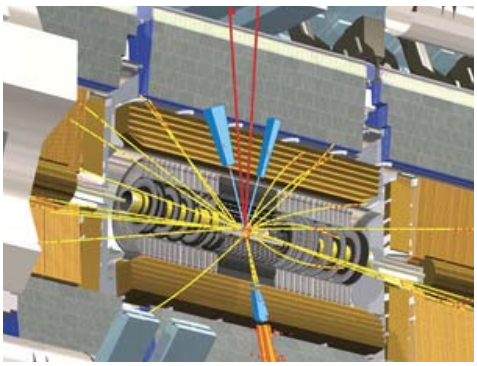

Figure 4.1: A side view of a $ZZ + X \rightarrow \mu^+\mu^- e^+ e^- + X$ event in ATLAS.

The expected number N of produced events for a given reaction is estimated by

$$N = \mathcal{L} \times \sigma \times BR \tag{4.1}$$

were $\mathcal{L}$ is the integrated luminosity, σ is the cross section of the process and BR is the Branching Ratio of the chosen decay mode. In our analyses we have

utilized the number of Z pair events produced from the LHC planned integrated luminosity of 100 $fb^{-1}/year$ and also considered a higher luminosity of 300 $fb^{-1}/year$. The leptonic branching ratios to electrons and muons of the ZZ, WZ and WW final states are listed in Table 4.1. Also in the table are given the number of expected events corresponding to 100 fb^{-1} calculated by the bolded cross section values given in Table 3.3.

	$ZZ \to l^+l^-l^+l^-$	$W^\pm Z \to l^\pm \nu l^+ l^-$	$W^+W^- \to l^+\nu l^-\nu$
BR	0.0045	0.0142	0.0447
$\sigma \times$BR[pb]	0.057	0.440	3.376
No. Events	~5,700	~44,000	~337,600

Table 4.1: The production cross sections [56] given by the bolded numbers in Table 3.3, multiplied by the charge leptonic (e/μ) BR [49] in pp collision at 14 TeV. Also given are the corresponding number of produced events for an integrated luminosity of $\mathcal{L}$=100 fb^{-1}.

For the efficiency estimation of both the identification and selection procedures we have used a large sample of 41,150 MC events[1] of the reaction $pp \to ZZ \to l^+l^-l^+l^-$ (were $l = e$ or μ) produced at $\sqrt{s_{pp}}$ of 14 TeV. From this sample about 10,300 are of the type $pp \to ZZ \to \mu^+\mu^-\mu^+\mu^-$ events[2]. The large sample of 41,150 events corresponds to a luminosity of about 720 fb^{-1} and a ZZ cross section of 12.7 pb. However for the physics analysis we have only utilized samples that corresponds to integrated luminosity of 100 fb^{-1}.

4.1 Muon identification and its reconstruction

For the production of $pp \to ZZ$ sample the Pythia 6.4 MC generator program [65] was used, which is based on the Lund model [66]. This MC generator

[1]The official ATLAS dataset number and name was given as 5980 and Pythiazz4l.

[2]This reaction is in fact $pp \to ZZ + X \to \mu^+\mu^-\mu^+\mu^- + X$ but for simplicity the accompanied additional particles X are omitted

utilizes the PDF package CTEQ6L1 [62] which includes the Z/γ^* interference (see page 180 in Ref. [65]). Since most of the MC processing time is spent on the detector simulation step the events are pre-filtered at the generation level so that only events with four leptons and within $|\eta| < 2.7$ and $p_T > 5\ GeV$ are selected. These events are further passed through the full simulation of the ATLAS detector and finally reconstructed by the various ATLAS algorithms to produce the standard output. All ATLAS generators, MC simulation and reconstruction algorithms are included in the ATLAS software framework, Athena [67].

The muon reconstruction algorithms are described in details in the published manuals [42, 68]. These programs can be divided into two categories. The first one uses the hits collected by the outer muon MDT detectors to construct a muon track. The second category contains programs that associate the outer muon track with its Inner Detector track. Each muon reconstruction algorithm was tested with different physics processes that decay leptonically like: $pp \rightarrow t\bar{t}$ and $pp \rightarrow J/\psi$ [68]. The $t\bar{t}$ sample was chosen to represent the main SM/QCD process while the J/ψ sample represents low p_T events due to its relative small mass.

Two of the important properties of these algorithms, the muon transverse momentum resolution and the efficiency, are summarized in Table 4.2 and presented in Fig. 4.2. In this figure the reconstructed muons momentum resolution is shown for the $t\bar{t}$ sample as a function of η and p_T. As can be seen, the sensitivity is lower in the overlap region between the barrel and the endcap ($1.2 < |\eta| < 1.7$) which can be understood in terms of the reduction of material in the end-cap toroid and consequently in its smaller number of measured hits and the fact that some of the end-cap chambers were absent in the simulation used in this work.

Table 4.2, which was summarized from Ref. [68], presents very similar merged muons[3] efficiencies and fake rates for two reconstruction packages and

[3]A merge muon is a reconstructed muon in the MDT that was associated with an inner detector track.

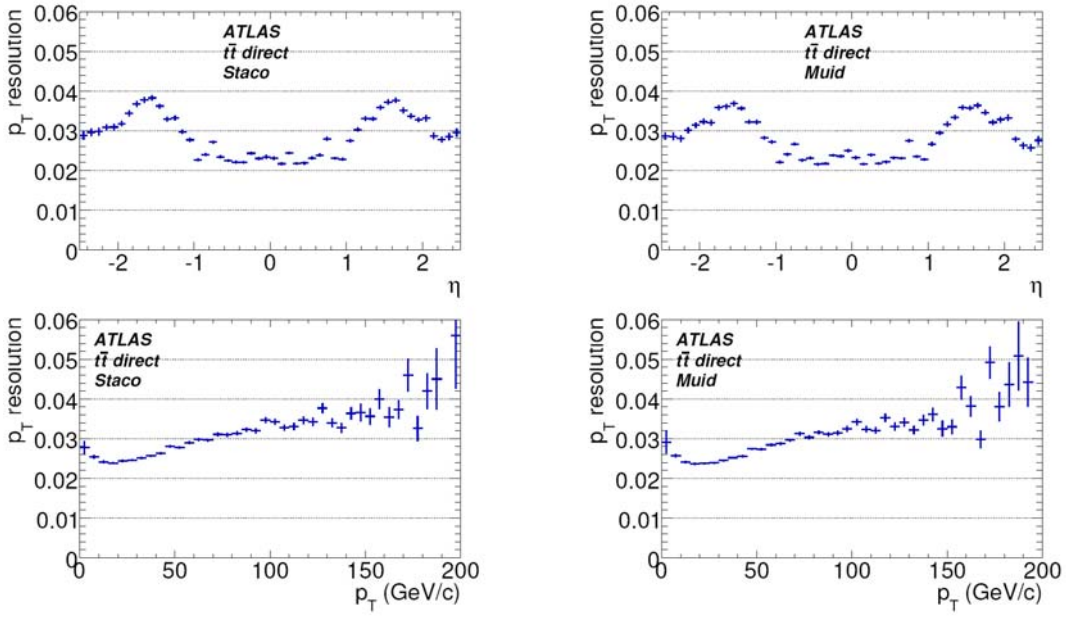

Figure 4.2: The muon transverse momentum reolution ($\Delta p_T/p_T$) as a function of η (top) and p_T (bottom), for the two muon reconstruction packages, 'Staco' (left) and 'Muid' (right), taken from [68] which are compared in Table 4.2 (see text).

for the two different physics processes. These efficiency values lie between 87 and 90% for the processes examined. The fake rate shown in the table are only for muons with a $p_T > 20\ GeV$ which are identical to the trigger condition requirements used in our selection. Here is the place to note that there is an additional muon reconstruction algorithm known under the name 'muGirl' which was designed to do inside-to-outside muon tracks reconstruction with the ATLAS detector.

4.2 Properties of the $Z \to \mu^+\mu^-$ decay

The reaction $pp \to Z \to \mu^+\mu^-$ is one of the first processes that were measured from the data taken by the ATLAS muon spectrometers [69] and is used as a "standard candle"[4]. From these measurements the experimental resolution of

[4]A process that is used in the calibration and alignment procedure of the ATLAS detector is refereed to as a "standard candle".

Sample	Efficiency	Fakes/(1000 events) with $p_T(\mu) > 20$ $[GeV]$
Staco		
$t\bar{t}$	0.876	6.1
J/ψ	0.883	0.1
Muid		
$t\bar{t}$	0.898	8.4
J/ψ	0.885	0.0

Table 4.2: The muon reconstruction efficiency for two main muon reconstruction packages and for two different physics processes. In addition, the fake rates of muons that have a $p_T > 20$ GeV, are also listed.

Γ_Z, the Z width can be extracted. This width value, as shown further, is an essential parameter in our selection procedure.

To study Γ_Z we have utilized a MC reconstructed Z pair events where one decays to a $\mu^+\mu^-$ pair and the other one to a pair of e^+e^-. In this way we collected a Z sample with a unique $\mu^+\mu^-$ pairing. The invariant mass of these selected events are shown in Fig. 4.3. As can be seen, there is a slight asymmetry between the higher and lower mass regions around the Z signal. A comparison between the energy distributions of the muons from the high and low mass wings of the resonance is presented in Fig. 4.4. The low mass distribution ($M_{\mu^+\mu^-} < 88$ GeV) is plotted by the dashed line has a mean value of 96.8 GeV while the high mass distribution ($M_{\mu^+\mu^-} > 94$ GeV) that is plotted by a continuous line has a mean value of 113.4 GeV. This effect is mainly due to the energy loss of one of the final state muons. For the determination of the resonance width we have first tried a Gaussian distribution but found a much better fit by the use of a Breit-Wigner shape plus a polynomial background to the mass distribution the result of which is shown in Fig. 4.3 by the continuous line. This fit, with χ^2/dof of 23.9/23, yielded a Z mass value of 91.25$\pm$0.16 GeV which is in a very good agreement with the M_Z value of 91.18 GeV [49] embedded in the MC. In addition, the simulated experimental

Z width was found to be Γ_Z=5.52±0.30 GeV as compared to its official value of 2.49 GeV [49] which implies at this mass region an experimental energy resolution of about 4.92 GeV. From this follows that the half width at half maximum of the mass distribution is $\sigma_Z^{Exp} = 2.76\ GeV$ (In this work when ever we used the superscript Exp we relate to the simulated data sample) .

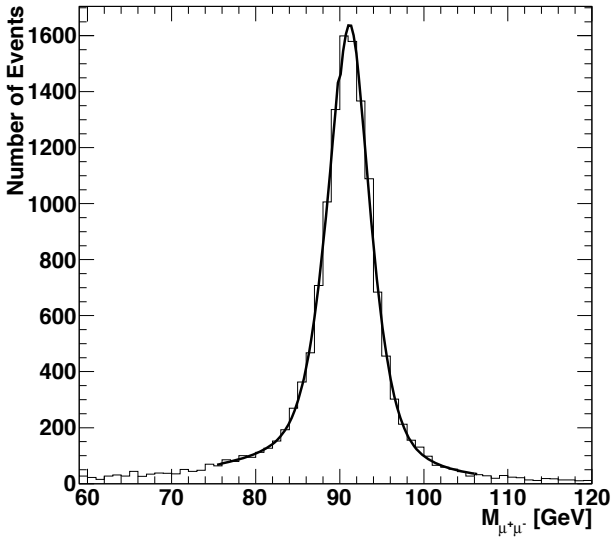

Figure 4.3: The invariant mass of all pairs of opposite charged muons found in the single Z sub-sample (see text). The continuous line is a result of a Breit-Wigner fit plus a polynomial background distribution that yielded M_Z=91.25±0.16 GeV and Γ_Z=5.52±0.30 GeV with χ^2/dof of 23.9/23.

4.3 The selection procedure

4.3.1 Overview

The event selection procedure was carried out in three steps. In the first one the condition of the trigger has been imposed. This was followed by the requirement that each event should contain at least $2\mu^+$ and $2\mu^-$ reconstructed tracks. In the last step the final identification was achieved by demanding that the two pairs of $\mu^+\mu^-$ invariant masses lie within the chosen Z mass range. In

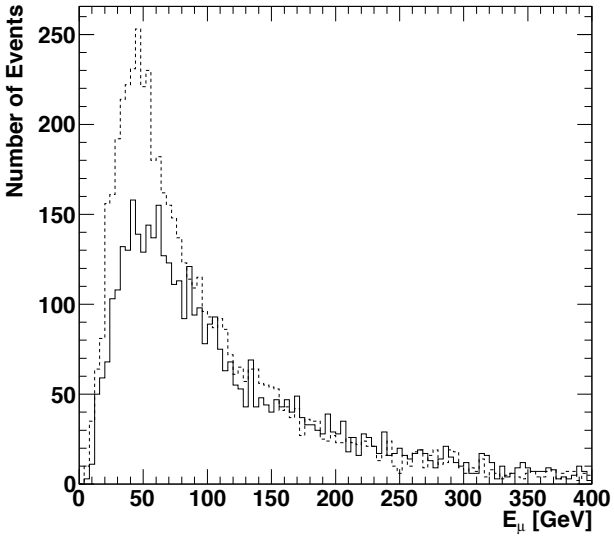

Figure 4.4: Energy distributions of the muons in the lower and higher mass regions of a single Z resonance. The low mass region distribution with a mean value of 96.84 GeV is given by the dotted line. The high mass region distribution is represented by a continuous line and has a mean value of 113.40 GeV.

our analysis, we have utilized two invariant mass ranges, the tight one which was 91.18 $GeV \pm 3\sigma_Z^{Exp}$ and the loose one which was 91.18 $GeV \pm 5\sigma_Z^{Exp}$. From the fit results described in section 4.2 we have determined the two mass ranges to be $79 < M_Z < 105$ GeV and $83 < M_Z < 100$ GeV respectively. Following these steps it was found that the selection efficiency for the loose mass range was about 43% while that of the tight mass selection was around 39%.

4.3.2 The ATLAS trigger

The ATLAS detector records a pp reaction according to a chosen trigger algorithm [55]. This algorithm contains a variety of trigger menus that are aimed for different physics topics. For the study of the reaction $pp \rightarrow ZZ \rightarrow muons$ we utilized the ATLAS High Level Trigger (HLT) menu, "mu20", which is set to trigger on events identified by the HLT to have at least one combined muon with $p_T > 20$ GeV. This menu is used for the study of heavy particles, such as the Z and $W^{\pm}$ gauge bosons as well as for the Top-quark in their decay to muons. This condition which is automatically satisfied by all our selected

events also suppresses the contribution from unwanted background sources.

4.3.3 The muons pairing and invariant mass cuts

At the second step events that did not have at least $2\mu^+$ and $2\mu^-$ reconstructed tracks were rejected so that $\sim$15% of the events were removed. The next step was divided in two parts. In the first one we selected two pairs of opposite charge muons which were taken to be a Z pair candidate. In the second part we verified that each Z candidate had an invariant mass in the chosen range. This last step was found to be the most important one in the selection procedure.

4.3.4 Ambiguity in the pairing procedure

There were cases where one did not find a unique solution in the pairing procedure. The fraction of these events were 7% and 17% respectively for the tight and loose mass ranges. In this case we have selected those muon combinations which yielded the Z masses nearest to its value of $M_Z = 91.18\ GeV$.

4.3.5 Number of events used in the analysis

In a luminosity of 100 fb^{-1} one expects 1,421 MC generated $pp \rightarrow ZZ \rightarrow \mu^+\mu^-\mu^+\mu^-$ events at 14 TeV for the physics analyses. After the ATLAS reconstruction stage a total of 1,214 events with at least $2\mu^+$ and $2\mu^-$ are left. Next the pairing procedure has been applied for the two selected Z mass regions which yielded 614 and 557 events for the conservative loose and tight mass cuts respectively. The sequence of this event selection is summarized for convenience in Table 4.3. Note that if one is able to add the $Z \rightarrow e^+e^-$ decay events to the analyzed sample an increase of up to a factor of four will result in the number of available events.

	Number of events	
Generated $pp \to ZZ \to \mu^+\mu^-\mu^+\mu^-$	1,421	
At least $2\mu^+$ and $2\mu^-$ reconstructed tracks	1,214	
Invariant mass cut	Loose	Tight
Paring procedure	614	557

Table 4.3: The selection sequence and corresponding number of $pp \to ZZ \to \mu^+\mu^-\mu^+\mu^-$ events for an integrated luminosity of $\mathcal{L} = 100\ fb^{-1}$.

4.4 Background contributions

The main background to the present study of the production of ZZ via $q\bar{q}$ interaction is its production via gluon fusion (gg). At 14 TeV this background was estimated by different authors [70–72] to be between 20-25% (see e.g. Fig. 4.5). It is expected that the amount of this background can be further reduced by appropriate cuts such as on the rapidity parameter. The usefulness of this cut can be deduced from the theoretical studies of ZZ production reported in Ref. [70] and shown in Fig. 4.6 for $\sqrt{s_{pp}} = 16\ TeV$. After such a cut the remained gg background contribution will have to be subtracted directly from the various physics quantities under study. At present it is obvious that there is still a need for theoretical estimation of the gluon fusion to the ZZ final state.

Other sources of background to be considered are coming from the $pp \to t\bar{t} \to 2\mu^-2\mu^+$ and the $pp \to Zb\bar{b} \to 2\mu^-2\mu^+$ processes [73]. The background of the t-quark arises from its decay to a $W^{\pm}b$ both followed by their leptonic decays which may include two pairs of opposite charged muons. To study this background we utilized the available $pp \to t\bar{t}$ MC samples of about 556,000 events produced at 10 TeV and 22,300 events produced at 14 TeV. At 10 TeV with a tight mass range no background contribution was found. In the loose mass range a non-zero but nevertheless negligible amount of background events were observed. In the sample of about 22,300 events at 14 TeV no background contribution to the ZZ events was found in both chosen mass cuts. Obviously a larger sample of $t\bar{t}$ events may improve the assessment of this possible con-

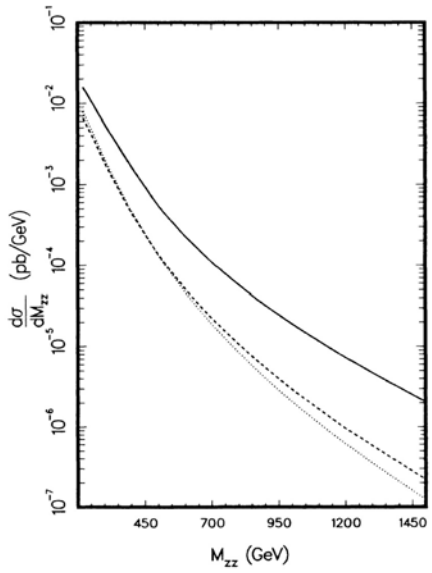

Figure 4.5: The ZZ production cross sections as a function of M_{ZZ} for $\sqrt{s_{pp}} = 10\ TeV$ and $|\eta| < 1.5$ taken from Ref. [71]. The solid line represents the contribution of the $q\bar{q} \rightarrow ZZ$ process. The doted and dashed lines represents the $gg \rightarrow ZZ$ contribution respectively for M_t=40 GeV and M_t=100 GeV.

tamination. After taking into account the $t\bar{t}$ and ZZ production cross sections and their branching ratios into muons we estimated that the $t\bar{t}$ background in our analysis to be 9%. Concerning the $Zb\bar{b}$ source it was found that it is mostly removed by the invariant mass cut which leaves a background of about 6%.

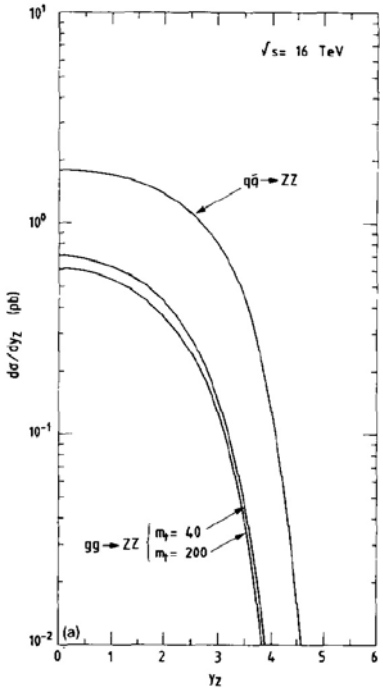

Figure 4.6: The rapidity Yz distribution of the Z-bosons produced via $gg \rightarrow ZZ$ and $q\bar{q} \rightarrow ZZ$ in pp collisions at $\sqrt{s} = 16\ TeV$, taken from Ref. [70].

Chapter 5

Physics analysis

In this chapter we utilized the selected $pp \to ZZ \to \mu^+\mu^-\mu^+\mu^-$ events to evaluate the differential and total cross sections with the use of the helicity amplitude technique and their relation to the fundamental $q\bar{q} \to ZZ$ process. In addition the longitudinal polarization of the final state Z gauge bosons is also estimated.

5.1 Transformation of the $pp \to ZZ$ to the $q\bar{q} \to ZZ$ reactions

In general, theoretical calculations of cross sections and other properties of parton anti-parton reactions leading to exclusive final states, such as $\bar{q}q \to ZZ$, are carried out in their center of mass energy, Ecm. In the study of the proton-proton collisions, at a given center of mass energy $\sqrt{s_{pp}}$, the Ecm can be determined event by event from the momenta of the final state particles. Thus it is needed to be able to transform the pp cross sections to their fundamental ones.

Here it is important to note that the partons in the proton have a continuous energy spectrum which are parametrized by the Parton Density Functions, PDF. These functions describe the relative parton energy E_{parton} with respect to the proton energy E_{proton} namely $x = E_{parton}/E_{proton}$. As a consequence, in the interacting pp system exists an infinite continuous set of colliding parton

anti-parton pairs with the identical Ecm value. This energy distribution is described here by the so called Energy Density Functions, EDF [74]. It is important to stress that the EDF is a property of the two colliding protons and clearly is not equivalent to the PDF, which is a property of the single non-reacting proton. However, the PDF is an essential input to the EDF determination which is crucial for the transformation from pp to their basic $q\bar{q}$ reactions and vice versa. Note that the larger the energy range on which the polarization measurement is averaged, the more it is sensitive to the EDF transformation (see Sec. 5.4) .

5.1.1 Evaluation of the Energy Density Functions

In the study of exclusive pp reactions via a dedicated MC program the $\bar{q}q$ repetition of a same Ecm value is automatically guarantied. Such a dedicated MC program, which is time consuming and frequently requires special development efforts, is often not readily available for the particular reaction under study, so that an evaluation of the EDF is inevitable and hence it is here further estimated.

If we denote by S the center of mass energy squared of the colliding pp system, assumed to be the original planned LHC energy squared of $(14\,TeV)^2$, and by $\hat{s}$ $(= Ecm^2)$ the center of mass energy squared of the incoming parton anti-parton pair, then the following relation holds:

$$\hat{s} \;=\; x_k x_{\bar{k}} S \;, \tag{5.1}$$

where $x_k \;=\; E_k/E_{proton}$ is the fraction of the proton energy carried by the parton k. For the different Parton Distribution Functions, here denoted by $h_k(x_k)$, we have used the ones given by CTEQ6.5M [75]. For a fixed S, the probability to obtain $\hat{s}$ is given by [74]

$$P(\hat{s},S)d\hat{s} \;=\; \frac{\int_{min}^{1} dx_k \int_{min}^{1} dx_{\bar{k}}\; [h_k(x_k)\bar{h}_{\bar{k}}(x_{\bar{k}})\delta(x_k x_{\bar{k}} - \hat{s}/S)]d\hat{s}}{\int_{\hat{s}_{min}}^{\hat{s}_{max}} d\hat{s} \int_{min}^{1} dx_k \int_{min}^{1} dx_{\bar{k}}\; [h_k(x_k)\bar{h}_{\bar{k}}(x_{\bar{k}})\delta(x_k x_{\bar{k}} - \hat{s}/S)]} \;, \tag{5.2}$$

where the lower positive integration limits of dx_k should be set to a very small but non zero value, in order to avoid in the numerical calculations the poles at $x = 0$. To note is that these two last formulae are also valid for

the $gluon - gluon$ (gg) collisions. From the probability distribution $P(\hat{s}, S)$ we derive the parton anti-parton center of mass Energy Density Functions, $EDF(k\bar{k})$, for pp collisions at 14 TeV which can be parameterized above the ZZ threshold as [74]

$$EDF_{u\bar{u}} \simeq \frac{1}{N_{u\bar{u}}} \frac{3.9 \times 10^4}{Ecm^{2.5}}; \quad EDF_{d\bar{d}} \simeq \frac{1}{N_{d\bar{d}}} \frac{1.956 \times 10^4}{Ecm^{2.5}}; \quad EDF_{s\bar{s}} \simeq \frac{1}{N_{s\bar{s}}} \frac{1.5 \times 10^4}{Ecm^{2.75}}, \tag{5.3}$$

where $1/N_{ij}$ are the normalization factors for the colliding $k_i k_j$ partons which depend on $\sqrt{\hat{s}_{min}}$ and $\sqrt{\hat{s}_{max}}$. The EDF expressions for the quark anti-quark systems $d\bar{u}$ and $u\bar{d}$, as well as the $g\bar{g}$ are given by

$$EDF_{d\bar{u}} \simeq \frac{1}{N_{d\bar{u}}} \frac{1.9 \times 10^4}{Ecm^2}; \quad EDF_{u\bar{d}} \simeq \frac{1}{N_{u\bar{d}}} \frac{4.1 \times 10^4}{Ecm^2}; \quad EDF_{gg} \simeq \frac{1}{N_{gg}} \frac{55 \times 10^4}{Ecm^{2.35}}. \tag{5.4}$$

The unnormalized Energy Density Functions are shown in Fig. 5.1 as a function of Ecm. These parameterized EDF expressions are applied in Secs. 5.2 and 5.4 for the case of the ZZ pairs final state.

5.1.2 Verification of the EDF procedure from the ZZ production in $q\bar{q}$ and pp collisions

The reliability of our derived EDF expressions to transform the parton anti-parton cross sections to the corresponding pp reactions is demonstrated in Fig. 5.2. In this figure the expected helicity amplitude calculations for the $q\bar{q} \to ZZ$ cross section as a function of the Ecm is given by the continuous line. This $q\bar{q}$ cross section is transformed via the relative EDF to obtain the corresponding $\sigma(pp \to q\bar{q} \to ZZ)$ distribution shown by the dotted line in the same figure. This expected distribution is further compared to a histogram of ∼38,000 MC events generated with Pythia 6.403 that utilized the PDF package CTEQ6L1 [62]. To note is that both helicity amplitude expectations are normalized to the area under the histogram of the MC sample. As can be seen, there is an overall agreement between the MC sample and the expected $pp \to ZZ$ cross section. The slight deviation between the EDF treated cross section and that of the MC generated sample can be traced back among other reasons to the approximate numerical evaluation of the integrals given in Eq. (5.2) and to the difference between the PDF version incorporated in the MC

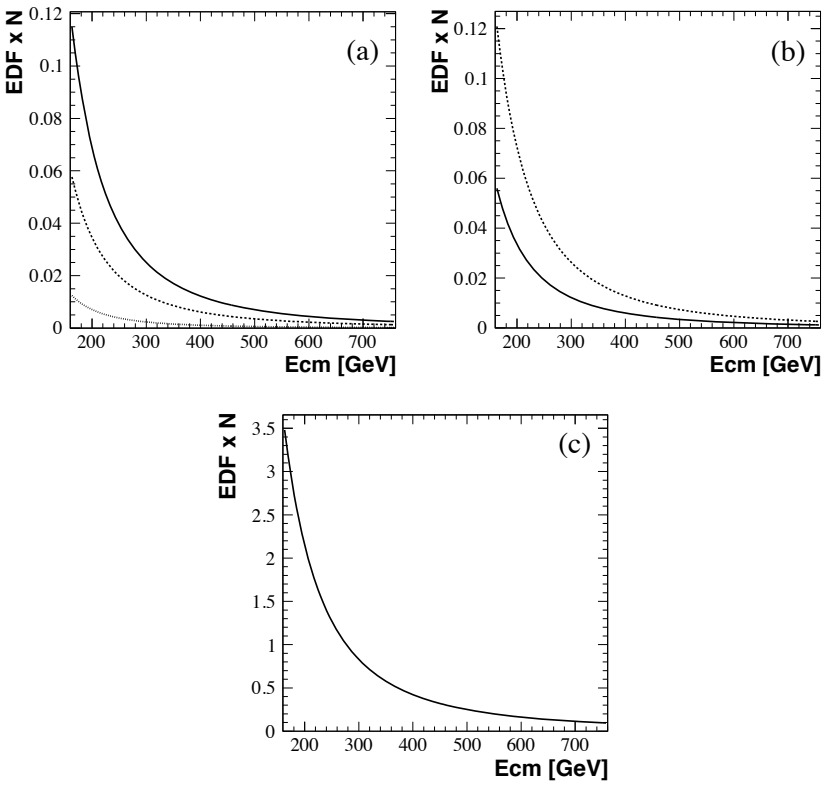

Figure 5.1: The unnormalized parton anti-parton Energy Density Function, $EDF \times N$ as a function of Ecm for pp interactions at a $\sqrt{s_{pp}} = 14$ TeV taken from Ref. [74]. (a) The continuous, dashed and dotted lines are respectively the $EDF_{k\bar{k}} \times N_{k\bar{k}}$ dependence on Ecm of the $u\bar{u}$, $d\bar{d}$ and $s\bar{s}$ systems, (b) The continuous and dashed lines are respectively the $EDF_{k\bar{k}} \times N_{k\bar{k}}$ dependence on Ecm of the $d\bar{u}$ and $u\bar{d}$ systems, (c) The $gluon - gluon$ $EDF_{gg} \times N_{gg}$.

program and that used by us.

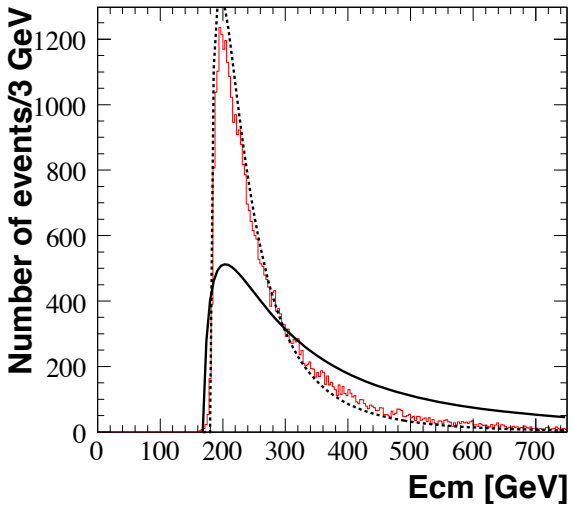

Figure 5.2: The expected $\sigma(q\bar{q} \rightarrow ZZ)$ helicity amplitude calculations and its corresponding $\sigma(pp \rightarrow q\bar{q} \rightarrow ZZ)$ distribution given respectively by the continuous and dotted lines. In addition a $\sigma(pp \rightarrow q\bar{q} \rightarrow ZZ)$ histogram distribution of the MC sample is also presented. All cross sections are for $\sqrt{s_{pp}}$=14 TeV where both areas under the lines are normalized to that of the MC data histogram. For further details see.

5.2 Cross sections

The ZZ system in its decay to $l^+l^-l^+l^-$ allows a straight forward determination of the center of mass energy event by event. Throughout our analysis we have considered two Z invariant mass width cuts (discussed earlier in Sec. 4.3) and two integrated luminosity values namely, 100 fb^{-1}/year which is the designed value of the LHC and a higher value of 300 fb^{-1}/year.

5.2.1 The differential cross section $d\sigma(pp \rightarrow ZZ)/dcos\theta_Z$

The $q\bar{q} \rightarrow ZZ$ differential cross section can be determined via the measured outgoing ZZ center-of-mass system, $\sqrt{\hat{s}_{ZZ}} = \sqrt{\hat{s}_{q\bar{q}}}$. To compare and fit our MC measured differential cross sections to the theoretical expectations we have followed several steps.

In the first step we have assigned the muons to their corresponding bosons after which we have transformed them to the ZZ center-of-mass system and plotted the differential cross section as a function of $cos\theta_Z$ while summing up over all azimuthal angles. Here θ_Z is the polar production angle of the ZZ event with respect to the $q\bar{q}$ collision line (see Fig. 3.9). The limited number of events did not allow us to study the differential cross sections at fine energy bins and therefore we have grouped them into two energy regions namely, 180-245 GeV and 245-300 GeV with the average values of 211 GeV and 269 GeV respectively. Here is the place to stress that these average values include both the intrinsic $q\bar{q}$ energy dependence and its frequency occurrence in pp reaction delt with by the EDF (Sec. 5.1).

Next we have calculated the expected helicity differential cross section as a function of $cos\theta_Z$ for the two average energy values. To examine our sensitivity to the presence of nearby bosons 'Beyond the SM', which could interfere, we have set the Z boson mass to be a free parameter in our analysis fits. These analyses took into account only the shape of the differential cross sections so that the normalization remained a free parameter in the fit.

As can be seen from Fig. 3.10, the theoretical ZZ differential cross section is expected to increase in the forward direction as the energy increases. This behavior is not observed in our measured differential cross sections (e.g. see Fig. 5.3) which we found to be due to a large loss of events increasing with the ZZ invariant mass, mainly around $cos\theta_Z$=1. This loss is a manifestation of the current poor detection efficiency of high energy muons in the very forward direction. Hence we limited our fits to the ranges of $0 < cos\theta_Z < 0.98$ for the 180-245 GeV samples and $0 < cos\theta_Z < 0.84$ for the 245-300 GeV samples.

The result of all the fits to M_Z with their statistical errors are listed in Table 5.1 and presented in Figs. 5.3-5.6. In Figs. 5.3 and 5.4 the loose and tight invariant Z mass cuts are shown for the integrated luminosity of 100 fb^{-1}, while Figs. 5.5 and 5.6 show the loose and tight cuts for the integrated luminosity of 300 fb^{-1}. The solid and dashed lines in the figures represents the fits results respectively for the 180-245 GeV and the 245-300 GeV energy

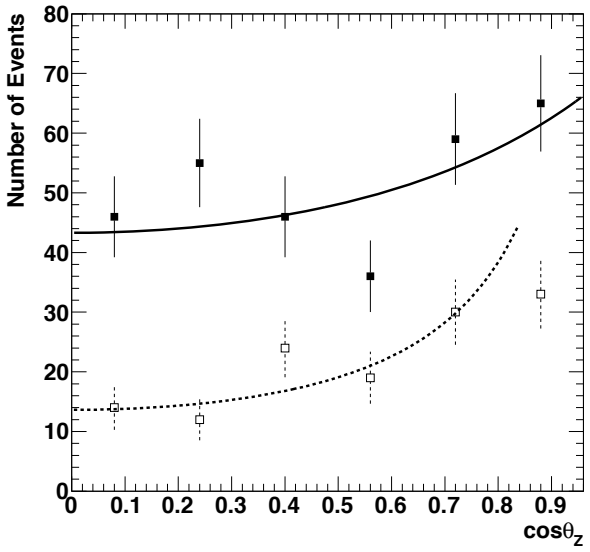

Figure 5.3: The differential cross sections for the loose invariant mass cut as a function of $cos\theta_Z$ for an integrated luminosity of 100 fb^{-1}. The solid and dashed lines represent respectively the 180-245 GeV and the 245-300 GeV energy ranges.

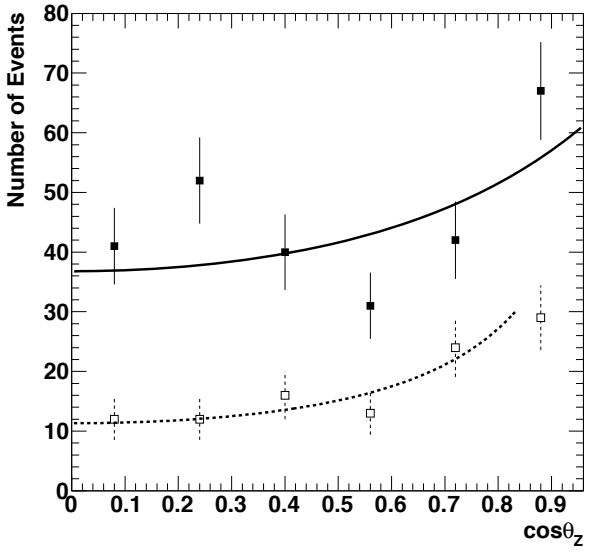

Figure 5.4: The differential cross sections for the tight invariant mass cut as a function of $cos\theta_Z$ for an integrated luminosity of 100 fb^{-1}. The solid and dashed lines represent respectively the 180-245 GeV and the 245-300 GeV energy ranges.

$\mathcal{L}$uminosity	Invariant mass cut		Energy Range	
			180-245 GeV	245-300 GeV
100 fb^{-1}	Loose	Number of Events	329	138
		χ^2/dof	2.97/3	7.81/4
		Probability	0.10	0.40
		Fitted M_Z $[GeV]$	99.80±4.10	89.22±25.69
100 fb^{-1}	Tight	Number of Events	290	117
		χ^2/dof	11.67/4	1.46/3
		Probability	0.02	0.69
		Fitted M_Z $[GeV]$	98.24±5.01	99.20±25.20
300 fb^{-1}	Loose	Number of Events	936	435
		χ^2/dof	2.17/4	4.42/3
		Probability	0.70	0.22
		Fitted M_Z $[GeV]$	94.31±2.27	86.32±16.29
300 fb^{-1}	Tight	Number of Events	857	351
		χ^2/dof	3.44/4	3.71/3
		Probability	0.49	0.29
		Fitted M_Z $[GeV]$	92.76±2.36	85.79±19.07

Table 5.1: The result of the fits to the differential cross sections.

ranges.

The systematic errors, describe in Sec. 5.3, associated with the Z mass fit results in the range of 180-245 GeV are listed in Table 5.2 including the statistical ones. The systematical errors for the 245-300 GeV samples are meaningless due to the relatively large loss of events. As seen from Table 5.2 the systematic errors associated with the fitted M_Z value dominate over the statistical ones indicating that a moderate increase in luminosity will not essentially improve the overall error value.

With in the MC used in this work, one finds in general that the fit results seen to be in a good agreement with the predicted helicity differential cross section distributions. Although the fitted Z masses are seen to deviate signif-

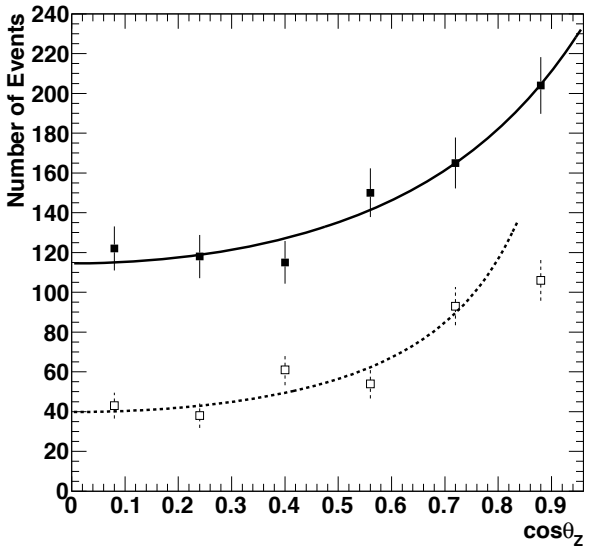

Figure 5.5: The differential cross sections for the loose invariant mass cut as a function of $cos\theta_Z$ for an integrated luminosity of 300 fb^{-1}. The solid and dashed lines represent respectively the 180-245 GeV and the 245-300 GeV energy ranges.

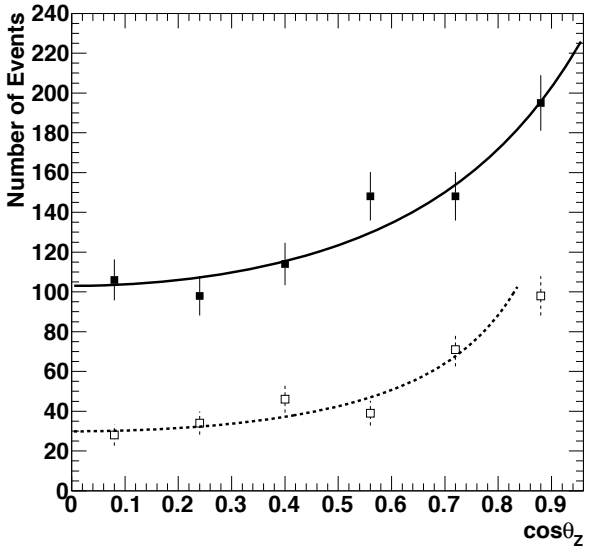

Figure 5.6: The differential cross sections for the tight invariant mass cut as a function of $cos\theta_Z$ for an integrated luminosity of 300 fb^{-1}. The solid and dashed lines represent respectively the 180-245 GeV and the 245-300 GeV energy ranges.

$\mathcal{L}$uminosity	Invariant mass cut	Fitted M_Z $[GeV]$
100 fb^{-1}	Loose	99.80±4.10±15.5
100 fb^{-1}	Tight	98.24±5.01±10.6
300 fb^{-1}	Loose	94.31±2.27±2.87
300 fb^{-1}	Tight	92.76±2.36±2.23

Table 5.2: The fitted M_Z values for the 180-245 GeV energy range of the differential cross sections with the statistical (first) and systematic (second) errors.

icantly from its SM value they are nevertheless still within errors. Since the loose mass cut clearly increases the accepted number of events its statistical error is smaller than that of the tight mass cut. However the tight cut is expected to enhance the quality of the M_Z determination and in fact its fitted mass values are closer to the official value of 91.18 GeV [49]. As will be shown further on the sensitivity of the fitted Z mass value to new physics is much more pronounced in the total cross section measurements.

5.2.2 The total cross section $\sigma(pp \to ZZ)$ at 14 TeV

The total $q\bar{q} \to ZZ$ cross section is determinate by the differential $q\bar{q} \to ZZ$ cross section through the integration over $cos\theta_Z$ to be

$$\sigma_{tot}(q\bar{q} \to ZZ) = N \int \frac{d\sigma}{dcos\theta_Z} dcos\theta_Z \ , \tag{5.5}$$

where N is a normalization factor. In our helicity calculation of the expected total cross section we have integrated $cos\theta_Z$ between 0 and 0.98, to avoid both the pole at $\theta_Z = 0$ and the loss of events in the forward direction.

The MC measured total cross section is given by a summation over all ZZ events as a function of $\sqrt{\hat{s}_{ZZ}}$ which is identical to Ecm. This summation includes both the Ecm dependence of the $q\bar{q} \to ZZ$ cross section and its occurrence (EDF) in pp collisions at 14 TeV. An example of it is shown by the histogram in Fig. 5.7.

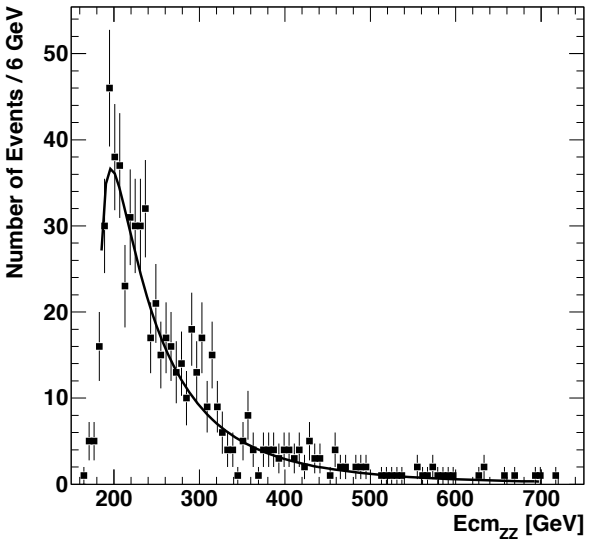

Figure 5.7: The total cross section distribution for the loose invariant mass cut as a function of energy for an integrated luminosity value of 100 fb^{-1}. The solid line represents the outcome fit function.

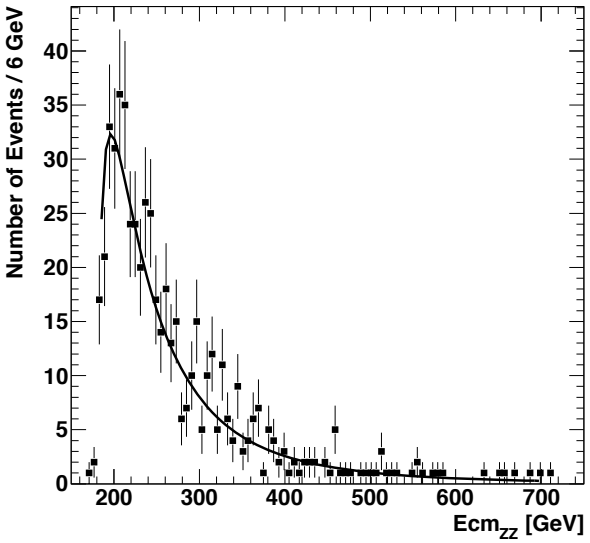

Figure 5.8: The total cross section distribution for the tight invariant mass cut as a function of energy for an integrated luminosity value of 100 fb^{-1}. The solid line represents the fit function.

To evaluate the $pp \to ZZ$ total cross section we have used our calculated $\sigma_{tot}(q\bar{q} \to ZZ)$ multiplied by the EDF shape both of which are functions of $\sqrt{\hat{s}_{ZZ}}$ and the mass of the Z boson. The M_Z value can be extracted by fitting this function to the measured total cross section distributions.

$\mathcal{L}$uminosity	Invariant mass cut		
100 fb^{-1}	Loose	Number of Events	614
		χ^2/dof	67.23/68
		Probability	0.50
		Fitted M_Z $[GeV]$	90.99±0.27±1.84
100 fb^{-1}	Tight	Number of Events	558
		χ^2/dof	51.67/67
		Probability	0.92
		Fitted M_Z $[GeV]$	90.88±0.33±0.83
300 fb^{-1}	Loose	Number of Events	1842
		χ^2/dof	63/68
		Probability	0.95
		Fitted M_Z $[GeV]$	91.01±0.15±0.10
300 fb^{-1}	Tight	Number of Events	1670
		χ^2/dof	59.44/77
		Probability	0.93
		Fitted M_Z $[GeV]$	91.03±0.15±0.12

Table 5.3: The total cross sections fit results with their statistical (first) and systematic (second) errors.

The fit results and their statistical and systematical errors which are described in Sec. 5.3 are summarized in Table 5.3 and presented in Figs. 5.7-5.10. The loose and tight invariant mass cuts are shown respectively in Figs. 5.7 and 5.8 for integrated luminosity of 100 fb^{-1} while Figs. 5.9 and 5.10 shows the loose and tight invariant mass cuts respectively for an integrated luminosity of 300 fb^{-1}. The lines in the figures represent the outcome of the fits.

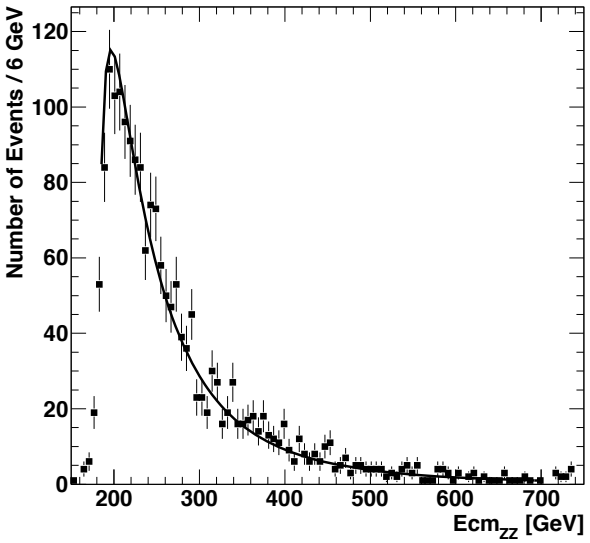

Figure 5.9: The total cross section distribution for the loose invariant mass cut as a function of energy for an integrated luminosity value of 300 fb^{-1}. The solid line represents the outcome fit function.

As seen from both Table 5.3 and the fitted plots there is a very good agreement between the MC data and the expected helicity total cross sections. This is also reflected by the fit quantities where M_Z is found to be essentially equal to its SM value. To note is that as before the fitted mass values are nearer to the official value of 91.18 GeV [49] for the tight mass cut samples as compared to the loose ones while their statistical error are smaller in the case of the loose mass cut as the accepted number of events increases.

As for the possibility to search for 'Beyond the SM' effects where in pp one is not restricted to a given Ecm (unlike in the case of e^+e^-) one observes from Table 5.3 that at 300 fb^{-1} the systematic errors are smaller than the statistical ones. This may give the opportunity to probe for new physics with the Super LHC which should increase the luminosity by a factor of 10 compare to the LHC.

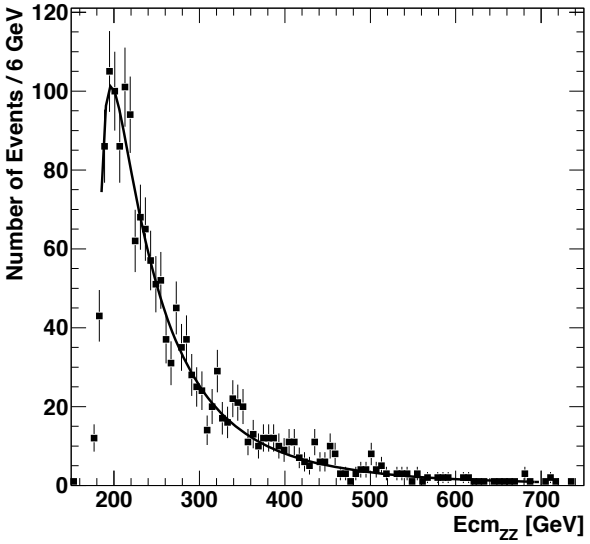

Figure 5.10: The total cross section distribution for the tight invariant mass cut as a function of energy for an integrated luminosity value of 300 fb^{-1}. The solid line represents the fit function.

5.2.3 The correlation of the ZZ decay planes

The reaction $q\bar{q} \rightarrow ZZ$, which finally decays into four charged ($e^{\pm}, \mu^{\pm}$) leptons, offers another measurable variable namely, the distributions of the angle χ between the two decay planes as illustrated in Fig. 5.11. These planes are obtained by first transforming the whole event configuration to the ZZ center-of-mass system and then transforming each lepton decay pair into the CM of its parent gauge boson. The angular distribution $F(\chi)$ has the form [76, 77]:

$$F(\chi) = 1 + Acos(2\chi) \ . \tag{5.6}$$

This correlation which can be applied to the study of the Higgs boson in its decay to a pair of Z bosons [78], is here studies in their direct production (see Fig. 3.8). For $e^+e^- \rightarrow W^+W^-$ the value of $A(ww)$ was found in LEP to be $0.012 \pm 0.021 \pm 0.012$ at $\sqrt{s_{e^+e^-}} \cong 200\ GeV$ [77] consistent with the SM. However the value of $A(zz)$ which we evaluated by the helicity amplitude method using Ref. [76] to be $\sim$0.02 has not been so far measured with data. Therefore it is of some interest to explore by the MC samples the possibility to measure it with the data coming from the LHC.

To extract the angle χ between the planes from a reconstructed $ZZ \rightarrow \mu^+\mu^-\mu^+\mu^-$ event, one assigns the muons to their corresponding Z bosons and transform them to the ZZ center-of-mass system, where the two decay planes are defined. Next one calculates the perpendicular vector to each plane defined by the assigned pair of muons. Finally the angle between planes is found from the scalar product of the two perpendicular vectors, where χ is limited to the range between 0 and $\pi/2$.

The MC χ distributions are plotted in Figs. 5.12 and 5.13 for the two chosen luminosity values and mass cuts. The above Eq. (5.6) is then fitted to the χ distributions letting $A(zz)$ to be a free parameter. The results of these fits are presented in Table 5.4 where the statistical errors alone are consists within errors with the expected value of $\sim$0.02.

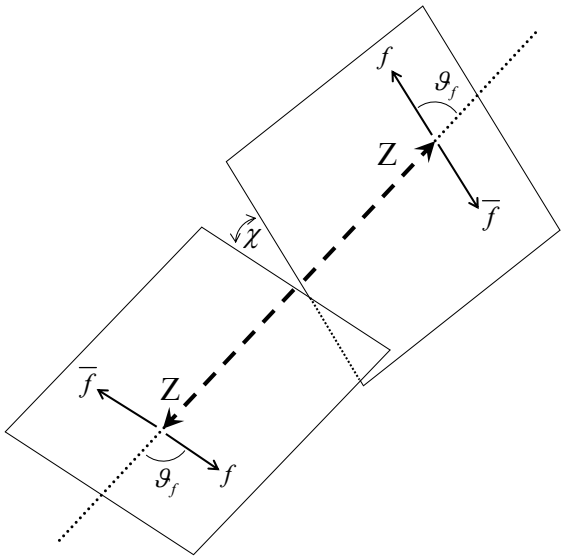

Figure 5.11: The angle χ definded by the two $f\bar{f}$ decay planes, each of them defined in the CM of their corresponding Z boson parent.

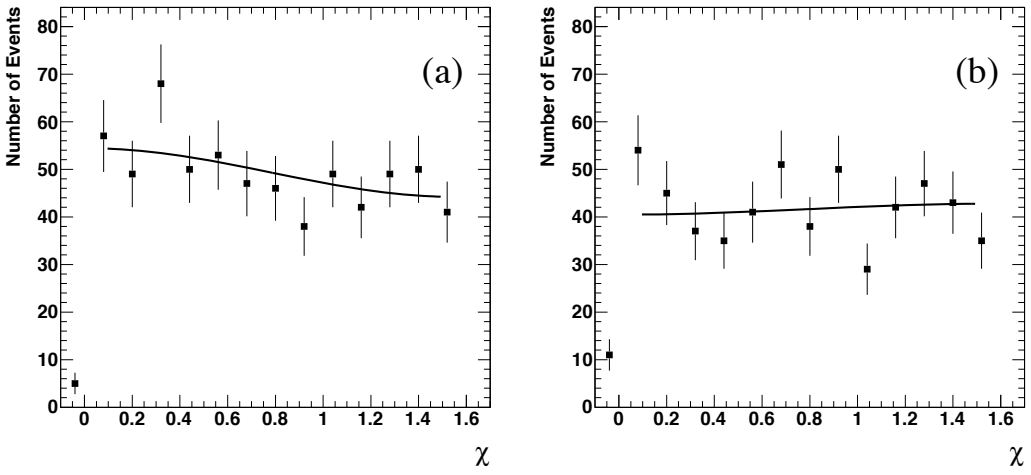

Figure 5.12: The χ plane correlation of the MC distribution for an integrated luminosity of 100 fb^{-1}. The solid lines are the fit result of Eq. (5.6) to the data. (a) For the loose mass cut sample. (b) For the tight mass cut sample.

5.3 Sources of systematic errors

Throughout our analysis we have considered several sources of systematic uncertainty like momentum resolution, reconstruction algorithms luminosity un-

$\mathcal{L}$uminosity	Invariant mass cut		
100 fb^{-1}	Loose	Number of Events	614
		χ^2/dof	8.25/9
		Probability	0.51
		$A(zz)$	0.104±0.065
100 fb^{-1}	Tight	Number of Events	558
		χ^2/dof	11.68/9
		Probability	0.23
		$A(zz)$	−0.027±0.073
300 fb^{-1}	Loose	Number of Events	1842
		χ^2/dof	19.30/22
		Probability	0.63
		$A(zz)$	0.095±0.035
300 fb^{-1}	Tight	Number of Events	1670
		χ^2/dof	16.95/22
		Probability	0.76
		$A(zz)$	0.023±0.037

Table 5.4: The fit results for the plane correlation χ and their statistical errors.

certainty and theoretical cross section evaluation which are presented in the following sub sections.

5.3.1 Momentum resolution

The main uncertainty in our ZZ MC analyses are the measured muon momentum resolution. To estimate this effect on our final physics results we took the maximum value of (see Fig. 4.2)

$$\frac{\Delta p_T}{p_T} = 0.05 \ . \tag{5.7}$$

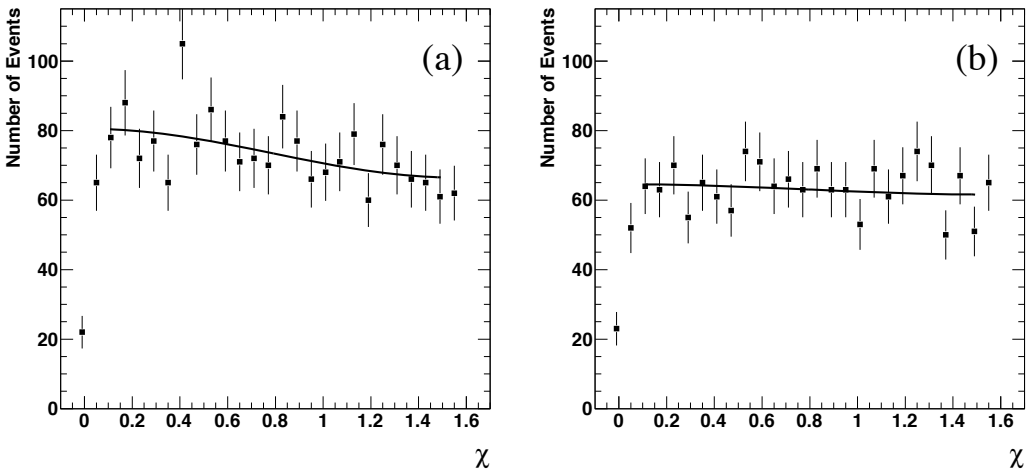

Figure 5.13: The χ plane correlation of the MC distribution for an integrated luminosity of 300 fb^{-1}. The solid lines are the fit result of Eq. (5.6) to the data. (a) For the loose mass cut sample. (b) For the tight mass cut sample.

Inasmuch that the conservative error on the momentum is not smaller than the error of p_z and further taking that the relative errors of p_x, p_y and p_z are nearly equal one has

$$\frac{\Delta p_x}{p_x} = \frac{\Delta p_y}{p_y} = \frac{\Delta p_z}{p_z} = 5\% \frac{0.5 p_T^2}{\sqrt{p_x^4 + p_y^4}} \ . \tag{5.8}$$

Next we have taken our MC data set and smeared p_x, p_y and p_z by a Gaussian distribution to produce a some what different set of 41,150 events which was used to estimate the momentum uncertainty of our final results.

5.3.2 Reconstruction algorithms

The ATLAS software framework, Athena, includes several muon reconstruction algorithms which are collected into muon reconstruction packages (see Sec. 4.1). The difference between them was used to estimate their uncertainty effects on our physics results.

5.3.3 Luminosity uncertainty

The luminosity relevant for the experiment is measured by the detector itself. The most current estimated luminosity uncertainty, as obtain from the com-

bined data measurements, is about 11% [79, 80]. This value is expected to be improved with time and is planned to reach the level few percent. To take into account this uncertainty we repeated the analyses with the assumption of a relative luminosity error of $\pm 10\%$, which effects the number of events and hence the statistical uncertainties.

5.3.4 Theoretical cross section evaluation

The theoretical calculated pp total cross sections at 14 TeV leading to a pair of ZZ gauge bosons, $\sigma_{tot}(pp \rightarrow ZZ)$ are listed in Table 3.3 at Sec. 3.2.2. As can be observed from the table, currently a non-negligible uncertainty exists in the theoretical estimates of this cross section. The bolded 12.7 pb cross section given in the table was the one used in our ZZ analyses. To estimate the effect of the theoretical calculation uncertainty on our physics results we have repeated the analyses with the other theoretical cross section values shown in the table.

5.4 The Z polarization

The angular distribution of the Z boson production and decay angles allows a spin state analysis (see Fig.3.9). This distribution depends on the production mechanism, the Z energy, and the polar production angle, $cos\theta_Z$. There are at least two leading methods, which are described in Ref. [81], that can be used to extract the polarization from the $cos\theta_f$ distributions, where θ_f is the polar decay angle defined in the rest frame of the parent gauge boson. The first is by fitting an expression given in terms of the helicity states to the $d\sigma/dcos\theta_f$ distribution and the second one is by applying the Λ_{ij} helicity projection operators.

5.4.1 The spin density matrix analysis

The spin density matrix (SDM) for a gauge boson is an hermitian matrix, ρ_{ij}, with a unit trace that can be fully described by eight free parameters. The elements lying on its diagonal ρ_-, ρ_0 and ρ_+ are the probabilities of observing a Z boson in each of the three possible helicity states -1, 0 and $+1$ which are real and positive after integration over the azimuthal angle. The general expected θ_f decay polar angular distribution for massless fermions in the rest frame of their parent gauge boson, is given in terms of the diagonal elements of the SDM by:

$$\frac{d\sigma}{dcos\theta_f} = \big[\rho_- g_-(cos\theta_f) + \rho_0 g_0(cos\theta_f) + \rho_+ g_+(cos\theta_f)\big]\sigma \qquad (5.9)$$

where g_-, g_0 and g_+ are functions of $cos\theta_f$ corresponding to the three SDM elements $\rho_-(\equiv \rho_{-1-1})$, $\rho_0(\equiv \rho_{00})$ and $\rho_+(\equiv \rho_{+1+1})$ respectively. Specifically for the decay of the Z boson, the polar angular expressions of the decay products in the range $-1 < cos\theta_Z < +1$ are given by [82]:

$$\begin{aligned} g_-(cos\theta_f) &= D^Z(1+cos\theta_f)^2 - 2Rcos\theta_f \\ g_+(cos\theta_f) &= D^Z(1-cos\theta_f)^2 + 2Rcos\theta_f \\ g_0(cos\theta_f) &= D^Z 2sin^2\theta_f \ , \end{aligned} \qquad (5.10)$$

where D^Z is a common constant for the three states and R=$(g_R^2-g_L^2)/(g_R^2+g_L^2)$ where the right (g_R) and left (g_L) couplings are equal respectively to $-1/2+sin^2\theta_w$

and $sin^2\theta_w$ (see Table 3.2). From Eqs. (5.9) and (5.10) the differential angular distribution of the charged leptonic Z boson decay is equal to

$$\frac{1}{\sigma}\frac{d\sigma}{dcos\theta_f} = \rho_-\frac{3}{8}\left[(1+cos\theta_f)^2 - 2Rcos\theta_f\right] + \rho_0\frac{3}{4}sin^2\theta_f + \rho_+\frac{3}{8}\left[(1-cos\theta_f)^2 + 2Rcos\theta_f\right] \ . \tag{5.11}$$

One should note that by adding the transverse polarizations ρ_- and ρ_+, defined as ρ_T, one eliminates the R ratio namely

$$\frac{1}{\sigma}\frac{d\sigma}{dcos\theta_f} = \rho_T\frac{3}{8}(1+cos^2\theta_f) + \rho_L\frac{3}{4}sin^2\theta_f \tag{5.12}$$

where $\rho_L = \rho_o$. From unitary condition one has further the relation $\rho_T = 1-\rho_L$.

In the cases where the number of available events is low it was found to be useful to apply an alternative method [83,84] for the SDM analysis namely the Λ_{ij} helicity projection operators. This method was previously applied to the production of W^+W^- pairs produced in e^+e^- collisions [85,86]. Here we have extended Λ_{ij} definition to the case of the Z pair production to obtain the functions:

$$\begin{aligned} \Lambda_- &= \frac{1}{2}(5cos^2\theta_f + \frac{2}{R}cos\theta_f - 1) \\ \Lambda_{\,0} &= 2 - 5cos^2\theta_f \\ \Lambda_+ &= \frac{1}{2}(5cos^2\theta_f - \frac{2}{R}cos\theta_f - 1) \ , \end{aligned} \tag{5.13}$$

where their sum is $\Lambda_- + \Lambda_0 + \Lambda_+$=1. With these operators the SDM elements are given by

$$\rho_i(cos\theta_Z) = \frac{1}{N}\sum_{k=1}^{N}\left[\Lambda_i(cos\theta_f)\right]_k \quad , \quad i \ = \ -, \ 0, \ + \tag{5.14}$$

where N is the total number of decay events. The advantage of this method is that it avoids the necessity to fit the data in a finite number of bins. For the investigation of the transverse and longitudinal polarization one has

$$\begin{aligned} \Lambda_T &= \Lambda_- + \Lambda_+ = 5cos^2\theta_f - 1 \\ \Lambda_L &= \Lambda_0 = 2 - 5cos^2\theta_f \end{aligned} \tag{5.15}$$

where the R ratio is again eliminated.

5.4.2 The longitudinal polarization evaluation

We determine the longitudinal Z polarization using our MC data sets and have further compared it to the calculated helicity amplitude polarization value. These investigations were carried out in the two SDM analyses methods.

In the first method the angular decay distributions $cos\theta_f$ are summed up over the energies between 200-500 GeV and are shown in Figs. 5.14-5.17. The loose and tight invariant mass cuts are given respectively in Figs. 5.14 and 5.15 for the integrated luminosity of 100 fb^{-1} whereas in Figs. 5.16 and 5.17 are shown the loose and tight mass cuts for the 300 fb^{-1} smaples. To obtain the

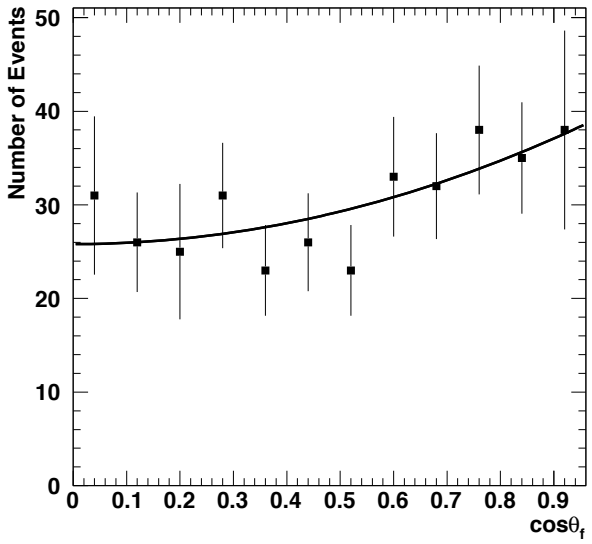

Figure 5.14: The $cos\theta_f$ angular distribution for the 100 fb^{-1} integrated luminosity and the loose invariant mass cut sample. The solid line represents the fit results of Eq. (5.12) to the data.

average longitudinal polarization we have fitted Eq. (5.12) with the unitarity condition $\rho_T = 1 - \rho_L$ to these $cos\theta_f$ distributions where ρ_0 was taken as a free parameter. The results of these fits are presented by the curves in Figs. 5.14-5.17 and listed in Table 5.5. From this table one can conclude that the integrated luminosity of 100 fb^{-1} is not sufficient enough to yield meaningful polarization results. As for the 300 fb^{-1} the longitudinal polarization results

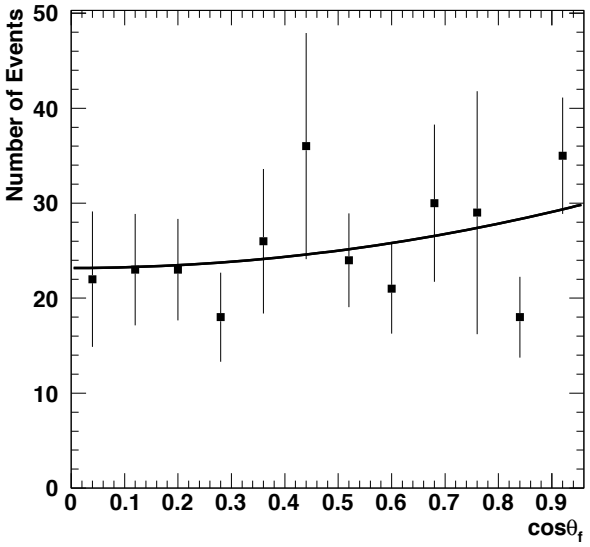

Figure 5.15: The $cos\theta_f$ angular distribution for the 100 fb^{-1} integrated luminosity and the tight invariant mass cut sample. The solid line represents the fit results of Eq. (5.12) to the data.

are very much similar for both invariant mass cuts.

It is interesting to compare these polarization results with the expected one from the helicity amplitude calculation which yielded the value of 15.58%. From the measured results given in Table 5.5 one finds that they are consistent with the calculated value. Here the reader should be reminded that the helicity calculation procedure took into account both the polarization behavior as a function of energy and its EDF but did not include any detector and other systematic effects.

It was found in our longitudinal Z polarization study that it is sensitive to the ZZ production process adopted by the MC generator program. In particular the Pythia generator used by us describes sufficiently well the single polarization but seems to ignore the presence of the joint polarization.

Next we investigated the longitudinal Z polarization in terms of the Λ_{ij} helicity projection operators. In this study we concentrated on the the 300

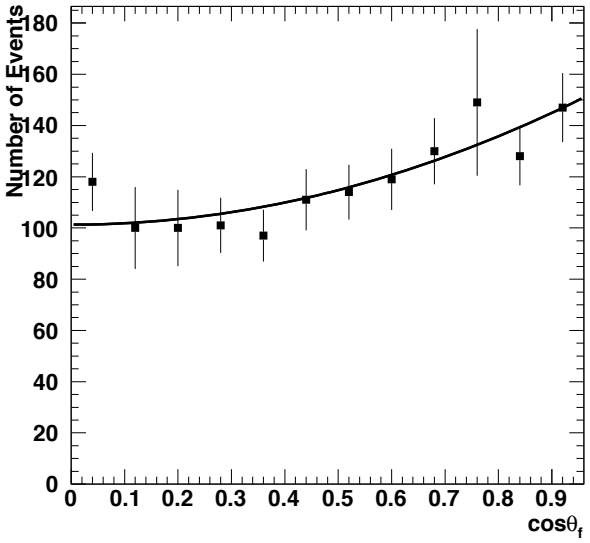

Figure 5.16: The $cos\theta_f$ angular distribution for the 300 fb^{-1} integrated luminosity and the loose invariant mass cut sample. The solid line represents the fit results of Eq. (5.12) to the data.

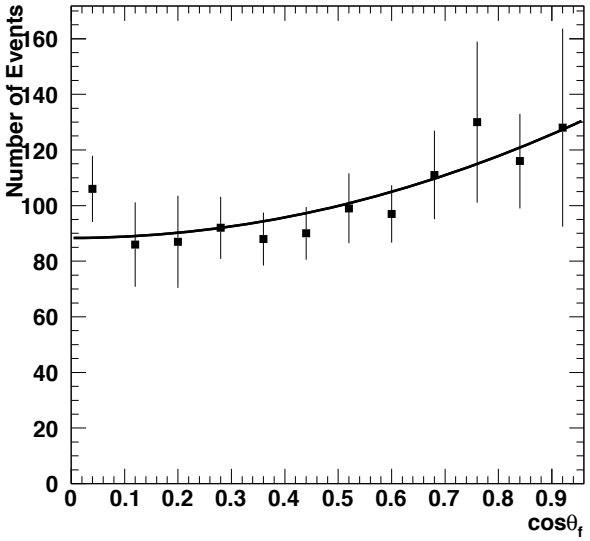

Figure 5.17: The $cos\theta_f$ angular distribution for the 300 fb^{-1} integrated luminosity and the tight invariant mass cut sample. The solid line represents the fit results of Eq. (5.12) to the data.

$\mathcal{L}$uminosity	Invariant mass cut		
100 fb^{-1}	Loose	χ^2/dof	4.42/10
		Probability	0.93
		ρ_0 [%]	13.00±8.43
100 fb^{-1}	Tight	χ^2/dof	10.53/10
		Probability	0.40
		ρ_0 [%]	20.68±9.39
300 fb^{-1}	Loose	χ^2/dof	5.10/10
		Probability	0.88
		ρ_0 [%]	13.25±4.31
300 fb^{-1}	Tight	χ^2/dof	4.27/10
		Probability	0.93
		ρ_0 [%]	13.61±4.60
Helicity amplitude expectation			15.58%

Table 5.5: The ρ_0 longitudinal Z polarization fit results for the 100 fb^{-1} and 300 fb^{-1} data samples compared to the expected helicity amplitude calculation value.

fb^{-1} integrated luminosity samples as the 100 fb^{-1} samples were found to have insufficient statistics for meaningful polarization measurements.

In Figs. 5.18 (loose cut) and 5.19 (tight cut) we plotted the ρ_0 values that were extracted by the Λ_{ij} operators as a function of Ecm. In addition the expectation from the helicity amplitude calculation is presented by the continues lines. As can be seen, in both figures the measured longitudinal Z polarization follows the general expected behavior as a function of energy. This is in particular notable in the loose mass cut event sample.

Finally we have compared the results of the two SDM ρ_0 polarization analyses. To this end we have estimated the average polarization in the range 200-500 GeV, obtain from the Λ_{ij} projection operators, which were found to be (15.1±0.4)% and (15.5±0.4)% respectively for the loose and tight invariant mass cuts. These ρ_0 values are in very good agreement with those found for

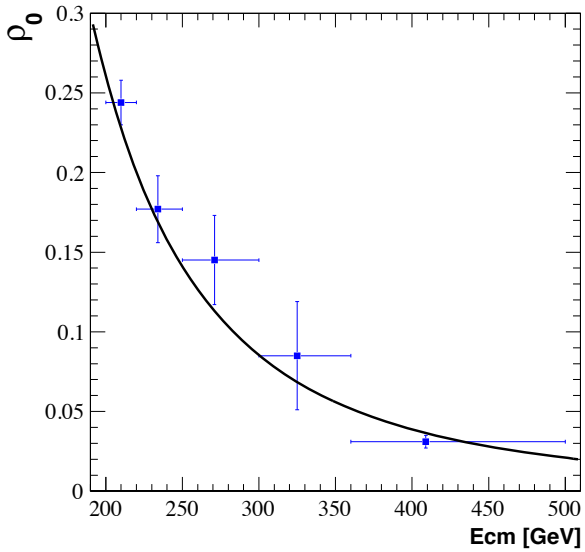

Figure 5.18: The ρ_0 longitudinal Z polarization extracted from the Λ_{ij} operators as a function of energy. The data points correspond to the 300 fb^{-1} sample subject to the loose invariant mass cut. The continues line represents the expected polarization as calculated by the helicity amplitude method.

the 300 fb^{-1} samples analyzed by the first method (see Table 5.5) and the expected 15.58% value obtained from the helicity amplitude calculation.

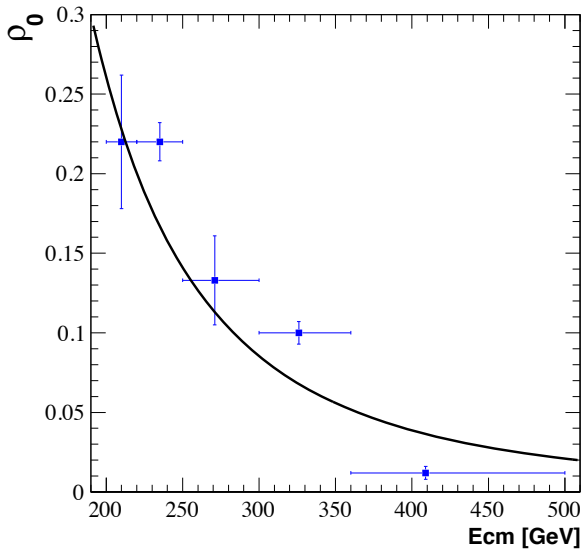

Figure 5.19: The ρ_0 longitudinal Z polarization extracted from the Λ_{ij} operators as a function of energy. The data points correspond to the 300 fb^{-1} sample subject to the tight invariant mass cut. The continues line represents the expected polarization as calculated by the helicity amplitude method.

Chapter 6

The ZZ Bose-Einstein Correlation

In 1954 the intensity interferometry was introduced by Hanbury-Brown and Twiss (HBT) [87,88] to correlate the intensity of two electromagnetic radiation arriving from extraterrestrial radio-wave sources to estimate their size. This method has been applied to the production of two identical pions in particle physics, by Goldhaber, Goldhaber, Lee and Pais (GGLP) [89] in 1959 which is generally referred to as the Bose-Einstein Correlation (BEC). This correlation has been observed in $p\bar{p}$ collision for pion pairs produced with nearby momenta and emission time. This enhancement, which was further related to the size of the particles' source in the space coordinates (see Fig. 6.1), was found to exist over a wide range of collision and boson particles energies.

6.1 BEC formalism

For the description of the main BEC expressions we have followed closely the notation presented in Ref. [90]. If the two outgoing indistinguishable bosons are represent in terms of two-particles symmetric plane wave-functions $\psi_{1,2}$ then in the incoherent case [90]

$$\psi_{1,2} = \frac{1}{\sqrt{2}} \left[e^{i(k_1 r_1 + k_2 r_2)} + e^{i(k_1 r_2 + k_2 r_1)} \right] \tag{6.1}$$

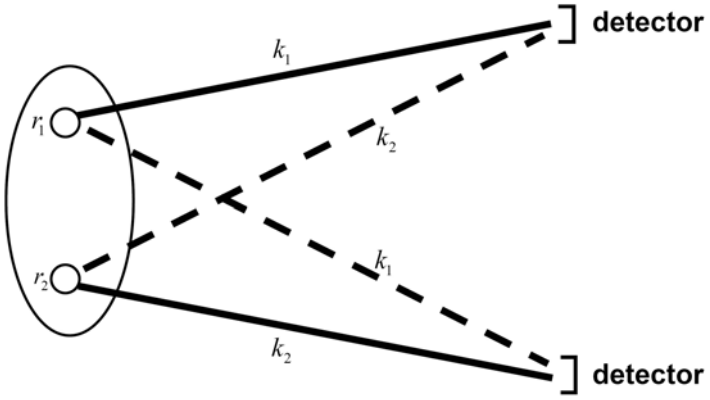

Figure 6.1: Schematic view of two identical bosons emerging from the r_1 and r_2 points within the emitter with the momentum k_1 and k_2 respectively.

where r_i and k_i are respectively the space and momentum three-vectors of the bosons. The probability associated with this wave-function is equal to

$$|\psi_{1,2}|^2 = 1 + cos\left[(k_1 - k_2)(r_1 - r_2)\right] \tag{6.2}$$

where $(k_1 - k_2)$ is the momentum difference of the particles and $(r_1 - r_2)$ is the relative emission position between them (Fig. 6.1). If the particle emission source is denoted by $\rho(r)$ then the probability to observe two particles with momenta k_1 and k_2 is given by

$$P(k_1, k_2) = \int |\psi_{1,2}|^2 \, |\rho(r_1)|^2 \, |\rho(r_2)|^2 \, d^3r_1 d^3r_2 \ . \tag{6.3}$$

The correlation function $C(k_1, k_2)$ can then be defined in terms of Eqs. (6.2) and (6.3) as

$$C(k_1, k_2) \equiv \frac{P(k_1, k_2)}{P(k_1)P(k_2)} = 1 + \frac{\int cos\left[(k_1 - k_2)(r_1 - r_2)\right] d^3r_1 d^3r_2}{P(k_1)P(k_2)} \ , \tag{6.4}$$

where $P(k_i)$ is the single probability to observe a particle with a momentum k_i. This expression, after integration over all possible pairs (Fourier transformation), could be simplified to

$$C(k_1, k_2) = 1 + |\rho(k_1 - k_2)|^2 \ . \tag{6.5}$$

In the one-dimension BEC analysis the Lorentz invariant parameter Q, introduced by Goldhaber *et al.* [89], is often used and is defined by

$$Q^2 = -(q_1 - q_2)^2 = M_{bb}^2 - 4m_b^2 \tag{6.6}$$

where q_1 and q_2 are respectively the four-momentum vectors of the two bosons of mass m_b and M_{bb}^2 is their invariant mass squared. With these definitions one can write the correlation function in terms of the variable Q as

$$C(Q) = 1 + |\rho(Q)|^2 \ . \tag{6.7}$$

If one assumes that the source is described by a spherically symmetric Gaussian density function like

$$\rho(r) = \rho(0)e^{-r^2/2r_0^2} \ , \tag{6.8}$$

then the correlation function $C(Q)$ can be expressed in term of the dimension r_G to take the GGLP form

$$C(Q) = 1 + \lambda e^{-r_G^2 Q^2} \tag{6.9}$$

where λ is the correlation strength that varies between 0 and 1 and is often refereed to as the chaoticity or the non-coherent parameter [90]. Throughout our work we confined ourself to the BEC analysis of one-dimension (1D) and use the Q parameter and its corresponding r_G dimension which we also refereed to as R_{1D}. Two typical examples of the $C(Q)$ behavior of identical charged pion pairs and their fitted Eq. (6.9) to them are shown in Fig. 6.2. The first presents an OPAL [91] BEC analysis of Z decays into pion pairs. The second example is taken from the ZEUS [92] BEC pion pairs study, where the K_S^0 and the ρ^0 regions were omitted from the fit.

Parallel to the studies done with particle reactions the BEC analysis method has also been applied to heavy-ion collisions [94]. In Fig. 6.3, which was taken from Ref. [95], we show results of the spatial dimension, R_{rms}, that were extracted from BEC studies of identical charged pions produced in nucleus-nucleus collision as a function of $A^{1/3}$, where A is the atomic number of the projectile nucleus. As can be seen from the figure, the R_{rms} increases essentially with $A^{1/3}$ namely, $R_{rms} \simeq 1.2 \times A^{1/3}\ fm$, shown by the straight line.

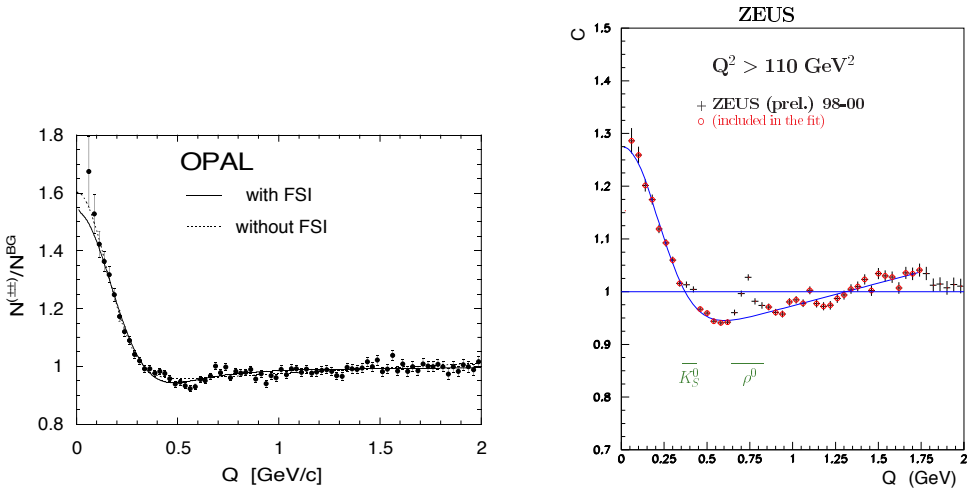

Figure 6.2: The charged pion pairs BEC as a function of Q. Left: OPAL results [91] obtained in the hadronic Z decays. The solid and dashed lines represent the fit results given in Ref. [93] respectively with and without the inclusion of final state interactions. Right: ZEUS results for momentum transfer of $Q^2 > 110$ GeV^2 [92]. The regions of K^0_S and ρ^0 which were omitted from the fit of the correlation function $C(Q)$ are indicated.

Here one should note that the BEC dimensions shown in Fig. 6.3 are essentially identical to the geometrical radius of the nuclei extracted from other kinds of measurements.

At the LEP collider BEC interferometry was applied with high statistics to pairs of pions and kaons. In order to investigate the dependence of R_{1D} on the boson mass the BEC analysis has been extended to fermions in a novel work by utilizing the Fermi-Dirac statistics property to final state pairs of $\Lambda\Lambda$ and $\bar{\Lambda}\bar{\Lambda}$ [96] and later extended to pairs of protons (for further details see [90, 96]). A compilation of the measured R_{1D} values, obtained from BEC and Fermi-Dirac Correlation (FDC) studies of Z decays to identical hadron pairs at LEP are shown in Fig. 6.4a as a function of the outgoing hadron mass m. The error bars attached to the R_{1D} values are the statistical and systematic uncertainties added in quadrature. To note is the significant spread of the $R_{1D}(m_{\pi^0})$ values between two of the experiments. Such a spread occurs often in the BEC and FDC measurements which can be traced back to the different adopted pro-

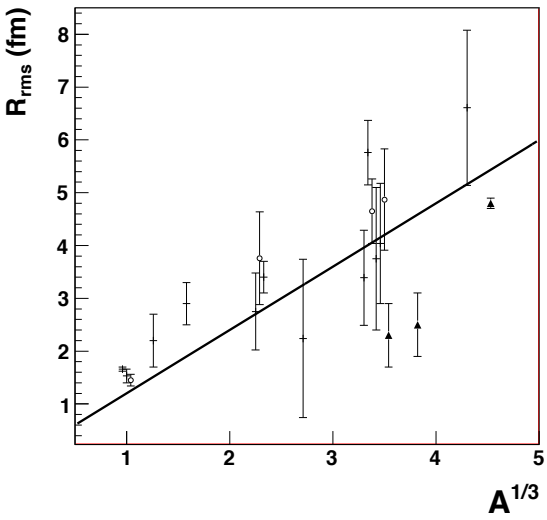

Figure 6.3: The measured R_{1D} from BEC of pion pairs produced in heavy ions collisions as a function of $A^{1/3}$ taken from reference [95]. The straight line represents the function $R = aA^{1/3}\ fm$ with $a = 1.2\ fm$.

cedures and choices of the reference sample. Notwithstanding this deficiency, R_{1D} is seen to decrease with the increase of the particle mass. That this behavior of $R_{1D}(m)$ is not only limited to the Z hadronic decays is demonstrated in Fig. 6.4b. This figure shows the R_{1D} results obtained from BEC and FDC analyses of the outgoing hadrons, from pion to deuteron pairs, produced in the central $Pb + Pb$ collisions at 158/A GeV [97].

In Ref. [103] it has been shown that from the Heisenberg uncertainty relations one can derive a connection between R_{1D} and a non-zero particle mass m, namely

$$R_{1D}(m) \ = \ \frac{c\sqrt{\hbar\Delta t}}{\sqrt{m}} \ . \tag{6.10}$$

This time scale Δt has been taken in [103] to be equal to 10^{-24} seconds representing the outgoing strong interacting hadron pairs. As a result, the R_{1D} behavior on the hadron mass shown in Fig. 6.4a was fairly well reproduced by Eq. (6.10) which is represented by the continuous line in the figure. In our recent work [104] we have pointed out that all the data given in the figure are the decay product of the Z gauge boson, the lifetime of which is of

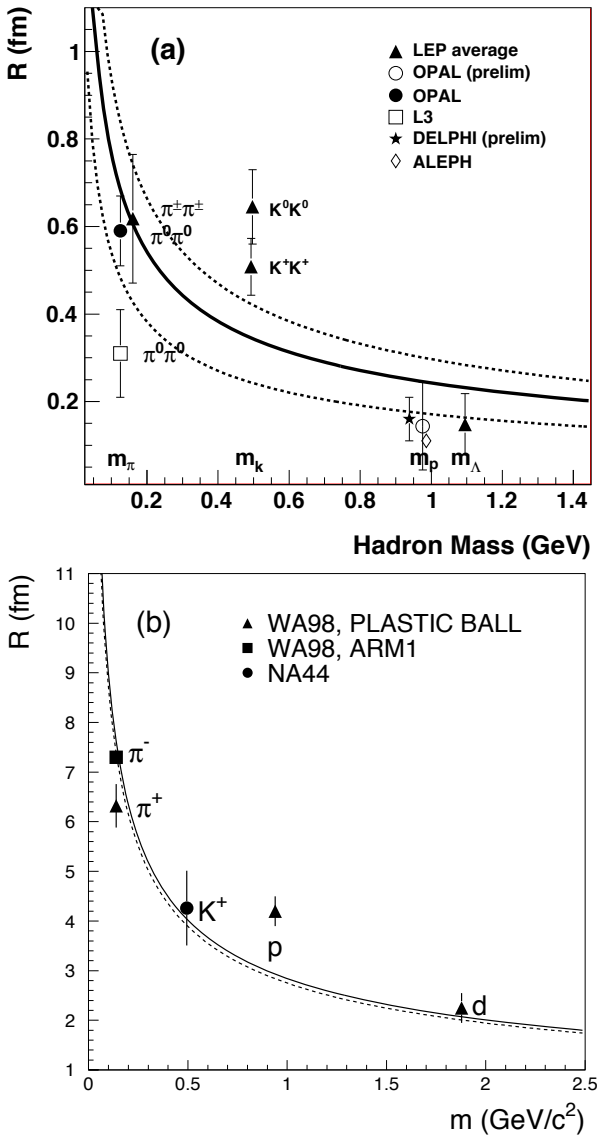

Figure 6.4: R_{1D} as a function of the hadron mass obtained from BEC and FDC analyses. (a) Values obtained from the Z hadronic decays by the LEP experiments [98–102]. The solid line represent Eq. (6.10) with Δt=10^{-24} seconds while the dotted lines are for Δt=$(1 \pm 0.5) \times 10^{-24}$ seconds. (b) BEC analyses of hadron pairs emerging from central $Pb + Pb$ collisions at 158/A GeV taken from [97]. The continuous line is the result of a fit of Eq. (6.10) to the data of the Plastic Ball detector whereas the dotted line is the result of the fit to all the data points shown in the figure.

the order of 10^{-24} seconds. Thus the success of the choice of Δt=10^{-24} seconds, may in fact be, as we further argue, due to the decay particles' emission time which is prescribed by the Z boson lifetime. In the Z decay, as well as in hadron interactions, like in pp reactions, the particle's collision and emission times are practically of the same order of magnitude. This apparently is not the case in heavy ion collisions. In the $Pb+Pb$ collisions at 158/A GeV, measured by the WA98 collaboration [97], the R_{1D} values obtained from identical hadron pairs are seen in Fig. 6.4b to be described very well, apart from the slight departure of $R_{1D}(m_p)$, by the continuous line. This line is the result of a fit of Eq. (6.10) to the data yielding $\Delta t = (1.28 \pm 0.03) \times 10^{-22}$ seconds that is much longer than the particles' collision time of $\sim 10^{-24}$ seconds. Here it is important to note that the success of this fit was taken by the WA98 collaboration as an indication for a common emission duration of the various particle pairs produced in the $Pb+Pb$ reactions.

6.2 The interpretation of the Δt time scale

The $R_{1D}(m_\pi)$ values obtained from BEC analyses of pion pairs emerging from collisions like the electron-nucleon [105] and neutrino-nucleon [106] are very similar to those obtained in e^+e^- and pp collisions and thus exclude the possibility that Δt is related to the interaction strength of the incoming particles. As for the association of Δt with the interaction strength of the outgoing identical correlated particles, it is instructive to examine Fig. 6.5. In this figure, taken from Ref. [104], the expectation of $R_{1D}(m)$ are plotted against m for three Δt values of 10^{-24}, 10^{-19} and 10^{-12} seconds which represent the strong, electro-magnetic and weak interactions. As can be seen, if indeed Δt is representing the interaction strength of the outgoing particles then for weak interaction the R_{1D} measured by BEC or FDC should reach unreasonable high values as compared to those measured in Z^0 hadronic decays.

An additional evidence against the association of Δt with the interaction strength of the outgoing particles is coming from the BEC measurement of the non-zero transverse momentum photon pairs, directly produced in the central

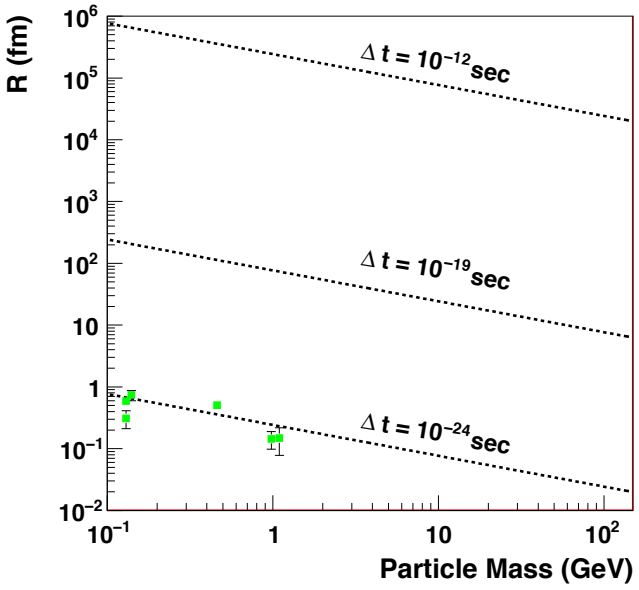

Figure 6.5: The expected R_{1D} dependence on the particle mass for three Δt values of 10^{-24}, 10^{-19} and 10^{-12} seconds, representing respectively strong, electro-magnetic and weak interactions of the outgoing particles. The data in the figure are the LEP measured R_{1D} values from Z decays, taken from Ref. [104].

$Pb + Pb$ interactions at 158/A GeV [107]. In this case Eq. (6.10) cannot be applied since $m_\gamma = 0$. However, from the Heisenberg uncertainty relations one can also derive [108] a relation between the longitudinal dimension R_{long}, defined in the Longitudinal Center of Mass System [109], and the average transverse mass m_T, namely

$$R_{long}(m_T) \;=\; \frac{c\sqrt{\hbar\Delta t}}{\sqrt{m_T}} \;, \tag{6.11}$$

which is applicable to photons with a non-zero transverse momentum. The BEC analysis of the directly produced photon pairs of the WA98 collaboration [107] was divided into two transverse momentum p_T regions which yielded the following R_{1D} and their associated λ_{1D} chaoticity parameter values:

$$R^I_{1D} = 5.9 \pm 1.2\ fm; \quad \lambda^I_{1D} = 0.0028 \pm 0.0007; \quad \text{for } 100 < P_T < 200\ MeV/c$$

$$R^{II}_{1D} = 6.1 \pm 1.4\ fm; \quad \lambda^{II}_{1D} = 0.0029 \pm 0.0017; \quad \text{for } 200 < P_T < 300\ MeV/c\ ,$$

where the statistical and systematic errors are added in quadrature. These $R_{1D}(\gamma)$ values are consistent with the $R_{1D}(m_\pi)$ values obtained in the same $Pb+Pb$ collision experiment at 158/A GeV. From this one can safely infer that the Δt associated with the directly produced photons is in any case far away, by a few order of magnitudes, from the Δt region that represents the elecro-magnetic interaction strength (see Fig. 6.5). Following these observations we have been lead to assign Δt to be the particles' emission time.

6.3 BEC of ZZ pairs

Even though the BEC analysis of two directly produced photons in $Pb+Pb$ collisions supports the notion that Δt is the particle emission time, a decisive answer to this issue should come from BEC and/or FDC of weak interacting particles. Presently no such information exists. The $\mu^{\pm}\mu^{\pm}$ pairs are in general the decay product of pions and/or kaons so that they are not produced simultaneously. As for the $e^{\pm}e^{\pm}$ system produced in particle reactions, it also has similar drawbacks. For this reason we here examined the possibility to carry out a BEC analysis of the two weakly interacting ZZ pairs. These pairs are expected at lower order to be dominated by a coherent pp production processes. However, high order corrections may well introduced a small non-coherent contributions which will be sufficient to allow a meaningful BEC analysis as was the BEC case in the di-photon [107] final state which was successful even with a chaoticity λ value as small as ≈ 0.003. The ZZ BEC analysis will also serves to test if the R_{1D} dimension will still behaves as $1/\sqrt{m}$ at high masses around 100 GeV.

Table 6.2 summarizes the selection criteria and number of events used in our ZZ BEC analysis. This is based on a MC sample generated by the Pythia program that utilized the CTEQ 6L1 PDF package and which includes the Z boson width. To note is that our analysis utilized only the ZZ pair events that decay into $\mu^+\mu^-\mu^+\mu^-$ this sample can in principle be enlarged to include $ZZ \rightarrow 4l$ where $l = \mu/e$ to reduce the statistical uncertainty by a factor of two.

Monte Carlo generation	$pp \rightarrow ZZ \rightarrow \mu^+\mu^-\mu^+\mu^-$	Pythia 6.403, CTEQ 6L1
Number of events	$\sim 10,287$	Equivalent to luminosity of 720 fb^{-1}
Major selection cuts:	$p_T > 20\ GeV$	At least 1 muon
	Two opposite charged lepton pairs	
	Invariant mass cut (for both Z's)	$79\ GeV < M_Z < 105\ GeV$
Acceptation efficiency	$\sim 45\%$	After simulation and reconstruction

Table 6.1: Details of the $pp \rightarrow ZZ \rightarrow \mu^+\mu^-\mu^+\mu^-$ BEC study as used by us.

In Fig. 6.6 we present the expected $C(Q)$ for ZZ pairs decaying into muons for a high integrated luminosity of $\sim 720\ fb^{-1}$ taking λ to be 0.33. The fit of Eq. (6.10) to the $C(Q)$ distribution yielded the value of $R_{1D} = 0.126 \pm 0.204\ fm$ with a χ^2/dof of 5/10 which is consistent with the expected one of 0.024 fm

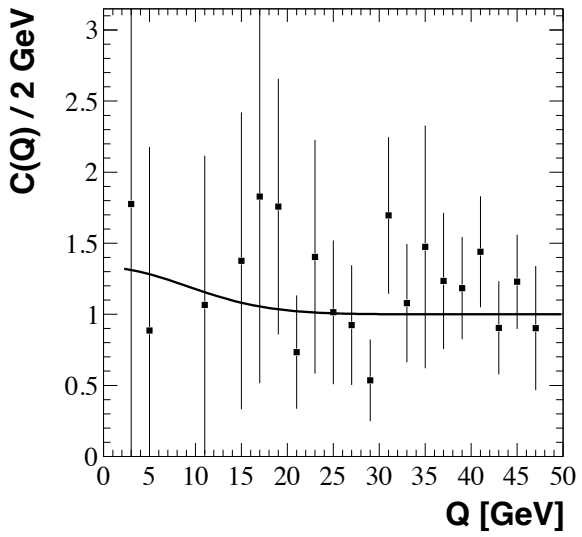

Figure 6.6: The correlation function $C(Q)$ for the final state ZZ system. The line represents Eq. (6.10) fit result of $R_{1D} = 0.126 \pm 0.204\ fm$ taken λ to be 0.33.

calculated from Eq. (6.10) using $\Delta t = 10^{-24}$ seconds. Even with this relatively high uncertainty the R_{1D} value with its error will exclude the possibility that Δt depends on the interaction strength of the outgoing correlated particles. From this study it is clear that to carry out a meaningful BEC analysis of the ZZ pairs requires a very large statistics which maybe realized at the 14 TeV CERN Large Hadron pp Collider in its upgraded luminosity configuration.

Chapter 7

Summary and Outlook

The work presented here is based on a simulation of the ATLAS detector expected performance and which covers the main physics properties of the ZZ pair production at 14 TeV. These includes the measurements of the differential and total cross sections, determination of the longitudinal Z polarization, the angular correlation between the two $Z \rightarrow l^+l^-$ decay planes and the feasibility to study the ZZ pairs Bose-Einstein correlation analysis. This research utilized the so called "gold plated events" where the Z boson pairs are observed through their decay into two pairs of muons. These topics were analyzed using an extensive MC samples equivalent to an integrated luminosity of 100 $fb^{-1}/year$, as envisaged for the LHC running. In addition, the benefit from a higher luminosity of 300 $fb^{-1}/year$ has been explored. In both luminosity studies two values for the Z invariant mass cut have been applied, a loose and a tight one. The study reported in this work has shown that while the loose cut reduced the statistical error, the tight cut improved the quality of the measurements and thus it should be recommended for future ZZ analysis.

In the differential and total cross section analyses we have set the Z boson mass value to be a free fit parameter to be able to exam our sensitivity to the SM properties and to possible "new physics" signs. The M_Z value obtained from the differential cross section analysis was 98.24±5.01±10.60 GeV which was improved by using the 300 fb^{-1} luminosity sample to yield 92.76±2.36±2.23 GeV as compared to 91.18 [49], the current known value.

From the total cross section analysis better M_Z fitted values were obtained namely, 90.88±0.33±0.83 GeV and 91.03±0.15±0.12 GeV for the luminosities of 100 and 300 fb^{-1} respectively. From the options considered in this study one can conclude that the best condition to search for "Beyond the SM" effects is a tight invariant mass cut and evidently the higher luminosity values of 300 fb^{-1}.

Throughout this work we have used the PDF parameters values extrapolated from the Tevatron and the HERA findings. An improvement of these parameters should be achieved as more data from the LHC will be available. In the experimental study of $pp \to ZZ$ reaction we have encountered the known problem that the theoretical calculations are given in terms of the basic process $q\bar{q} \to ZZ$. The transformation from pp collisions to $q\bar{q}$ reactions and vice versa have here been worked out to yield the so called Energy Density Functions. A successful verification of this transformation has been shown by using the ZZ pair production.

The $ZZ \to \mu^+\mu^-\mu^+\mu^-$ decay planes correlation has been investigated. In these analyses the fitted correlation strength values of -0.027 ± 0.073 and 0.023 ± 0.037 were extracted for an integrated luminosity of 100 and 300 fb^{-1} respectively. These values are consistent within errors with the expected value of $\sim$0.02 which was calculated for the ZZ lower order production mechanism (see Fig 3.8) by us via the helicity amplitude method.

In the study of the longitudinal Z polarization we have applied two Spin Density Matrix analysis methods. In the first one the angular decay distribution of the Z boson was used. From this distribution the fitted longitudinal Z polarization was found to be $\rho_0 = (13.2\pm3.8)$ and (15.0 ± 4.1) % for the loose and tight invariant mass cut samples respectively. The second method investigated ρ_0 in terms of the Λ_{ij} projection operators which were previously applied to the W^+W^- analyses [85, 86] and were extended by us to the ZZ pair production. For the comparison between the two methods the projection operator polarization values were average over the same energy covered in the first method and thus yielded $\rho_0 = (15.1\pm0.4)$ and (15.5 ± 0.4) % for the loose and tight cut samples as before. We further used the helicity amplitude tech-

nique to calculate the SM expected longitudinal Z polarization which yielded 15.6 %. As seen the two methods are in a very good agreement between themselves and with the expected SM value.

The interest in a Bose-Einstein Correlation study of ZZ pairs produced in pp collisions has been illustrated for two main reasons. The first is the fact that it will be the first BEC analysis of non-hadronic produced particles. The second reason is the fact that this BEC measurement of two very heavy bosons which so far has been only applied up to the mass of the deuteron. The feasibility of such a study has been investigated and it was found that it can only be realized in the future Super LHC with a typical integrated luminosity of about 1000 fb^{-1} per year.

Following the LHC operation and its achivments the high energy community is considering the design and construction of a high energy Linear e^+e^- Collider (LC) [110–112]. Its final design, however, does depends on the discovery of "Beyond the SM" phenomena in the LHC such as super symmetric particles. Currently two variations of a LC are discussed namely the International Linear Colliser and the Compact Linear Collider. The advantage of an e^+e^- LC is mainly due to two reasons: The first is the realization that the CM of the reactions is identical to that of the colliding beams. The second is the general simplicity of the e^+e^- reactions as compare to those in pp collisions. It is generally accepted that at least the LC electron beam should be longitudinal polarized as was the case in the SLAC Linear Collider where it was achieved by irradiating GaAs crystals [113]. There are several arguments that require in addition also a longitudinal polarized positron beam [114]. Within this program one attractive proposition to create a polarized position beam via an undulator magnetic system [115] has been sucessfuly tested by the E-166 collaboration experiment at SLAC [116–118].

Appendix A

Observation of Polarized Positrons from an Undulator-Based Source

G. Alexander,[1] J. Barley,[2] Y. Batygin,[3] S. Berridge,[4] V. Bharadwaj,[3] G. Bower,[3] W. Bugg,[4] F.-J. Decker,[3] R. Dollan,[5] Y. Efremenko,[4] V. Gharibyan,[6,7] C. Hast,[3] R. Iverson,[3] H. Kolanoski,[5] J. Kovermann,[8] K. Laihem,[9] T. Lohse,[5] K. T. McDonald,[10] A. A. Mikhailichenko,[2] G. A. Moortgat-Pick,[11] P. Pahl,[6] R. Pitthan,[3] R. Pöschl,[6] E. Reinherz-Aronis,[1] S. Riemann,[9] A. Schälicke,[9] K. P. Schüler,[6] T. Schweizer,[5] D. Scott,[12] J. C. Sheppard,[3] A. Stahl,[8] Z. M. Szalata,[3] D. Walz,[3] and A. W. Weidemann[3]

[1]*Tel-Aviv University, Tel Aviv 69978, Israel*
[2]*Cornell University, Ithaca, New York 14853, USA*
[3]*SLAC, Menlo Park, California 94025, USA*
[4]*University of Tennessee, Knoxville, Tennessee 37996, USA*
[5]*Institut für Physik, Humboldt-Universität zu Berlin, D-12489 Berlin, Germany*
[6]*DESY, D-22607 Hamburg, Germany*
[7]*YerPhI, Yerevan 375036, Armenia*
[8]*RWTH Aachen, D-52056 Aachen, Germany*
[9]*DESY, D-15738 Zeuthen, Germany*
[10]*Joseph Henry Laboratories, Princeton University, Princeton, New Jersey 08544, USA*
[11]*University of Durham, Durham, DH1 3LE, United Kingdom*
[12]*STFC Daresbury Laboratory, Daresbury, Warrington, Cheshire, WA4 4AD, United Kingdom*

(Received 8 March 2008; published 29 May 2008)

An experiment (E166) at the Stanford Linear Accelerator Center has demonstrated a scheme in which a multi-GeV electron beam passed through a helical undulator to generate multi-MeV, circularly polarized photons which were then converted in a thin target to produce positrons (and electrons) with longitudinal polarization above 80% at 6 MeV. The results are in agreement with GEANT4 simulations that include the dominant polarization-dependent interactions of electrons, positrons, and photons in matter.

DOI: 10.1103/PhysRevLett.100.210801 PACS numbers: 07.77.Ka, 13.88.+e, 29.27.Hj, 41.75.Fr

A polarized positron beam would enhance the physics capability of a TeV-scale e^+e^- linear collider [1]. Polarized positrons can be produced via the pair-production process initiated by circularly polarized photons [2]. In a scheme proposed by Balakin and Mikhailichenko [3] a multi-GeV electron beam is passed through a helical undulator [4] to generate the needed multi-MeV photons with circular polarization. Alternatively, the circularly polarized photons can be produced by laser backscattering off an electron beam [5,6]. An experiment (E166) has been performed to demonstrate that the undulator-based scheme can produce polarized positron beams of sufficient quality for use at the proposed International Linear Collider (ILC) [7]. The main elements of the experiment were the Stanford Linear Accelerator Center (SLAC) linac [8], the Final Focus Test Beam (FFTB) [9], a pulsed helical undulator, and detectors to measure the photon and positron polarizations [10], as shown schematically in Fig. 1.

The experiment operated with an electron beam energy of 46.6 ± 0.1 GeV at a repetition rate of 10 Hz with $1–4 \times 10^9 e$/pulse. The normalized beam emittances were $\gamma\epsilon_x(\gamma\epsilon_y) \approx 2.2(0.5) \times 10^{-5}$ m rad, and the transverse spot size was tuned to $\sigma_x \approx \sigma_y \approx 35$ μm at the 1-m-long undulator whose aperture was only 0.9 mm. After passing through the undulator, the primary electron beam was deflected away from the photon beam by a string of permanent magnets (D1). A circularly polarized photon beam of peak energy $\approx$ 8 MeV was created in the undulator and then drifted approximately 35 m to the diagnostic detectors, shown in the lower part of Fig. 1 and in greater detail in Fig. 2.

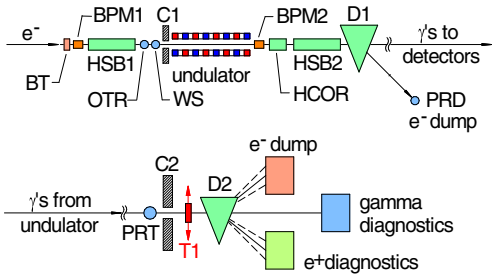

FIG. 1 (color online). Conceptual layout (not to scale) of the E166 experiment. A 46.6-GeV electron beam entered from the left and was deflected by magnet D1 after traversing the undulator. Part of the beam of $\approx$ 8-MeV circularly polarized photons created in the undulator was converted to positrons in a target 35 m downstream of the undulator, and the rate and polarization of the positrons and unconverted photons were subsequently diagnosed in the spectrometer D2. BPM = beam-position monitor, BT = beam toroid, C = collimator, HCOR = horizontal-correction magnet, HSB = hard-soft-bend magnet, OTR = optical-transition-radiation monitor, PR = beam-profile monitor, T1 = target, WS = wire scanner.

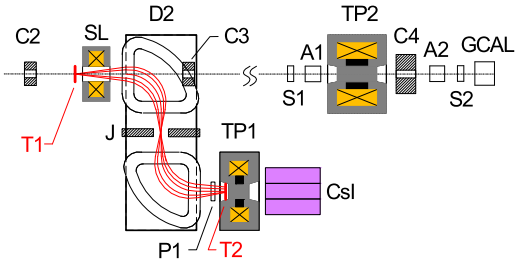

FIG. 2 (color online). Schematic of the photon and positron diagnostics. A1, A2 = aerogel Čerenkov detectors, C2 − C4 = collimators, D2 = dipole spectrometer magnet, CsI = 3 × 3 array of CsI crystals, GCAL = Si-W calorimeter, J = movable W jaws, P1, S1, S2 = Si-diode detectors, SL = solenoid lens, T1 = positron production target, T2 = reconversion target, TP1 = positron transmission polarimeter solenoid, TP2 = photon transmission polarimeter solenoid. The detectors were encased in lead and tungsten shielding (not shown).

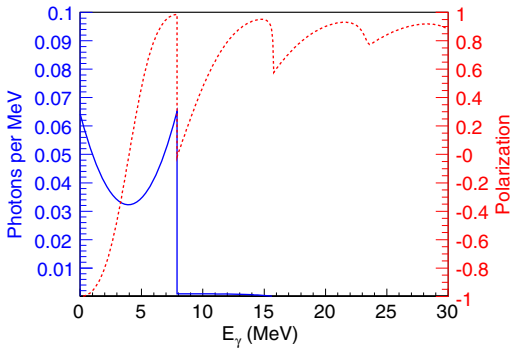

FIG. 3 (color online). Solid line: calculated photon number spectrum per beam electron of undulator radiation integrated over angle, plotted as a function of photon energy E_γ for electron beam energy 46.6 GeV, undulator period 2.54 mm and undulator strength parameter $K = 0.17$. The peak energy of the first-harmonic (dipole) radiation was 7.9 MeV. Dashed line: longitudinal polarization P_γ of the undulator radiation as a function of energy.

The photon beam impinged upon a 0.2-radiation-length tungsten target T1 to produce positrons and electrons which were separated in spectrometer D2, and the polarization and rate of the positrons were measured in transmission polarimeter TP1 [11]. The unconverted photons were monitored in a second transmission polarimeter, TP2.

The undulator had bifilar, helical windings of wires of cross section 0.6×0.6 mm^2 with currents (2.3 kA in a 12 μs pulse) flowing in opposite directions, resulting in a transverse magnetic field whose direction rotated with period 2.54 mm and whose strength was 0.71 T on axis, corresponding to an undulator strength parameter of $K = 0.17$. The calculated energy spectrum and longitudinal polarization of the photons produced by the undulator are shown in Fig. 3. For an electron beam energy of 46.6 GeV and $K = 0.17$ the first-harmonic photon energy cutoff is $E_\gamma = 7.9$ MeV, at which energy the longitudinal polarization P_γ is 0.98, differing from unity due to the small admixture of second harmonic photons.

The photon beam was monitored in a transmission polarimeter TP2, indicated in the right side of Fig. 2. The flux of photons was determined by aerogel Čerenkov counters, A2, A2, and by silicon-diode detectors, S1, S2, before and after a 15-cm-long cylinder of iron whose axial magnetization was reversed periodically. The total energy of photons that passed through the iron cylinder was monitored in a W-plate calorimeter GCAL read out by interleaved Si diodes. The photon flux at full undulator current, observed in detector S1 with the pair-production target T1 removed, was 0.071 ± 0.007 photons/beam electron, which value is only 20% of expectations, likely due to misalignment of collimator C2. When the undulator current was reduced, the photon flux showed the expected quadratic dependence on the current.

The asymmetry $\delta_\gamma = (S_\gamma^- - S_\gamma^+)/(S_\gamma^- + S_\gamma^+)$ in the observed signals $S_\gamma^\pm$ of photons transmitted through the iron cylinder was $0.0331 \pm 0.0012(\text{stat}) \pm 0.0063(\text{syst})$ using aerogel detector A2, $0.0367 \pm 0.0007(\text{stat}) \pm 0.0040(\text{syst})$ using calorimeter GCAL, and $0.0388 \pm 0.0006(\text{stat}) \pm 0.0016(\text{syst})$ using Si-diode detector S2. A simulation that combined the energy and polarization distributions shown in Fig. 3 with the spin dependence of Compton scattering of the polarized photons off polarized atomic electrons in the magnetized iron [12] calculated asymmetries of 0.036 for detector A2 (assuming a Čerenkov threshold of 3.8 MeV), 0.035 for GCAL, and 0.034 for S2.

Positrons (and electrons) produced from undulator photons in the W target T1 were focused to a parallel beam by solenoid lens SL and then energy selected and separated from the electrons and unconverted photons in spectrometer D2 consisting of a pair of dipole magnets, shown in Fig. 2. The energy spread of positrons at the reconversion target T2 was 5% (FWHM). The positron flux (typically 2–6 $\times 10^4$/pulse with undulator on and 1% of this with undulator off) was monitored at this location by Si-diode detector P1. The polarization of the positrons was determined by first reconverting them into polarized photons by a 0.5-radiation-length W disk, and then using transmission polarimeter TP1 to measure the longitudinal polarization of the photons. This polarimeter consisted of a 7.5-cm-long magnetized iron cylinder followed by a 3×3 array of CsI crystals.

Data were collected with the undulator on and off during successive electron beam pulses. The sign of the magnetization of polarimeter TP1 (and that of TP2 as well) was reversed after every 1500 undulator-on beam pulses.

Beam-off and target-out runs were interspersed throughout the data sets. Data were taken with positrons at five energies from 4.6 to 7.4 MeV, and with electrons at a single energy (6.7 MeV) for which the current in dipole spectrometer D2 (but not that in solenoid lens SL) was reversed. Data samples for each energy ranged from 2–20 $\times$ 10^5 beam pulses and a total of more than 8 $\times$ 10^6 events were recorded during the experiment.

The distribution of photon energies from reconverted positrons as observed in the central CsI crystal for central positron energy of 6.7 MeV is shown in Fig. 4 for undulator-on and undulator-off beam pulses. Approximately 30 photons from reconverted positrons were observed each pulse above a background of a similar number of MeV particles from showers of beam electrons that scraped the undulator tube.

The positron (or electron) polarization is derived from the asymmetry

$$\delta_{e^\pm} = (S^-_{\mathrm{CsI}} - S^+_{\mathrm{CsI}})/(S^-_{\mathrm{CsI}} + S^+_{\mathrm{CsI}}) \quad (1)$$

of signals $S^\pm_{\mathrm{CsI}}$ that are proportional to the (integrated) energies $E^\pm_{\mathrm{CsI}}$ of reconverted photons observed in the central CsI crystal for the two signs of axial magnetization of polarimeter TP1. The outer eight crystals of the CsI array were not used in the final analysis because of poorer signal-to-background ratio. The energy calibration of the crystals was maintained by data collected with radioactive sources embedded in the array. The photon energies $E^\pm_{\mathrm{CsI}}$ were corrected for background using the undulator-off data, and normalized to the rates observed in the Si-diode detector P1 according to

$$S_{\mathrm{CsI}} = \frac{1}{N_{\mathrm{on}} N_{\mathrm{off}}} \sum_{i=1}^{N_{\mathrm{on}}} \sum_{j=1}^{N_{\mathrm{off}}} \frac{E^{\mathrm{on}}_{\mathrm{CsI},i} - E^{\mathrm{off}}_{\mathrm{CsI},j} \frac{I^{\mathrm{on}}_i}{I^{\mathrm{off}}_j}}{\mathrm{P1}^{\mathrm{on}}_i - \mathrm{P1}^{\mathrm{off}}_j \frac{I^{\mathrm{on}}_i}{I^{\mathrm{off}}_j}}, \quad (2)$$

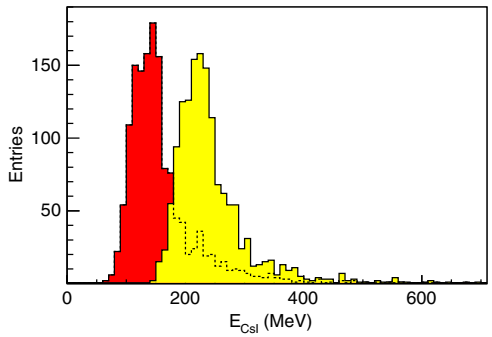

FIG. 4 (color online). Distributions of energy E_{CsI} observed in the central CsI crystal of the positron polarimeter from individual electron beam pulses with undulator-on (right peak) and undulator-off (left peak). The central positron energy was 6.7 MeV.

where $N_{\mathrm{on}} \approx N_{\mathrm{off}} \approx 1500$ are the numbers of events with undulator-on and off in data sets with $\pm$ magnetization of polarimeter TP1, I is the number of 46.6-GeV electrons as measured in beam toroid BT, and P1 is the signal observed in that Si-diode detector. Terms in Eq. (2) more than 2 standard deviations from the mean were discarded to stabilize the averaging procedure against the effect of outliers caused by occasional off-energy electron beam pulses.

The asymmetry (1) was calculated for each pair of 1500 undulator-on beam pulses with opposite magnetization of the polarimeter, as shown in Fig. 5 for data collected with a central positron energy of 6.1 MeV. Asymmetries more than 3 standard deviations from the average were discarded. The averaged asymmetries were typically 1%, as listed in Table I. Without the normalization (2) to the rates in detector P1, the asymmetries would have been about 10% smaller for positrons and 40% larger for electrons, which indicates differing effects on these particle types of their interactions with the stray fields of the solenoid lens SL, the spectrometer magnet D2, and the polarimeter magnet TP1. Alternative normalization procedures yielded results consistent with those given in Table I. Use of all nine CsI crystals in the analysis yielded similar results but with larger uncertainties due to the relatively larger backgrounds in the outer crystals.

The longitudinal polarization $P_{e^\pm}$ of the positrons (electrons) is deduced from the measured asymmetry $\delta_{e^\pm}$ using the relation

$$P_{e^\pm} = \frac{\delta_{e^\pm}}{A_{e^\pm} P^{\mathrm{Fe}}_e}, \quad (3)$$

where $P^{\mathrm{Fe}}_e = 0.0695 \pm 0.0021$ is the longitudinal polarization of the atomic electrons in the iron cylinder, and $A_{e^\pm}$ is the analyzing power determined by numerical simulation. The latter was performed with an enhanced version of the GEANT4 toolkit [13] that included six new routines to deal with circularly polarized photon beams and longitudinally polarized electron beams [14]: for Compton scattering, Møller or Bhabha scattering, and electron-positron annihilation the dependence of the cross section on beam

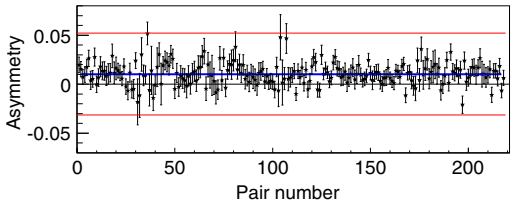

FIG. 5 (color online). Positron-induced asymmetries δ_{e^+} in the central CsI crystal of the positron polarimeter for 220 pairs of 1500 undulator-on beam pulses with opposite magnetization in the polarimeter. The central positron energy was 6.1 MeV. The average asymmetry was 0.0108, as indicated by the horizontal line.

TABLE I. The asymmetries $\delta_{e^\pm}$ (in %) observed in the transmission polarimeter TP1, and the corresponding analyzing powers $A_{e^\pm}$ and longitudinal polarizations $P_{e^\pm}$ (in %) as a function of energy $E_{e^\pm}$ in MeV.

$E_{e^\pm}$	$\delta \pm \sigma_\delta$(stat)	A	$P \pm \sigma_P$(stat) $\pm \sigma_P$(syst)
4.6 (e^+)	0.69 ± 0.17	0.150	$66 \pm 16 \pm 8$
5.4 (e^+)	0.96 ± 0.08	0.156	$89 \pm 8 \pm 9$
6.1 (e^+)	1.08 ± 0.06	0.162	$96 \pm 6 \pm 10$
6.7 (e^+)	0.92 ± 0.08	0.165	$80 \pm 7 \pm 9$
6.7 (e^-)	0.94 ± 0.05	0.153	$88 \pm 5 \pm 15$
7.4 (e^+)	0.89 ± 0.20	0.169	$76 \pm 17 \pm 12$

and target polarization was modeled; in addition, the polarization transfer from initial- to final-state particles in bremsstrahlung, electron-positron pair annihilation and creation, and the photoelectric effect was evaluated. The relative systematic uncertainty on the analyzing power is estimated to be 7%.

The asymmetries δ, the analyzing powers A, and the longitudinal polarizations $P_{e^\pm}$ of electrons and positrons deduced using Eq. (3) are listed in Table I, and the polarizations are shown together with simulations in Fig. 6 as a function of particle energy. The shift between the curves arises because for photon energies that peak near $E_\gamma = 7.9$ MeV the maximum energy of a positron from pair production is $E_{e^+} = E_\gamma - mc^2 \approx 7.4$ MeV, while electrons from Compton scattering and the photoelectric effect have maximum energies $E^{\mathrm{C}}_{e^-} \approx E_\gamma + mc^2/2 \approx 8.2$ MeV and $E^{\mathrm{PE}}_{e^-} = E_\gamma + mc^2 \approx 8.4$ MeV, respectively, where $mc^2 = 511$ keV is the rest energy of the electron.

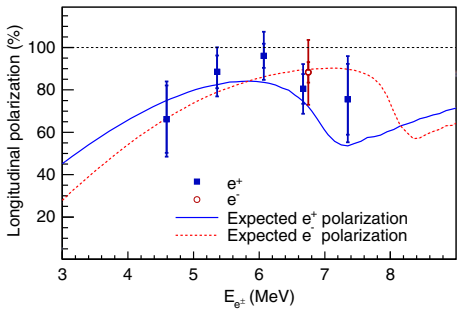

FIG. 6 (color online). Longitudinal polarization $P_{e^\pm}$ as a function of energy $E_{e^\pm}$ of positrons and electrons as determined from the asymmetries $\delta_{e^\pm}$ observed in the central CsI crystal. The smaller error bars show the statistical uncertainty, and the larger bars indicate the statistical and systematic uncertainties combined in quadrature. Also shown are predictions by a GEANT4 simulation of the experiment.

The uncertainties shown in the figure include both statistical and systematic effects where the latter were estimated from studies of the effects of non-Gaussian fluctuations and outlier rejection, from the quality cuts on the beam current, of the pairing of sets of 1500 beam pulses, of background correction, and of the stray-field-induced asymmetry at the counter P1 used for signal normalization.

The results of this experiment are in agreement with GEANT4 simulations that positron polarization of 80% is obtainable at MeV energies when GeV electrons pass through a helical undulator, producing MeV photons that are converted in a thin target. The polarization extensions to GEANT4 provide a basis for optimization of the ILC positron source, and for other applications of polarization transfer, such as polarimetry. The technique of undulator-based production of polarized positrons, demonstrated in this experiment, can be scaled up to provide polarized positron (and electron) beams for the next generation of linear colliders [7].

This work was supported in part by DOE Contract No. DE-AC03-76SF00515, DOE Grants and Nos. DE-FG05-91ER40627, DE-FG02-91ER40671, DE-FG02-03ER41283, and DE-FG02-04ER41353, by NSF Grant No. PHY-0202078 (U.S.), by European Commission Contract No. RIDS-011899 (Germany), by the STFC (U.K.), and by ISF Contract No. 342/05 (Israel).

[1] G. Moortgat-Pick *et al.*, Phys. Rep. **460**, 131 (2008).
[2] H. Olsen and L. C. Maximon, Phys. Rev. **114**, 887 (1959).
[3] V. E. Balakin and A. A. Mikhailichenko, Budker Institute of Nuclear Physics Report No. BINP 79-85, 1979.
[4] R. C. Wingerson, Phys. Rev. Lett. **6**, 446 (1961).
[5] E. G. Bessonov and A. A. Mikhailichenko, Budker Institute of Nuclear Physics BINP 92-43, 1992.
[6] T. Omori *et al.*, Phys. Rev. Lett. **96**, 114801 (2006).
[7] International Linear Collider Reference Design Report, 2007, http://www.linearcollider.org/rdr
[8] R. Erickson *et al.*, Report No. SLAC-R-714, 1984.
[9] M. Berndt *et al.*, Report No. SLAC-376, 1991.
[10] G. Alexander *et al.*, Nucl. Instrum. Methods Phys. Res., Sect. A (to be published).
[11] H. Schopper, Nucl. Instrum. **3**, 158 (1958).
[12] H. Frauenfelder and A. Rossi, in *Methods of Experimental Physics: Nuclear Physics*, edited by L. C. L. Yuan and C.-S. Wu (Academic Press, New York, 1963), Part B5, p. 214.
[13] S. Agostinelli *et al.* (GEANT4 Collaboration), Nucl. Instrum. Methods Phys. Res., Sect. A **506**, 250 (2003); J. Allison *et al.*, IEEE Trans. Nucl. Sci. **53**, 270 (2006).
[14] R. Dollan, K. Laihem, and A. Schälicke, Nucl. Instrum. Methods Phys. Res., Sect. A **559**, 185 (2006); A. Schälicke, K. Laihem, and P. Starovoitov, Report No. DESY 07-202, 2007.

Bibliography

[1] S. L. Glashow, "Partial Symmetries of Weak Interactions," *Nucl. Phys.* **22** (1961) 579–588.

[2] S. Weinberg, "A Model of Leptons," *Phys. Rev. Lett.* **19** (1967) 1264–1266.

[3] A. Salam, "Elementary Particle Theory,". p. 367.

[4] O. S. Bruning, (Ed.) *et al.*, "LHC design report. Vol. I: The LHC main ring,". CERN-2004-003-V-1, CERN-2004-003-V21, CERN-2004-003-V-3.

[5] **ALEPH, DELPHI, L3 and OPAL** Collaboration, J. Alcaraz *et al.*, "A Combination of preliminary electroweak measurements and constraints on the standard model," `arXiv:hep-ex/0612034`.

[6] **CDF** Collaboration, D. E. Acosta *et al.*, "Search for ZZ and ZW production in $p\bar{p}$ collisions at $\sqrt{s} = 1.96$ TeV," *Phys. Rev.* **D71** (2005) 091105, `arXiv:hep-ex/0501021`.

[7] **CDF** Collaboration, T. Aaltonen *et al.*, "First Measurement of ZZ Production in panti-p Collisions at $\sqrt{s} = 1.96$-TeV," *Phys. Rev. Lett.* **100** (2008) 201801, `arXiv:0801.4806 [hep-ex]`.

[8] **DØ** Collaboration, V. M. Abazov *et al.*, "Search for ZZ and $Z\gamma^*$ production in $p\bar{p}$ collisions at $\sqrt{s} = 1.96$ TeV and limits on anomalous ZZZ and $ZZ\gamma^*$ couplings," *Phys. Rev. Lett.* **100** (2008) 131801, `arXiv:0712.0599 [hep-ex]`.

[9] **DØ** Collaboration, V. M. Abazov *et al.*, "Observation of ZZ production in $p\bar{p}$ collisions at $\sqrt{s} = 1.96$-TeV," *Phys. Rev. Lett.* **101** (2008) 171803, `arXiv:0808.0703 [hep-ex]`.

[10] **ATLAS** Collaboration, G. Aad *et al.*, "The ATLAS Experiment at the CERN Large Hadron Collider," *JINST* **3** (2008) .

[11] **ATLAS** Collaboration, O. Abdinov *et al.*, "ATLAS detector and physics performance: Technical Design Report, 1,". CERN-LHCC-99-014, ATLAS-TDR-014.

[12] **ATLAS** Collaboration, O. Abdinov *et al.*, "ATLAS detector and physics performance: Technical Design Report, 2,". CERN-LHCC-99-015, ATLAS-TDR-015.

[13] **CMS** Collaboration, R. Adolphi *et al.*, "The CMS experiment at the CERN LHC," *JINST* **3** .

[14] **CMS** Collaboration, P. Anrnio *et al.*, "CMS, the Compact Muon Solenoid: Technical proposal,". CERN-LHCC-94-38.

[15] **LHCb** Collaboration, S. Amato *et al.*, "LHCb technical proposal,". CERN-LHCC-98-004.

[16] **ALICE** Collaboration, V. Abramova *et al.*, "ALICE transition-radiation detector: Technical Design Report,". CERN-LHCC-2001-021, ALICE-TDR-9, LYCEN-2001-97.

[17] "Layout of the LEP tunnel including future LHC infrastructures." AC multimeida documents, Feb, 1997.

[18] **LEP Higgs Working Group for Higgs boson searches** Collaboration, "Search for the standard model Higgs boson at LEP," `arXiv:hep-ex/0107029`.

[19] **CDF and D0** Collaboration, K. Yamamoto, "Higgs searches at the Tevatron," *Int. J. Mod. Phys.* **A25** (2010) 5097–5104.

[20] **UA1** Collaboration, G. Arnison *et al.*, "Experimental observation of isolated large transverse energy electrons with associated missing energy at s**(1/2) = 540 GeV," *Phys. Lett.* **B122** (1983) 103–116.

[21] **UA1** Collaboration, G. Arnison *et al.*, "Experimental observation of lepton pairs of invariant mass around 95 GeV/c**2 at the CERN SPS collider," *Phys. Lett.* **B126** (1983) 398–410.

[22] **UA2** Collaboration, M. Banner *et al.*, "Observation of single isolated electrons of high transverse momentum in events with missing transverse energy at the CERN anti-p p collider," *Phys. Lett.* **B122** (1983) 476–485.

[23] **UA2** Collaboration, P. Bagnaia *et al.*, "Evidence for $Z^0 \to e^+ e^-$ at the CERN anti-p p collider," *Phys. Lett.* **B129** (1983) 130–140.

[24] G. de Rijk *et al.*, "Status report on the LHC main magnet production,". CERN-LHC-PROJECT-REPORT-805.

[25] J. C. Brunet *et al.*, "Design of the second series of LHC prototype dipole magnet cryostats," *Adv. Cryog. Eng.* **43A** (1998) 435–441.

[26] J. C. Brunet *et al.*, "Design of LHC prototype dipole cryostats," *Cryogenics* **32** (1992) 191–194.

[27] "LHC magnets: first steps in the tunnel." BUL-NA-2004-020, Jul, 2007.

[28] S. de Capua, F. Ferro, M. De Gruttola, and M. Villa, "Luminosity measurements at LHC," *Nuovo Cim.* **123B** (2008) 423–434.

[29] M. Barone, E. Borchi, A. Gaddi, C. Leroy, and L. Price, eds., *Plans for the very forward region of atlas - the LUCID luminosity monitor*, World Scientific. World Scientific, Singapore, 2006. 9th ICATPP Conference on Astroparticle, Particle, Space Physics, Detectors and Medical Physics Applications, ICATTP-9, 17 - 21 Oct 2005, Como, Italy.

[30] *ATLAS inner detector: Technical Design Report, 1.* Technical Design Report ATLAS. CERN, Geneva, 1997.

[31] S. Haywood, L. Rossi, R. Nickerson, and A. Romaniouk, *ATLAS inner detector: Technical Design Report, 2.* Technical Design Report ATLAS. CERN, Geneva, 1997.

[32] **ATLAS** Collaboration, G. Aad *et al.*, "The ATLAS Experiment at the CERN Large Hadron Collider," *JINST* **3** (2008) S08003.

[33] A. Abdesselam *et al.*, "The barrel modules of the ATLAS semiconductor tracker," *Nucl. Instrum. Meth.* **A568** (2006) 642–671.

[34] **ATLAS** Collaboration, A. Abdesselam *et al.*, "The ATLAS semiconductor tracker end-cap module," *Nucl. Instrum. Meth.* **A575** (2007) 353–389.

[35] **ATLAS** Collaboration, R. Mashinistov, "Performance of the ATLAS Transition Radiation Tracker with Cosmic Rays and First High Energy Collisions at LHC,". ATL-INDET-SLIDE-2010-430, ATL-COM-INDET-2010-133.

[36] J. D. Jackson, *Classical electrodynamics; 3rd ed.* Wiley, New York, NY, 1999. p. 646-654.

[37] **ATLAS** Collaboration, V. Rossetti, "Commissioning of the ATLAS Tile Hadronic Calorimeter with cosmic muons, single beams and first collisions,". ATL-TILECAL-PROC-2010-009.

[38] **ATLAS Electromagnetic Barrel Calorimeter** Collaboration, M. Aharrouche *et al.*, "Energy linearity and resolution of the ATLAS electromagnetic barrel calorimeter in an electron test- beam," *Nucl. Instrum. Meth.* **A568** (2006) 601–623, `arXiv:physics/0608012`.

[39] **ATLAS Electromagnetic Barrel Calorimeter** Collaboration, Z. Meng *et al.*, "Performance of the ATLAS Liquid Argon Calorimeter,". ATL-LARG-PROC-2010-017.

[40] **ATLAS Liquid Argon** Collaboration, P.-S. Mangeard, "Performance of the ATLAS liquid argon calorimeter with cosmic muons and single LHC beam data," *Nucl. Instrum. Meth.* **A623** (2010) 216–218.

[41] **TileCal** Collaboration, E. Mazzoni, "Study of the TileCal hadron calorimeter of ATLAS experiment at LHC," *Nucl. Instrum. Meth.* **A409** (1998) 601–603.

[42] **ATLAS** Collaboration, M. Abolins *et al.*, "ATLAS muon spectrometer: Technical Design Report,". CERN-LHCC-97-22, ATLAS-TDR-10.

[43] M. Deile *et al.*, "Resolution and efficiency of the ATLAS muon drift-tube chambers at high background rates," *Nucl. Instrum. Meth.* **A535** (2004) 212–215.

[44] **ATLAS** Collaboration, I. Gough Eschrich, "Readout Electronics of the ATLAS Muon Cathode Strip Chambers,". ATL-MUON-PROC-2009-003. ATL-COM-MUON-2008-018.

[45] **ATLAS** Collaboration, "Commissioning of the ATLAS Muon Spectrometer with Cosmic Rays," `arXiv:1006.4384 [physics.ins-det]`.

[46] Y. Arai *et al.*, "Timing optimization of thin gap chambers for the use in the ATLAS muon endcap trigger," *Nucl. Instrum. Meth.* **A367** (1995) 398–401.

[47] R. Cardarelli *et al.*, "The implementation of the ATLAS level-1 muon trigger in the barrel region,". Prepared for International Conference on Computing in High- energy Physics (CHEP 95), Rio de Janeiro, Brazil, 18-22 Sep 1995.

[48] **ATLAS Muon** Collaboration, E. Etzion, "System Test of the ATLAS Muon Spectrometer in the H8 Beam at the CERN SPS," `arXiv:physics/0509222`.

[49] **Particle Data Group** Collaboration, C. Amsler *et al.*, "Review of particle physics," *Phys. Lett.* **B667** (2008) 1.

[50] S. D. Drell and T.-M. Yan, "Connection of Elastic Electromagnetic Nucleon Form-Factors at Large Q**2 and Deep Inelastic Structure Functions Near Threshold," *Phys. Rev. Lett.* **24** (1970) 181–185.

[51] S. D. Drell and T.-M. Yan, "Massive Lepton Pair Production in Hadron-Hadron Collisions at High-Energies," *Phys. Rev. Lett.* **25** (1970) 316–320.

[52] e.g. V.D. Barger, R. Phillips, *Collider Physics*. Addison-Wesley publishing company, 1987.

[53] A. D. Martin, R. G. Roberts, W. J. Stirling, and R. S. Thorne, "Parton distributions and the LHC: W and Z production," *Eur. Phys. J.* **C14** (2000) 133–145, `arXiv:hep-ph/9907231`.

[54] **ATLAS** Collaboration, "Measurement of the W*rightarrow*lnu and Z/gamma**rightarrow*ll production cross sections in proton-proton collisions at sqrt(s) = 7 TeV with the ATLAS detector," `arXiv:1010.2130 [hep-ex]`.

[55] **ATLAS** Collaboration, P. Jenni, M. Nessi, M. Nordberg, and K. Smith, "ATLAS high-level trigger, data-acquisition and controls: Technical Design Report,". CERN-LHCC-2003-022, ATLAS-TDR-016.

[56] J. M. Campbell and R. K. Ellis, "An update on vector boson pair production at hadron colliders," *Phys. Rev.* **D60** (1999) 113006, `arXiv:hep-ph/9905386`.

[57] E. G. Altarelli and M. Mangano, "*Proc. CERN Workshop "Standard Model Physics (and More) at the LHC*," *CERN Yellow Report* **2000/001** (Geneva, October 1999) 117–230, `arXiv:hep-ph/0003275`.

[58] J.M. Campbell, R.K. Ellis, "*MCFM: User Guide*,". http://mcfm.fnal.gov.

[59] R. Asfandiyarov, K. A. Assamagan1, G. Carrillo Montoya, Y. Fang, H. Liu, B. Mansoulie, B. Mellado Garcia, A. Nisati, J. Purdham, J. Qian, W. Quayle, J. Strandberg, R. Thun, Sau Lan Wu, "*Production Cross Section of the Higgs Boson and Other Standard Model Processes in pp Collisions at Different Center-of-Mass Energies*," *ATL-COM-PHYS-2009-051* (2009) .

[60] L. Collaboration, "e^+e^- cross sections,". http://cern.ch/l3/gif/l3_xsbig.gif.

[61] **L3** Collaboration, P. Achard *et al.*, "Measurement of hadron and lepton-pair production in e+ e- collisions at s**(1/2) = 192-GeV - 208-GeV at LEP," *Eur. Phys. J.* **C47** (2006) 1–19, arXiv:hep-ex/0603022.

[62] J. Pumplin *et al.*, "New generation of parton distributions with uncertainties from global QCD analysis," *JHEP* **07** (2002) 012, arXiv:hep-ph/0201195.

[63] S. Mandelstam, "Determination of the Pion-Nucleon Scattering Amplitude from Dispersion Relations and Unitarity. General Theory," *Phys. Rev.* **112** no. 4, (Nov, 1958) 1344–1360.

[64] E. Nuss, "Diboson production at hadron colliders with general three gauge boson couplings. Analytic expressions of helicity amplitudes and cross-section," *Z. Phys.* **C76** (1997) 701–719, arXiv:hep-ph/9610309.

[65] T. Sjostrand, S. Mrenna, and P. Z. Skands, "PYTHIA 6.4 Physics and Manual," *JHEP* **05** (2006) 026, arXiv:hep-ph/0603175.

[66] B. Andersson, G. Gustafson, G. Ingelman, and T. Sjostrand, "Parton Fragmentation and String Dynamics," *Phys. Rept.* **97** (1983) 31–145.

[67] **ATLAS** Collaboration, A. Airapetian *et al.*, "ATLAS computing technical proposal,". CERN-LHCC-96-043.

[68] **ATLAS** Collaboration, G. Aad *et al.*, "Expected Performance of the ATLAS Experiment - Detector, Trigger and Physics," arXiv:0901.0512 [hep-ex]. CERN-OPEN-2008-020.

[69] **ATLAS** Collaboration, G. Aad *et al.*, "Measurement of the W → lnu and Z/gamma* → ll production cross sections in proton-proton collisions at sqrt(s) = 7 TeV with the ATLAS detector," arXiv:1010.2130 [hep-ex].

[70] E. W. N. Glover and J. J. van der Bij, "Z Boson Pair Production via Gluon Fusion," *Nucl. Phys.* **B321** (1989) 561.

[71] D. A. Dicus, C. Kao, and W. W. Repko, "Gluon Production of Gauge Bosons," *Phys. Rev.* **D36** (1987) 1570.

[72] L. J. Dixon, Z. Kunszt, and A. Signer, "Vector boson pair production in hadronic collisions at order α_s : Lepton correlations and anomalous couplings," *Phys. Rev.* **D60** (1999) 114037, arXiv:hep-ph/9907305.

[73] E. Brodet, "Prospects of measuring Nutral Gauge Boson Coupling with the ATLAS detector," *ATL-PHYS-PUB-2007-015, ATL-COM-PHYS-2006-096* (2006) .

[74] G. Alexander and E. Reinherz-Aronis, "Quark-Antiquark Energy Density Function applied to Di- Gauge Boson Production at the LHC," *JHEP* **09** (2008) 132, arXiv:0805.4066 [hep-ex].

[75] W. K. Tung *et al.*, "Heavy quark mass effects in deep inelastic scattering and global QCD analysis," *JHEP* **02** (2007) 053, arXiv:hep-ph/0611254.

[76] M. J. Duncan, G. L. Kane, and W. W. Repko, "W W Physics at Future Colliders," *Nucl. Phys.* **B272** (1986) 517.

[77] **L3** Collaboration, P. Achard *et al.*, "Study of spin and decay-plane correlations of W bosons in the $e^+e^- \to W^+W^-$ process at LEP," *Eur. Phys. J.* **C40** (2005) 333–341, arXiv:hep-ex/0501036.

[78] C. P. Buszello, I. Fleck, P. Marquard, and J. J. van der Bij, "Prospective analysis of spin- and CP-sensitive variables in H → Z Z → l(1)+ l(1)- l(2)+ l(2)- at the LHC," *Eur. Phys. J.* **C32** (2004) 209–219, arXiv:hep-ph/0212396.

[79] **ATLAS** Collaboration, A. collaboration, "Luminosity Determination Using the ATLAS Detector," Tech. Rep. ATLAS-CONF-2010-060, CERN, Geneva, Jul, 2010.

[80] **ATLAS** Collaboration, G. Aad *et al.*, "Luminosity Determination in pp Collisions at sqrt(s)=7 TeV Using the ATLAS Detector at the LHC," *Eur. Phys. J.* **C71** (2011) 1630, arXiv:1101.2185 [hep-ex].

[81] **OPAL** Collaboration, G. Abbiendi *et al.*, "Measurement of W boson polarizations and CP violating triple gauge couplings from W^+W^- production at LEP," *Eur. Phys. J.* **C19** (2001) 229–240, arXiv:hep-ex/0009021.

[82] P. Renton, *Electroweak Interactions: an Introduction to the Physics of Quarks and Leptons*. Cambridge University Press, 1990.

[83] K. Hagiwara, R. D. Peccei, D. Zeppenfeld, and K. Hikasa, "Probing the Weak Boson Sector in $e^+ e^- \to 4W^+ W^-$," *Nucl. Phys.* **B282** (1987) 253.

[84] G. Gounaris, J. Layssac, G. Moultaka, and F. M. Renard, "Analytic expressions of cross-sections, asymmetries and W density matrices for $e^+ e^- \to W^+ W^-$ with general three on couplings," *Int. J. Mod. Phys.* **A8** (1993) 3285–3320.

[85] **OPAL** Collaboration, G. Abbiendi *et al.*, "W boson polarisation at LEP2," *Phys. Lett.* **B585** (2004) 223–236, `arXiv:hep-ex/0312047`.

[86] **OPAL** Collaboration, G. Abbiendi *et al.*, "W^+W^- production and triple gauge boson couplings at LEP energies up to 183-GeV," *Eur. Phys. J.* **C8** (1999) 191–215, `arXiv:hep-ex/9811028`.

[87] R. Hanbury Brown and R. Q. Twiss, "A New type of interferometer for use in radio astronomy," *Phil. Mag.* **45** (1954) 663–682.

[88] R. Hanbury Brown and R. Q. Twiss, "A Test of a new type of stellar interferometer on Sirius," *Nature* **178** (1956) 1046–1048.

[89] G. Goldhaber, S. Goldhaber, W.-Y. Lee, and A. Pais, "Influence of Bose-Einstein statistics on the antiproton proton annihilation process," *Phys. Rev.* **120** (1960) 300–312.

[90] G. Alexander, "Bose-Einstein and Fermi-Dirac interferometry in particle physics," *Rept. Prog. Phys.* **66** (2003) 481–522, `arXiv:hep-ph/0302130`.

[91] **OPAL** Collaboration, P. D. Acton *et al.*, "A Study of Bose-Einstein correlations in e+ e- annihilations at LEP," *Phys. Lett.* **B267** (1991) 143–153.

[92] **ZEUS** Collaboration, M. Derrick, "Bose-Einstein correlations in DIS," *Acta Phys. Polon.* **B33** (2002) 3281–3286.

[93] T. Osada, S. Sano, and M. Biyajima, "Coulomb and strong interactions for Bose-Einstein correlations," *Z. Phys.* **72** (1996) 285, `hep-ph/9606365`.

[94] U. A. Wiedemann and U. W. Heinz, "Particle interferometry for relativistic heavy-ion collisions," *Phys. Rept.* **319** (1999) 145–230, arXiv:nucl-th/9901094.

[95] A. D. Chacon *et al.*, "Pion correlations in relativistic heavy ion collisions for three symmetric systems," *Phys. Rev.* **C43** (1991) 2670–2688.

[96] G. Alexander and H. J. Lipkin, "Use of spin correlations to study low-energy Lambda Lambda and Lambda anti-Lambda space symmetries and resonances," *Phys. Lett.* **B352** (1995) 162–168.

[97] **WA98** Collaboration, M. M. Aggarwal *et al.*, "Source radii at target rapidity from two-proton and two- deuteron correlations in central Pb+Pb collisions at 158 A GeV," arXiv:0709.2477 [nucl-ex].

[98] **OPAL** Collaboration, G. Abbiendi *et al.*, "Bose-Einstein correlations of π^0 pairs from hadronic Z^0 decays," *Phys. Lett.* **B559** (2003) 131–143, arXiv:hep-ex/0302027.

[99] **L3** Collaboration, P. Achard *et al.*, "Bose-Einstein correlations of neutral and charged pions in hadronic Z decays," *Phys. Lett.* **B524** (2002) 55–64, arXiv:hep-ex/0109036.

[100] M. Kucharczyk, "Fermi-Dirac correlations in $Z^0 \to p\ p\ X$ at LEP," arXiv:hep-ex/0405057.

[101] **ALEPH** Collaboration, S. Schael *et al.*, "Two-particle correlations in p p, anti-p anti-p and K0(S) K0(S) pairs from hadronic Z decays," *Phys. Lett.* **B611** (2005) 66–80.

[102] **ALEPH** Collaboration, A. Heister *et al.*, "Two-dimensional analysis of Bose-Einstein correlations in hadronic Z decays at LEP," *Eur. Phys. J.* **C36** (2004) 147–159.

[103] G. Alexander, I. Cohen, and E. Levin, "The dependence of the emission size on the hadron mass," *Phys. Lett.* **B452** (1999) 159–166, arXiv:hep-ph/9901341.

[104] G. Alexander and E. Reinherz-Aronis, "On the role of the time scale Delta t in Bose-Einstein correlations," *Phys. Lett.* **B687** (2010) 310–313, arXiv:0910.0138 [hep-ph].

[105] **ZEUS** Collaboration, S. Chekanov *et al.*, "Bose-Einstein correlations in one and two dimensions in deep inelastic scattering," *Phys. Lett.* **B583** (2004) 231–246, arXiv:hep-ex/0311030.

[106] **NOMAD** Collaboration, P. Astier *et al.*, "Bose-Einstein correlations in charged current muon- neutrino interactions in the NOMAD experiment at CERN," *Nucl. Phys.* **B686** (2004) 3–28, arXiv:hep-ex/0404011.

[107] **WA98** Collaboration, M. M. Aggarwal *et al.*, "Interferometry of direct photons in central Pb-208 + Pb- 208 collisions at 158-A-GeV," *Phys. Rev. Lett.* **93** (2004) 022301, arXiv:nucl-ex/0310022.

[108] G. Alexander, "Mass and transverse mass effects on the hadron emitter size," *Phys. Lett.* **B506** (2001) 45–51, arXiv:hep-ph/0101319.

[109] T. Csorgo and S. Pratt, "Structure of the peak in Bose-Einstein correlations,". Prepared for International Workshop on Relativistic Heavy Ion Collisions at Present and Future Accelerators, Budapest, Hungary, 17-21 Jun 1991.

[110] **ECFA/DESY LC Physics Working Group** Collaboration, J. A. Aguilar-Saavedra *et al.*, "TESLA Technical Design Report Part III: Physics at an e^+e^- Linear Collider," arXiv:hep-ph/0106315.

[111] J. E. Augustin *et al.*, "Linear Collider, Final International Technology Recommendation Panel report,".

[112] I. Wilson, "The compact linear collider CLIC," *Phys. Rept.* **403-404** (2004) 365–378.

[113] R. Prepost, "*Proceeding of the 21st SLAC Summer Institute on Particle Physics: Spin Structure in High Energy Processes*," *SLAC-Report* **444** (1994) p.57. SLAC-R-444.

[114] G. Moortgat-Pick *et al.*, "The role of polarized positrons and electrons in revealing fundamental interactions at the linear collider," *Phys. Rept.* **460** (2008) 131–243, arXiv:hep-ph/0507011.

[115] V. E. Balakin and A. A. Mikhailichenko, "Conversion system for obtaining highly polarized electrons and positrons,". INP-79-85.

[116] **E166** Collaboration, G. Alexander *et al.*, "Undulator-based production of polarized positrons: A proposal for the 50-GeV beam in the FFTB,". SLAC-TN-04-018, SLAC-PROPOSAL-E-166, LC-DET-2003-044.

[117] **E166** Collaboration, G. Alexander *et al.*, "Observation of Polarized Positrons from an Undulator-Based Source," *Phys. Rev. Lett.* **100** (2008) 210801.

[118] **E166** Collaboration, G. Alexander *et al.*, "Undulator-Based Production of Polarized Positrons," *Nucl. Instrum. Meth.* **A610** (2009) 451–487, `arXiv:0905.3066 [physics.ins-det]`.